TKK Dissertations 71
Espoo 2007

EFFECT OF STRAIN-INDUCED α'-MARTENSITE TRANSFORMATION ON MECHANICAL PROPERTIES OF METASTABLE AUSTENITIC STAINLESS STEELS

Doctoral Dissertation

Juho Talonen

Helsinki University of Technology
Department of Mechanical Engineering
Laboratory of Engineering Materials

TKK Dissertations 71
Espoo 2007

EFFECT OF STRAIN-INDUCED α'-MARTENSITE TRANSFORMATION ON MECHANICAL PROPERTIES OF METASTABLE AUSTENITIC STAINLESS STEELS

Doctoral Dissertation

Juho Talonen

Dissertation for the degree of Doctor of Science in Technology to be presented with due permission of the Department of Mechanical Engineering for public examination and debate in Auditorium K216 at Helsinki University of Technology (Espoo, Finland) on the 1st of June, 2007, at 12 noon.

Helsinki University of Technology
Department of Mechanical Engineering
Laboratory of Engineering Materials

Teknillinen korkeakoulu
Konetekniikan osasto
Koneenrakennuksen materiaalitekniikan laboratorio

Distribution:
Helsinki University of Technology
Department of Mechanical Engineering
Laboratory of Engineering Materials
P.O. Box 4200
FI - 02015 TKK
FINLAND
URL: http://dislokaatio.hut.fi/
Tel. +358-9-451 3538
Fax +358-9-451 3537
E-mail: juho.talonen@tkk.fi

ISBN 978-951-22-8779-6
ISBN 978-951-22-8780-2 (PDF)
ISSN 1795-2239
ISSN 1795-4584 (PDF)
URL: http://lib.tkk.fi/Diss/2007/isbn9789512287802/

TKK-DISS-2300

Yliopistopaino
Helsinki 2007

ABSTRACT OF DOCTORAL DISSERTATION	HELSINKI UNIVERSITY OF TECHNOLOGY P.O. BOX 1000, FI-02015 TKK http://www.tkk.fi

Author Juho Talonen

Name of the dissertation

Effect of strain-induced α'-martensite transformation on mechanical properties of metastable austenitic stainless steels

Manuscript submitted 04.01.2007	Manuscript revised 11.04.2007
Date of the defence 01.06.2007	
☒ Monograph	☐ Article dissertation (summary + original articles)

Department	Department of Mechanical Engineering
Laboratory	Laboratory of Engineering Materials
Field of research	Material Science
Opponents	Prof. Paulo Ferreira and PhD Wade Karlsen
Supervisor	Prof. Hannu Hänninen

Abstract

Metastable austenitic stainless steels undergo a strain-induced martensitic transformation, where the metastable austenite phase is transformed to the thermodynamically more stable α'-martensite phase due to the plastic deformation. The strain-induced martensitic transformation enhances the work hardening of metastable austenitic stainless steels. This thesis concentrated on the effects of the strain-induced martensitic transformation on the mechanical properties of metastable austenitic stainless steels, focussing on the interaction between the strain-induced martensitic transformation and the work hardening. The effects of chemical composition, temperature and strain rate on the strain-induced martensitic transformation were also studied.

The experiments were carried out on steel grades EN 1.4318 (AISI 301LN) and EN 1.4301 (AISI 304). Mechanical testing was performed by means of uniaxial tensile tests. The α'-martensite volume fractions were measured with a Ferritescope. X-ray diffraction was used for the phase identification, dislocation density measurements and to measure the stacking fault energies of the test materials. Microstructure investigations were carried out by means of the scanning electron microscopy, transmission electron microscopy and optical metallography. Load distribution between the austenite and α'-martensite phases was studied by *in-situ* X-ray diffraction stress measurements.

Increasing strain rate and temperature were found to suppress the formation of strain-induced α'-martensite. This was attributed to the temperature-dependence of the stacking fault energy. A direct relationship between the work-hardening rate and the rate of the strain-induced α'-martensite transformation was found. The higher was the transformation rate, the higher was the work-hardening rate. The α'-martensite transformation was concluded to affect the uniform elongation through its influence on the work-hardening rate. The dislocation density of the austenite phase was found to increase with increasing plastic strain and stress. Instead, the dislocation density of the α'-martensite was substantially higher and remained relatively constant. Two alternative strengthening mechanisms of the α'-martensite were proposed. When the α'-martensite content is below 30%, the hard α'-martensite particles dispersion harden the softer austenite phase, and the plastic deformation of the aggregate is accommodated mainly by the deformation of the austenite phase. When the α'-martensite content exceeds 30%, the α'-martensite was concluded to form a percolating cluster extending through the body. Thereafter, the aggregate can deform only if also the α'-martensite phase is deformed. This further increases the work-hardening rate.

Keywords	austenitic stainless steel, work hardening, strain-induced martensite, stacking fault energy		
ISBN (printed)	978-951-22-8779-6	ISSN (printed)	1795-2239
ISBN (pdf)	978-951-22-8780-2	ISSN (pdf)	1795-4584
Language	English	Number of pages	125 p.
Publisher	Helsinki University of Technology, Laboratory of Engineering Materials		
Print distribution	Helsinki University of Technology, Laboratory of Engineering Materials		

☒ The dissertation can be read at http://lib.tkk.fi/Diss/2007/isbn9789512287802/

VÄITÖSKIRJAN TIIVISTELMÄ	TEKNILLINEN KORKEAKOULU PL 1000, 02015 TKK http://www.tkk.fi

Tekijä Juho Talonen

Väitöskirjan nimi

Venymän aiheuttaman martensiittitransformaation vaikutus metastabiilien austeniittisten ruostumattomien terästen mekaanisiin ominaisuuksiin

Käsikirjoituksen päivämäärä 04.01.2007	Korjatun käsikirjoituksen päivämäärä 11.04.2007
Väitöstilaisuuden ajankohta 01.06.2007	
☒ Monografia	☐ Yhdistelmäväitöskirja (yhteenveto + erillisartikkelit)

Osasto	Konetekniikan osasto
Laboratorio	Koneenrakennuksen materiaalitekniikan laboratorio
Tutkimusala	Materiaalitekniikka
Vastaväittäjät	Prof. Paulo Ferreira ja PhD Wade Karlsen
Työn valvoja	Prof. Hannu Hänninen

Tiivistelmä

Metastabiileissa austeniittisissa ruostumattomissa teräksissä tapahtuu plastisen venymän vaikutuksesta faasimuutos, jossa huoneenlämpötilassa pysyvä austeniittifaasi transformoituu termodynaamisesti stabiilimmaksi α'-martensiitiksi. Martensiittitransformaation takia metastabiilit austeniittiset ruostumattomat teräkset muokkauslujittuvat voimakkaasti. Väitöskirjan tavoitteena oli tarkastella venymän aiheuttaman martensiittitransformaation vaikutusta metastabiilien austeniittisten ruostumattomien terästen mekaanisiin ominaisuuksiin, keskittyen erityisesti martensiittitransformaation ja muokkauslujittumisen väliseen yhteyteen. Lisäksi tutkittiin kemiallisen koostumuksen, lämpötilan ja muodonmuutos-nopeuden vaikutusta martensiittitransformaatioon.

Koemateriaaleina käytettiin teräslaatuja EN 1.4318 (AISI 301LN) ja EN 1.4301 (AISI 304). Koemateriaalien mekaanisia ominaisuuksia tutkittiin vetokokein. α'-martensiitin faasiosuus määritettiin ferriittimittarilla. Röntgendiffraktiomittauksia käytettiin ε- ja α'-martensiittifaasien havaitsemiseen, dislokaatiotiheysmittauksiin ja terästen pinousvian pintaenergian mittaukseen. Muokkauksessa syntyneitä mikrorakenteita tutkittiin käyttäen pyyhkäisy- ja läpivalaisuelektronimikroskopiaa sekä optista metallografiaa. Jännitysten jakautumista faasien välillä vetomuodonmuutoksen aikana tarkasteltiin in situ jännitysmittauksin röntgendiffraktion avulla.

Lämpötilan ja muodonmuutosnopeuden kasvaessa α'-martensiittia havaittiin muodostuvan vähemmän. Tämä johtui pääasiassa pinousvian pintaenergian lämpötilariippuvuudesta. Muokkauslujittumisen ja α'-martensiittitransformaation välillä havaittiin suora yhteys. Mitä suurempi transformaationopeus oli, sitä nopeampaa oli muokkauslujittuminen. Martensiittitransformaatio vaikutti terästen tasavenymään muokkauslujittumisnopeuden kautta. Venymän ja jännityksen kasvaessa austeniitin dislokaatiotiheys kasvoi, mutta α'-martensiitin dislokaatiotiheys pysyi melko muuttumattomana ja oli alusta lähtien selvästi suurempi kuin austeniitin. α'-martensiitin todettiin lujittavan teräksiä kahdella eri mekanismilla: α'-martensiittipitoisuuden ollessa alle 30% luja martensiittifaasi dispersiolujittaa pehmeämpää austeniittia, ja plastinen muodonmuutos tapahtuu pääasiassa austeniitin deformaation välityksellä. α'-martensiittipitoisuuden ylittäessä 30% α'-martensiitti muodostaa perkoloivan klusterin, joka ulottuu läpi koko materiaalin. Näin ollen materiaali ei voi muokkautua ilman, että myös lujempi α'-martensiitti muokkautuu. Tämä ilmenee yhä nopeampana muokkauslujittumisena.

Asiasanat austeniittinen ruostumaton teräs, muokkauslujittuminen, pinousvian pintaenergia, venymän aiheuttama martensiittitransformaatio, työstökarkeneminen

ISBN (painettu)	978-951-22-8779-6	ISSN (painettu)	1795-2239
ISBN (pdf)	978-951-22-8780-2	ISSN (pdf)	1795-4584
Kieli	englanti	Sivumäärä	125 s.

Julkaisija Teknillinen korkeakoulu, Koneenrakennuksen materiaalitekniikan laboratorio

Painetun väitöskirjan jakelu Teknillinen korkeakoulu, Koneenrakennuksen materiaalitekniikan laboratorio

☒ Luettavissa verkossa osoitteessa http://lib.tkk.fi/Diss/2007/isbn9789512287802/

ABSTRACT

Metastable austenitic stainless steels undergo a strain-induced martensitic transformation, where the metastable austenite phase is transformed to the thermodynamically more stable α'-martensite phase due to plastic deformation. The strain-induced martensitic transformation enhances the work hardening of the metastable austenitic stainless steels, and affects their ductility. This thesis concentrated on the effects of the strain-induced martensitic transformation on the mechanical properties of the metastable austenitic stainless steels, focussing on the interaction between the strain-induced martensitic transformation and the work hardening. The effects of chemical composition, temperature and strain rate on the strain-induced martensitic transformation were studied.

The experiments were carried out on the steel grades EN 1.4318 (AISI 301LN) and EN 1.4301 (AISI 304). Mechanical testing was performed by means of uniaxial tensile tests at temperatures ranging between -40 and +80°C and at strain rates ranging between 3×10^{-4} and 200 s^{-1}. The α'-martensite volume fractions were measured with a Ferritescope. X-ray diffraction was used for phase identification, dislocation density measurements and to measure the stacking fault energies of the test materials. Microstructure investigations were carried out by means of the scanning electron microscopy, transmission electron microscopy and optical metallography. Load distribution between the phases was studied by *in-situ* X-ray diffraction stress measurements.

The effects of applied stress and the stacking fault energy on the formation of the shear bands, acting as the nucleation sites for the α'-martensite, were demonstrated by using the model developed by Byun (2003). An excellent correlation between the theoretical predictions and the scanning electron microscopy findings was found. The suppression of the strain-induced α'-martensite transformation with increasing strain rate and temperature was attributed to the temperature dependence of the stacking fault energy. A direct relationship between the work-hardening rate and the rate of the α'-martensite transformation was found. The α'-martensite transformation was concluded to govern the uniform elongation by affecting the work-hardening rate. In the optimum condition the transformation effectively shifts the intersection of the stress-strain and work-hardening curves to higher strains. The higher was the transformation rate, the higher was the work-hardening rate. The dislocation density of the austenite phase was found to increase with increasing plastic strain and stress. Instead, the dislocation density of the α'-martensite was substantially higher and remained relatively constant. The work hardening sequence of the metastable steels was divided in four stages. During the first stage, the work-hardening rate decreased rapidly due to the dynamic softening effect caused by the strain-induced α'-martensite transformation. During the stage II, the work-hardening rate started to increase due to the dispersion hardening caused by the strain-induced α'-martensite. The dispersion hardening effect was analysed by means of quantitative optical metallography and the theory developed by Ashby (1971). At the onset of the stage III, the α'-martensite forms a percolating cluster extending through the whole body. This manifested itself by an abrupt change in the relations between the flow stress, α'-martensite volume fraction and dislocation density of the austenite. During the stage III the work-hardening rate continued to increase. The stage IV was related to the high α'-martensite volume fractions, where the α'-martensite became the matrix phase, and the work-hardening rate started to decrease.

PREFACE

The research work presented in this thesis was started and mostly accomplished in the Fifth European Community Framework Programme project LIGHT&SAFE. The membership in the GSCME graduate school funded by the Ministry of Education made possible to concentrate on the post-graduate studies and writing of the thesis during and after the LIGHT&SAFE project. Significant financial support enabling the completion of the work has also been provided by Outokumpu Stainless Research Foundation, Outokumpu Foundation, Henry Ford Foundation and Walter Ahlström Foundation, which are gratefully acknowledged.

I would like to express my gratitude to my supervisor, professor Hannu Hänninen, for his support and encouragement, and for suggesting me a challenging research problem. I also wish to thank the project steering committee of the LIGHT&SAFE project, and especially the coordinator Dr. Nuri Akdut, for the fruitful project work. Tero Taulavuori and other staff of Outokumpu Stainless Oy Tornio Research Centre are acknowledged for carrying out a part of the tensile test experiments and for valuable discussions. Dr. Gersom Pape, Delft University of Technology and Delft Technology & Research Laboratories are acknowledged for performing the high speed tensile tests. I also want to thank Niko Tolvanen for helping me with the grammar of the thesis and Pertti Nenonen for carrying out the TEM experiments.

I want to thank professor Erno Keskinen, professor Michel Cotsaftis and my postgraduate student colleagues in the GSCME graduate school for the memorable postgraduate seminars and interesting scientific discussions. I am also grateful to professor Staffan Hertzman and to my postgraduate student colleagues supported by Outokumpu Stainless Research Foundation, as well as to the personnel of Avesta Research Centre, for the interesting seminars held in Avesta.

I am grateful to my colleagues in the Laboratory of Engineering Materials for creating a pleasant working environment. Special thanks are due to Dr. Yuriy Yagodzinskyy for his support and valuable comments on my thesis, and to Kim Widell, Jari Hellgren and Heikki Westman for the assistance with the experiments.

Finally, I would like to thank my family and friends for their support and Anna-Leena for her love and patience.

Otaniemi, May 2007

Juho Talonen

CONTENTS

LIST OF ABBREVIATIONS

BCC	Body-Centred Cubic
EBSD	Electron Backscatter Diffraction
ECC	Electron Channelling Contrast
ECCI	Electron Channelling Contrast Imaging
FCC	Face-Centred Cubic
FEG-SEM	Field Emission Gun Scanning Electron Microscope
FEG-STEM	Field Emission Gun Scanning Transmission Electron Microscope
FEM	Finite Element Method
FWHM	Full Width at Half Maximum
HCP	Hexagonal Close Packed
IBM	Integral Breadth Method
LEDS	Low-Energy Dislocation Structure
RMSS	Root Mean Square Microstrain
SFE	(Intrinsic) Stacking Fault Energy
SFP	Stacking Fault Probability
TEM	Transmission Electron Microscopy
TRIP	Transformation-Induced Plasticity
VM	Voigt Method
WHR	Work-Hardening Rate
XRD	X-Ray Diffraction

NOMENCLATURE

a	Lattice parameter [Å]
A	Elastic anisotropy factor (Zener anisotropy)
b	Absolute value of Burgers vector of a perfect dislocation [Å]
b_p	Absolute value of Burgers vector of a Shockley partial dislocation [Å]
b_2, b_3	Burgers vectors of Shockley partial dislocations [Å]
c	Constant
C	Specific heat [J/kgK]
d	Lattice spacing [Å]
$d_{\phi\psi}$	Lattice spacing measured at the angles of ϕ and ψ [Å]
d_0	Unstressed lattice spacing [Å]
d_{111}	Spacing between {111} planes [Å]
D	Volume [m^3]
$\langle D \rangle$	Volume-weighted coherent domain size [nm]
$\langle D \rangle_{true}$	True coherent domain size [nm]
e	Approximate upper limit of lattice distortions
E	Elastic modulus [GPa]
E_d	Energy of dislocation line per unit length [J/m]
E^{str}	Coherency strain energy related to martensitic transformation [J/mol]
E_{tot}	Total elastic strain energy stored by dislocations [J/m^3]
$f^{\alpha'}$	Volume fraction of α'-martensite phase
F	Factor describing the effect of interaction of adjacent dislocations on the self-energy of a dislocation
G	Shear modulus [GPa]
GS	ASTM grain size number
$\Delta G^{\gamma\rightarrow\alpha'}$	Chemical free-energy difference between austenite and α'-martensite phases [J/mol]
$\Delta G_{Ms}^{\gamma\rightarrow\alpha'}$	Chemical free-energy difference between austenite and α'-martensite phases at M_S temperature [J/mol]
$\Delta G_{T1}^{\gamma\rightarrow\alpha'}$	Chemical free-energy difference between austenite and α'-martensite phases at temperature T_1 [J/mol]
$\Delta G^{\gamma\rightarrow\varepsilon}$	Chemical free-energy difference between austenite and ε-martensite phases [J/mol]
K	Constant
K_{111}	Constant
L	Mean chord length of martensite particles [μm]
$\Sigma_b(\pm)L_0/h_0^2(u+b)$	Constant
m_1, m_2	Absolute values of Schmid factors of Shockley partial dislocations
M_d	Temperature above which no strain-induced martensite is formed [°C]
M_{d30}	Temperature at which 50% α'-martensite is formed at 30% true tensile strain [°C]
M_S	Martensite start temperature [°C]
M_S^{σ}	Temperature above which martensitic transformation can occur only due to plastic deformation [°C]
n	Constant
n^{CR}	Critical thickness of martensitic embryo [Å]

n^T	Number of dislocation loops per martensite particle
n*	Thickness of a stacking fault in number of atom planes
N	Number of dislocations in domain wall
N^T	Number of dislocation loops per unit volume [m^{-3}]
N_v	Number of martensite particles per unit volume [m^{-3}]
r	Radius of the strain field of a dislocation [nm]
r_0	Radius of dislocation core [nm]
s_0	Shear strain
T, T_1	Temperature [K]
ΔT	Temperature change [K]
U'	Mechanical driving force [J/mol]
w	Width of stacking fault, *i.e.*, the separation distance between two Shockley partial dislocations [Å]
wG	Gaussian component of physical line profile
wG_E	Gaussian component of experimental line profile
wG_I	Gaussian component of instrumental line profile
wL	Lorentzian component of physical line profile
wL_E	Lorentzian component of experimental line profile
wL_I	Lorentzian component of instrumental line profile
x	Factor describing the ratio of the extrinsic and intrinsic stacking fault energies
α	Stacking fault probability
α_{OC}	Constant
α_0	Constant
β	Integral breadth of physical line profile [rad]
β_D	Integral breadth due to lattice distortions, *i.e.*, strain broadening [rad]
β_E	Integral breadth of experimental line profile [rad]
β_G	Integral breadth of Gaussian function [rad]
β_I	Instrumental broadening [rad]
β_L	Integral breadth of Lorentzian function [rad]
β_{OC}	Constant
β_S	Integral breadth due to small domain size, *i.e.*, size broadening [rad]
β_T	Twin fault probability
γ	Intrinsic stacking fault energy [mJ/m^2]
γ_{eff}	Effective stacking fault energy [mJ/m^2]
γ_0	Intrinsic stacking fault energy at temperature at which $\Delta G^{\gamma\rightarrow\varepsilon}=0$ [mJ/m^2]
ε, ε_0	True strain
$\Delta\varepsilon$	Strain increment
$<\varepsilon^2>$	Mean square microstrain
$<\varepsilon_{50}^2>$	Mean square microstrain averaged over the distance of 50 Å
$<\varepsilon^2>^{1/2}$	Root mean square microstrain
$(\varepsilon'_{33})_{\phi\omega}$	Lattice strain measured with XRD
θ	Diffraction angle [rad]
θ_1, θ_2	Angles between the unit vector of perfect dislocation line and the Burgers vectors of the leading and trailing partial dislocations [rad]
$\Delta(2\theta_{200}-2\theta_{111})_{ANN}$	Distance between austenite 200 and 111 reflections in annealed sample [rad]

$\Delta(2\theta_{200}\text{-}2\theta_{111})_{CW}$	Distance between austenite 200 and 111 reflections in cold-worked sample [rad]
Θ	Angle between the stress axis and the normal of habit plane of a martensite nucleus [rad]
λ	Wavelength [Å]
λ^L	Mean matrix chord length [μm]
μ	Factor characteristic of dislocation type
ν	Poisson's ratio
ξ	Contraction normal to the basal plane due to $\gamma \rightarrow \varepsilon$ transformation
ρ	Dislocation density [m^{-2}]
ρ_A	Density of atoms in a close packed plane [mol/m^2]
ρ_{AGG}	Dislocation density of austenite per unit volume of aggregate [m^{-2}]
ρ_d	Density [kg/m^3]
ρ_D	Dislocation density calculated from domain size [m^{-2}]
ρ_G	Density of geometrically necessary dislocations [m^{-2}]
$\Delta\rho_G$	Increase in density of geometrically necessary dislocations [m^{-2}]
ρ_S	Dislocation density calculated from microstrain [m^{-2}]
ρ_0	Initial dislocation density of austenite at the onset of α'-martensite transformation [m^{-2}]
σ	True stress, flow stress [MPa]
σ_E	Athermal component of flow stress [MPa]
$\sigma(n)$	Surface energy [mJ/m^2]
σ_S	Dynamic softening contribution due to strain-induced α'-martensite transformation [MPa]
σ_T	Critical stress for twinning [MPa]
$\sigma_{\alpha'}$	Stress level in α'-martensite [MPa]
σ_γ	Stress level in austenite [MPa]
σ_0	Constant [MPa]
σ^*	Thermal component of flow stress [MPa]
τ	Shear stress [MPa]
ϕ	Angle around the sample surface normal [rad]
ψ	Angle between the X-ray beam and sample surface [rad]
Ω	Angle at which the X-ray beam enters the sample surface [rad]
ω_0	Constant

ORIGINAL FEATURES

The following features are believed to be original:

1. The electron channelling contrast imaging (ECCI) technique was utilised to visualise the shear bands formed in the austenite phase. The appearance of the shear bands was shown to be dependent on the combination of the stacking fault energy and the applied stress. An excellent correlation between the experimental findings made by ECCI and Byun's (2003) model predicting the stress-dependence of the stacking fault width was found.

2. Non-homogeneous nature of the plastic deformation of austenite-α'-martensite aggregate was demonstrated by X-ray diffraction line broadening analysis of tensile strained samples and X-ray diffraction stress measurements performed *in situ* during uniaxial tensile tests.

3. A direct relation between the work-hardening rate of metastable austenitic stainless steel and the α'-martensite transformation rate was shown. The work hardening was divided in four stages. The contribution of the α'-martensite transformation to the mechanical response during each stage was discussed.

4. Ashby's (1971) dispersion hardening theory was applied in order to explain the strengthening effect of the α'-martensite phase. An excellent correlation between the calculated density of geometrically necessary dislocations and the dislocation density measured by means of X-ray diffraction line broadening analysis was found.

5. α'-martensite volume fraction of 0.3 was found to be a critical fraction above which the harder α'-martensite phase starts to directly contribute to the work-hardening rate and strength of the austenite-α'-martensite aggregate. This was attributed to the percolation threshold of the α'-martensite phase, *i.e.*, to the formation of an infinite cluster of α'-martensite phase extending through the whole body. The α'-martensite clusters were analysed by optical metallography and coupled image analysis, and the percolation threshold was found to be about 0.3.

1 INTRODUCTION

Austenitic stainless steels are widely used in engineering applications due to their good corrosion resistance, weldability and mechanical properties. Until now, corrosion resistance has in most of the cases been the main motivation for their use.

Due to increasingly strict safety regulations and the need to reduce the fuel consumption, the car industry has become increasingly aware of the structural materials of better performance. As the austenitic stainless steels show a better strength/elongation ratio compared to almost any other metallic structural materials used in car body structures (Figure 1), they have become an attractive group of materials to be used in crash relevant structures. Figure 1 demonstrates how the strength-elongation ratio of the austenitic stainless steels can be adjusted within a wide range by work hardening. Although austenitic stainless steels have a higher material cost than the plain carbon steel grades, their use can be cost effective if their good formability and high strength are reasonably well exploited in the part design and manufacturing process. Furthermore, the lower weight of the stainless steel part reduces the costs and the environmental impact during the use phase of the part (Säynevirta, 2005).

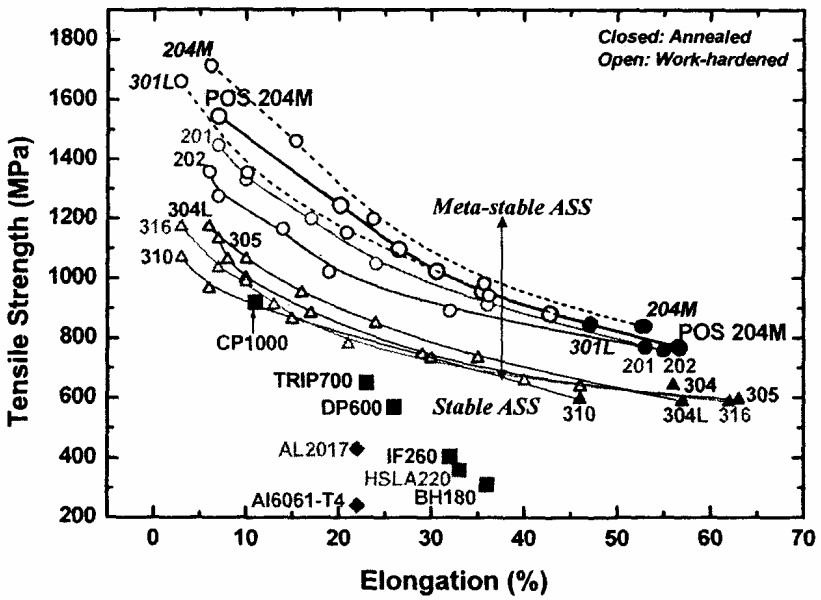

Figure 1 Elongation vs. tensile strength of various austenitic stainless steel grades in annealed and work-hardened condition (circles and triangles) compared to carbon steels and aluminium alloys (Kim *et al.*, 2003)

The strain rate is a key parameter when assessing material performance in the automotive applications, since both during the manufacturing process and a car crash high strain rates occur. With conventional structural materials, the major influence of the high strain rate is the increased flow stress. In contrast, austenitic stainless steels show complex changes in the microstructural evolution and mechanical behaviour with varying strain rate, which is related to the low stacking fault energy of the steels and the strain-induced martensitic transformations. Furthermore, the microstructural evolution and the mechanical behaviour are sensitive to chemical composition, temperature, stress state and grain size. Understanding of the interplay between these factors, resulting microstructures and the consequent mechanical response is crucial not only in terms of

the selection of an optimal material, but also in the development of the material models for finite element method (FEM) simulations, which are nowadays extensively utilised in the car industry to study forming and crash performance.

1.1 Effects of temperature and strain rate on plastic deformation of single-phase face-centred cubic metals

1.1.1 Effect of temperature and strain rate on flow stress

The flow stress of a crystalline material is dependent on the temperature and strain rate due to the thermal activation of dislocation motion. The flow stress σ consists of the thermal and athermal components σ^* and σ_E (Reed-Hill and Abbaschian, 1992):

$$\sigma = \sigma^* + \sigma_E . \tag{1}$$

The athermal component originates from long-range forces caused by, *e.g.*, other dislocations. The long-range forces cause barriers too high to be overcome by thermal activation. Thus, the athermal component is temperature dependent only through the temperature dependence of the elastic modulus, as indicated by the subscript E. The thermal component is significant when the dislocations are overcoming short-range obstacles. With increasing temperature, the thermal activation increases. Consequently, the thermal component of the flow stress decreases. The strain rate affects the thermal component of the flow stress, because the probability of the thermal activation decreases with increasing strain rate. Accordingly, the thermal component of the flow stress increases with increasing strain rate. This behaviour is often referred to as the positive strain rate sensitivity. On the other hand, the adiabatic heating during high speed deformation increases the thermal activation and may decrease the thermal component of the flow stress.

In general, in face-centred cubic (FCC) metals the thermal component of the flow stress is small. Consequently, FCC metals exhibit a rather small temperature dependence of the yield strength. However, the work-hardening rate of the FCC metals is largely affected by the stacking fault energy (SFE), which decreases with decreasing temperature. Therefore, the work-hardening rate of FCC metals may increase with decreasing temperature. (Reed-Hill and Abbaschian, 1992)

1.1.2 Effect of temperature and strain rate on ductility

The onset of the plastic instability, corresponding to the uniform elongation, is determined according to Considére's criterion as:

$$\sigma = \frac{d\sigma}{d\varepsilon}, \tag{2}$$

where σ is the flow stress and $d\sigma/d\varepsilon$ is the work-hardening rate. Considére's criterion corresponds to the condition, where the reduction in the load bearing capacity due to the decreasing cross-sectional area of the sample can no longer be compensated by the work hardening. As the work-hardening rate of FCC metals increases with decreasing temperature, but the yield strength is relatively unaffected by the temperature, the

intersection of the work-hardening rate and stress-strain curves is shifted to higher strains with decreasing temperature. Consequently, the uniform elongation of FCC metals increases with decreasing temperature (Reed-Hill and Abbaschian, 1992). Strain rate affects both the yield strength and the temperature due to adiabatic heating. Thus, the influence of the strain rate on the uniform elongation is determined by the combination of the both effects.

Besides the uniform elongation, also the post-uniform elongation is affected by the temperature and strain rate. El-Magd *et al.* (1997) suggested that the total elongation, comprising the uniform and post-uniform elongations, is affected by the strain rate due to: 1) adiabatic heating, 2) strain rate sensitivity, 3) inertia effects and 4) decrease in the local failure strain. In general, adiabatic heating softens the material, the effect being stronger in the neck area where the local strain rate is higher. However, in the neck zone high local strain rates lead to higher flow stresses due to the strain rate sensitivity. This effect has been shown to be dominant compared to the softening due to adiabatic heating (El-Magd *et al.*, 1997). Hu *et al.* (1994) showed that inertia can improve the post-uniform elongation above a certain critical strain rate that is dependent on the material. The improvement in elongation was the highest with the materials having the lowest ductility.

1.2 Plastic deformation of metastable austenitic stainless steels

1.2.1 Crystal structure of austenitic stainless steels

Austenitic stainless steels have FCC microstructure. This is achieved by the combination of chromium and nickel alloying. The most common alloy content is 18% Cr and 8% Ni. With 200-series alloys the nickel alloying is partially replaced by manganese. The interstitial atoms, namely carbon and nitrogen, also promote the FCC crystal structure and cause significant solid solution strengthening. The use of carbon for solid solution strengthening is, however, hindered by its tendency to form carbides at high temperatures. This may result in the depletion of chromium in the grain boundaries, and therefore, cause a risk of intergranular corrosion. Instead, such a risk is smaller in the case of nitrogen. Hence, nitrogen has been used as an alloying element providing austenite stabilisation, solid solution strengthening and increased corrosion resistance in various austenitic stainless steel grades. An example of the nitrogen alloyed grades is the steel EN 1.4318 (AISI 301LN), which has the nitrogen content of 0.1-0.2 %.

The stacking fault energy of austenitic stainless steels is low, typically about 20 mJ/m^2. Numerous investigations (*e.g.*, Schramm and Reed, 1974; Rhodes and Thompson, 1977; Brofman and Ansell, 1978; Ferreira and Müllner, 1998) have been carried out in order to clarify the compositional dependence of the SFE. In general, the SFE of austenitic stainless steels tends to increase with increasing alloying. However, significant uncertainty of the influence of individual elements, especially about the influence of nitrogen (Gavriljuk and Berns, 1999), still exists.

The FCC microstructure of most austenitic stainless steels is not thermodynamically stable around the room temperature. Therefore, applied stress or plastic deformation may induce a diffusionless martensitic phase transformation, by which the metastable

austenite phase is transformed to the thermodynamically more stable martensite phase. Two different martensite phases exist in austenitic stainless steels: hexagonal close-packed (HCP) ε-martensite and body-centred cubic (BCC) α'-martensite. Due to the relatively low interstitial content, the crystal structure is normally referred to as BCC and not as body-centred tetragonal. As it will be discussed below, the strain-induced martensitic transformations have a pronounced influence on the mechanical properties of metastable austenitic stainless steels.

1.2.2 Thermodynamics of strain-induced martensite transformations

The thermodynamics of strain-induced martensitic transformation are illustrated schematically in Figure 2, which shows the chemical free energies of the austenite and martensite phases as a function of temperature. Spontaneous martensitic transformation can take place only if the difference between the chemical free energies of the austenite and martensite phases, *i.e.,* the chemical driving force, reaches the critical value $\Delta G_{Ms}^{\gamma\rightarrow\alpha'}$, which occurs at the M_S temperature.

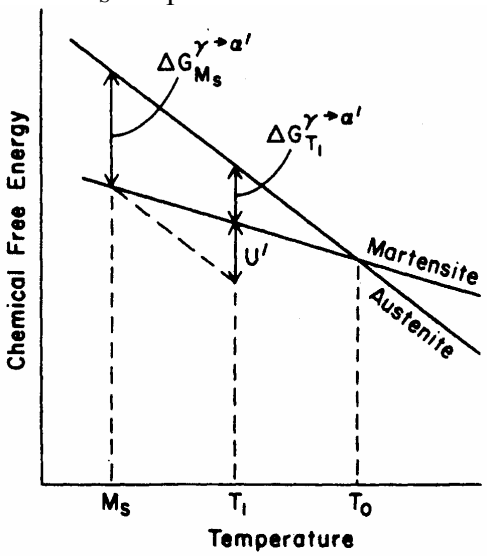

Figure 2 Schematic illustration of chemical free energies of austenite and martensite phases as a function of temperature (Wayman and Bhadeshia, 1996)

However, the transformation can occur also at the temperature T_1 (>M_S), if a sufficient mechanical driving force U' is available, so that:

$$\Delta G_{T_1}^{\gamma\rightarrow\alpha'} + U' = \Delta G_{M_s}^{\gamma\rightarrow\alpha'}. \qquad (3)$$

The mechanical driving force is believed to originate from the applied stress, which aids the chemical driving force. Patel and Cohen (1953) suggested the following expression for the mechanical driving force as a function of stress and orientation:

$$U' = \tau s_0 + \sigma\varepsilon_0 = \frac{1}{2} s_0 \sigma \sin 2\Theta \pm \frac{1}{2}\varepsilon_0\sigma(1+\cos 2\Theta), \qquad (4)$$

where the terms τs_0 and $\sigma\varepsilon_0$ represent the work done by the shear and normal stresses, respectively, σ is the absolute value of the applied stress and Θ the angle between the stress axis and the normal of the habit plane. The plus and minus signs correspond to

tensile and compressive stress, respectively. By using the values of s_0=0.2 and ε_0=0.04 for the shear and normal strains, the maximum of U' is reached when Θ=39.5° in tension and Θ=50.5° in compression.

Figure 2 suggests that the chemical driving force of the martensitic transformation decreases linearly with the increasing temperature. Thus, as indicated by equation 4, the stress level required to give the corresponding mechanical driving force also increases linearly. The linear relation has been shown to be valid up to the stress level corresponding to the yield strength of the austenite, which is illustrated in Figure 3. Bolling and Richman (1970) defined the corresponding temperature as the M_S^σ temperature. Below the M_S^σ temperature, the yielding can occur by means of the martensitic transformation, whereas at higher temperatures the transformation can take place only after the plastic deformation of the austenite phase.

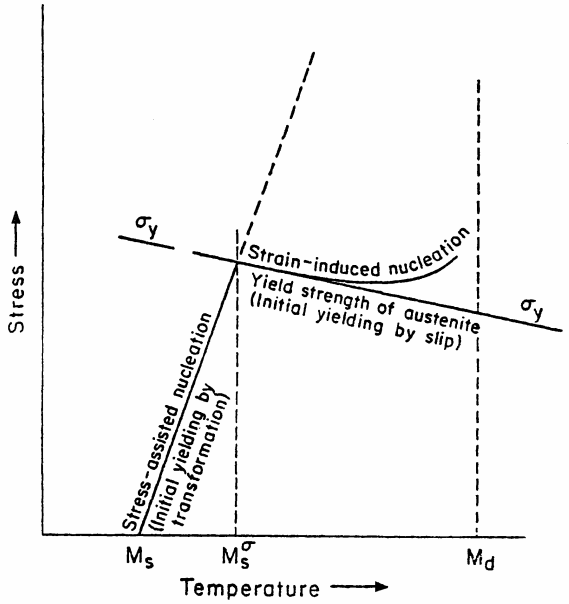

Figure 3 Schematic illustration of the critical stress to initiate martensitic transformation as a function of temperature (Olson and Cohen, 1972)

In order to distinguish between the behaviour below and above the M_S^σ temperature, Olson and Cohen (1972) established the concepts of *stress-assisted* and *strain-induced* martensitic transformations. The former occurs below the yield strength of the austenite phase with the aid of the applied stress, and the magnitude of the mechanical driving force is determined by equation 4. When the martensitic transformation occurs only after plastic deformation of the austenite phase, the transformation is referred to as strain-induced transformation. The upper limit for the strain-induced transformation is defined by the M_d temperature.

In the case of the strain-induced transformation, the nature of the mechanical driving force remains unclear. Olson and Cohen (1972) suggested that the plastic deformation of the austenite aids the transformation by the formation of energetically favourable nucleation sites for the martensite, which in addition to the effect of the applied stress enhances the transformation. In austenitic stainless steels, these nucleation sites have been shown to involve the intersections of shear bands, consisting of bundles of overlapping stacking faults, ε-martensite and mechanical twins. Lecroisey and Pineau (1972) found that although austenitic Fe-Ni and Fe-Ni-Cr alloys exhibited rather

comparable chemical driving forces $\Delta G^{\gamma\rightarrow\alpha'}$, the former showed a significantly lower difference between the M_S and M_d temperatures, *i.e.*, higher stability against the strain-induced martensitic transformation. This was explained in terms of the lower SFE of the Fe-Ni-Cr alloys, which enables the generation of energetically favourable nucleation sites, and thus, the occurrence of the strain-induced α'-martensite transformation at much higher temperatures. Suzuki *et al.* (1976) concluded that in the case of the strain-induced nucleation, it is not directly the external stress, but the internal stress due to the dislocations piled-up to the shear band intersections that produces the mechanical driving force. Fang and Dahl (1991) suggested that the mechanical driving force originates from the energy stored by the dislocations in the austenite.

1.2.3 Formation of stacking faults and ε-martensite

Intrinsic stacking faults form in the FCC crystal lattice as a consequence of the dissociation of a/2<110> perfect dislocations into two a/6<211> partial dislocations, referred to as Shockley partial dislocations. An intrinsic stacking fault is formed between the partials, and consequently, the stacking sequence of the {111} planes is changed from the regular ABCABCABC to, for instance, ABCACABCA. If two intrinsic stacking faults overlap on the successive {111} planes, the resulting stacking sequence will be ABCACBCAB, which has one excess plane with the C stacking. Such a fault is referred to as an extrinsic stacking fault.

Due to the low SFE, wide stacking faults are frequently observed in the microstructures of austenitic stainless steels. The width of the stacking fault (*e.g.*, the separation distance between the Shockley partial dislocations) is limited by the energy stored by the stacking fault. On the other hand, the Shockley partial dislocations repel each other due to their mutual interaction, which tends to broaden the fault. Cottrell (1953) proposed the following expression for the stacking fault width w:

$$w = \frac{G(b_2 \cdot b_3)}{2\pi\gamma} = \frac{Gb_p^{\,2}}{4\pi\gamma}, \tag{5}$$

where G is the shear modulus, b_2 and b_3 are the Burgers vectors of the Shockley partial dislocations, b_p is their absolute value and γ is the stacking fault energy. Kelly *et al.* (2000) suggested the following expression taking into account the angles between the unit vector of the perfect dislocation line and the Burgers vectors of the partial dislocations θ_1 and θ_2:

$$w = \frac{Gb_p^{\,2}}{2\pi\gamma}\left(\cos\theta_1\cos\theta_2 + \frac{\sin\theta_1\sin\theta_2}{1-\nu}\right), \tag{6}$$

where ν is Poisson's ratio.

In the case of an intrinsic stacking fault, the change in the stacking sequence of the {111} atom planes causes a thin layer of hexagonal close-packed phase with the stacking sequence of CACA. Therefore, even a single stacking fault can be regarded as a nucleus of HCP ε-martensite (Brooks *et al.*, 1979b), and the growth of the perfect ε-martensite occurs by the overlapping of the stacking faults on every second {111} plane (Venables, 1962; Fujita and Ueda, 1972; Brooks *et al.*, 1979a). Consequently, it is

difficult to distinguish between single stacking faults, bundles of overlapping stacking faults, and faulted or perfect ε-martensite. Therefore, a collective term "shear band" (Olson and Cohen, 1975) has often been used to designate the microstructural features originating from the formation and overlapping of stacking faults in austenitic stainless steels.

The orientation relationships between the austenite and ε-martensite are (Venables, 1962; Mangonon and Thomas, 1970a; Brooks *et al.*, 1979):

$\gamma\{111\} \parallel \varepsilon\{0001\}$

$\gamma\langle 110\rangle \parallel \varepsilon\langle 11\bar{2}0\rangle$.

Fujita and Ueda (1972) carried out a TEM examination on ε-martensite formation in 18Cr8Ni austenitic stainless steel. They found that once a single stacking fault was formed in the austenite, the other faults tended to form near the original fault. They attributed this to the minimisation of the total energy of the stacking faults. The mutual interaction of the extended dislocations on closely spaced slip planes was also found to affect the overlapping process. By this mechanism, the ε-martensite crystals were found to be initially highly faulted, but more perfect ε-martensite was formed as the deformation proceeded. A similar explanation was also proposed by Brooks *et al.* (1979).

Since even a single intrinsic stacking fault involves HCP stacking, the stacking fault energy may be regarded as a sum of surface and volume energy contributions (Olson and Cohen, 1976a; Rémy and Pineau, 1978; Miodownik, 1978; Ferreira and Müllner, 1998). Accordingly, the intrinsic stacking fault energy γ may be expressed as follows (Olson and Cohen 1976a):

$$\gamma = n^{*}\rho_{A}(\Delta G^{\gamma\to\varepsilon} + E^{str}) + 2\sigma(n), \qquad (7)$$

where n^{*} is the thickness of the fault in number of atom planes, ρ_A is the density of atoms in a close packed plane in moles per unit area, $\Delta G^{\gamma\to\varepsilon}$ is the chemical free-energy difference between the austenite and ε-martensite phases, σ(n) is the surface energy and E^{str} is strain energy, which in the case of $\gamma\to\varepsilon$ transformation is small. Based on equation 7, the overlapping process of the stacking faults and the energetics of the ε-martensite formation can be better understood. The surface energy component 2σ(n) has been estimated as 20 mJ/m^2 (Olson and Cohen, 1976a; Miodownik, 1978). When the SFE is below that value, $\Delta G^{\gamma\to\varepsilon}$ is negative, *i.e.*, the ε-martensite phase is thermodynamically more stable than the austenite phase (provided that E^{str} is neglected). Obviously, in such a condition the stacking faults tend to overlap so that perfect ε-martensite is formed.

Several authors have shown that the SFE of austenitic stainless steels increases with increasing temperature. These results are summarised in Table 1 and have been reviewed by Rémy and Pineau (1978). It is observed that for different chemical compositions the temperature coefficient of the SFE is consistently between 0.05 and 0.1 mJ/m^{2}K, the result of Murr *et al.* (1973) at high temperatures being the only exception. As the surface energy contribution of the SFE is relatively independent of the chemical composition (Miodownik, 1978) and only slightly affected by the temperature

(Olson and Cohen, 1976a), the temperature and compositional dependence of the SFE arises mainly from $\Delta G^{\gamma\rightarrow\varepsilon}$. Consequently, the temperature dependence $d\gamma/dT$ is proportional to the entropy difference between the austenite and ε-martensite phases (Rémy and Pineau, 1978).

Table 1 Temperature coefficients of intrinsic stacking fault energy $d\gamma/dT$ according to various references

Reference	Alloy	Temperature range (°C)	$d\gamma/dT$ (mJ/m^2K)
Latanision and Ruff (1971)	18%Cr-10%Ni	+25…+135	0.10
Latanision and Ruff (1971)	19%Cr-16%Ni	+25…+135	0.05
Abrassart (1972)	18%Cr-7%Ni-0.18%C	+20…+330	0.10
Lecroisey and Pineau (1972)	16%Cr-13%Ni-0.01%C	-150…+100	0.08
Lecroisey and Pineau (1972)	18%Cr-12%Ni-0.01%C	-150…+100	0.05
Gavriljuk *et al.* (1998)	18%Cr-16%Ni-10%Mn-0.4%C	-140…+20	0.06
Murr *et al.* (1973)	18%Cr-10%Ni-0.06%C	> +800	0.014

Rather conflicting information about the presence of the ε-martensite phase in deformed austenitic stainless steels has been reported. Significant fractions of ε-martensite have been found to form during the plastic deformation of AISI 304 steel at low temperatures (Guntner and Reed, 1962; Reed and Guntner, 1964; Mangonon and Thomas, 1970b; De *et al.*, 2004) and during room temperature cold rolling in AISI 301 steel (Bowkett *et al.*, 1982). In contrast, in some investigations (Narutani *et al.*, 1982; Narutani, 1989; Lichtenfeld *et al.*, 2006) ε-martensite was not found from the steels deformed in similar conditions. In the cases where ε-martensite was found to be present, it reached the highest volume fraction between the strains of 5 and 20%. At higher strains, the α'-martensite fraction increased at the expense of the ε-martensite.

1.2.4 Effect of applied stress on stacking faults

Two Shockley partial dislocations bounding a stacking fault can have different Schmid factors. As a consequence, the forces acting on the partial dislocations under a shear stress may be unequal, resulting in the stress-dependence of the stacking fault width. The role of the stress was first discussed by Smallman and Westmacott (1956). Later, it has been suggested that the stress-dependence of the stacking fault width may have a significant effect on the evolution of the deformation microstructures of FCC metals and alloys (Copley and Kear, 1968; Goodchild *et al.*, 1970; Kestenbach, 1977). Recently, Byun (2003) and Byun *et al.* (2003; 2004) demonstrated quantitatively the relationship between the SFE, stress level and the deformation microstructures of AISI 316 steel.

Copley and Kear (1968) determined the following expression for the stress-dependence:

$$\frac{1}{w} = \frac{1}{c}\left(\gamma \pm \frac{m_2 - m_1}{2}\sigma b_p\right), \tag{8}$$

where c is a constant depending on the material and the type of the perfect dislocation, γ is the SFE, m_1 and m_2 are absolute values of the Schmid factors of the leading and trailing partial dislocations, b_p their Burgers vector and σ uniaxial stress. The influence of the stress on the stacking faults was later illustrated by means of the transmission

electron microscope (TEM) studies by Goodchild *et al.* (1970) and Kestenbach (1977). Goodchild *et al.* (1970) found that fewer stacking faults and less ε-martensite were present in the grains oriented in <100> direction parallel to the tensile axis compared to the other grains. Similar findings were made also by Lagneborg (1964). Based on Copley's and Kear's expression, Kestenbach (1977) defined the effective stacking fault energy γ_{eff}:

$$\gamma_{eff} = \gamma \pm \frac{(m_2 - m_1)}{2}\sigma b_p . \tag{9}$$

Byun (2003) studied the effect of applied stress on stacking fault width, and proposed the following formula:

$$w = \frac{Gb_p^2}{\pi(2\gamma - \tau b_p|\sin\theta_2 - \sin\theta_1|)}(\cos\theta_1\cos\theta_2 + \frac{\sin\theta_1\sin\theta_2}{1-\nu}), \tag{10}$$

where θ_1 and θ_2 are the angles between the Burgers vectors of the leading and trailing partial dislocations and the unit vector of the perfect dislocation line, and ν is Poisson's ratio. In the absence of stress, Byun's equation becomes equivalent with equation 6.

In order to validate equation 10, Byun *et al.* (2003; 2004) carried out TEM examinations on deformed AISI 316LN steel. It was shown that the observed deformation microstructures could be categorised in terms of the applied stress level. At low stress levels, the microstructures were dominated by tangled perfect dislocations, whereas at higher stress levels the microstructures contained large amounts of wide stacking faults and twins. It was concluded that the applied stress accounted for the observed differences according to equation 10. As the stress level increased, the stress promoted the slip planarity and the presence of stacking faults. A limitation of the analysis was, however, that the SFE of the studied steel was not known.

1.2.5 Deformation twinning

The plastic deformation of austenitic stainless steels may involve deformation twinning. A mechanical twin is formed by the overlapping of intrinsic stacking faults, *i.e.*, by the glide of Shockley partials of the same sign on successive {111} planes (Lecroisey and Pineau, 1972; Lee *et al.*, 2001). Recalling section 1.2.3, a fault consisting of two overlapping intrinsic stacking faults on successive {111} planes is referred to as an extrinsic stacking fault, which therefore is a twin nucleus. If the overlapping of the intrinsic stacking faults proceeds on successive {111} planes, the twin grows in thickness. Lecroisey and Pineau (1972) found that in 16/11, 16/13 and 18/12 type austenitic alloys the deformation twins occurred along with ε-martensite. They observed that with increasing temperature and strain the number of the twins increased, and attributed this to the increase in the SFE with increasing temperature. Bowkett *et al.* (1982) compared the deformation microstructures of AISI 301 and 316 steels. In the former stacking faults and mechanical twins were present, whereas in AISI 316 steel only twins were found. This was explained by the higher stacking fault energy of the AISI 316 steel. Ferreira *et al.* (2004) found that high strain rate promoted the deformation twinning in AISI 304 steel, and also increased the number of twin variants from one to two.

Deformation twinning has been found to be a preferred mechanism of plastic deformation in nitrogen alloyed austenitic stainless steels at high strains and stress levels. Müllner *et al.* (1993) studied the deformation microstructures of AISI 316L steels with nitrogen contents between 0.04 and 0.53 wt%. They observed that the onset of twinning was shifted to higher stresses and lower strains as the N content increased. This was explained in terms of the solid solution strengthening caused by N and due to the reduced SFE. The twinning was always found to be preceded by planar glide.

Byun (2004) suggested that the stress-dependence of the stacking fault width discussed in the previous section might determine the critical stress for twinning. By using the average Schmid factor of 0.326, the critical stress for twinning is obtained from equation 10 as follows:

$$\sigma_T = 6.14\frac{\gamma}{b_p}. \tag{11}$$

However, Byun's model predicts that the twinning becomes more difficult as SFE increases. This conflicts with the findings of Lecroisey and Pineau (1972) and Bowkett *et al.* (1982), who found that twinning was favoured by the high SFE. Lecroisey and Pineau suggested that the ε-martensite formation is preferred to the twinning when:

$$\frac{\gamma_0 - \gamma(1-x)}{Gb_p} > \sqrt{2}\xi^2 \pm 2\sqrt{2}\xi\frac{\sigma}{G}, \tag{12}$$

where γ_0 is the intrinsic stacking fault energy at the temperature where $\Delta G^{\gamma\rightarrow\varepsilon}=0$ (*i.e.*, $\gamma=2\sigma(n)$ according to equation 7), x is a factor representing the ratio of the extrinsic and intrinsic stacking fault energies and ξ is the contraction normal to the basal plane due to the $\gamma\rightarrow\varepsilon$ transformation. In more general terms, the ε-martensite formation is preferred when $\Delta G^{\gamma\rightarrow\varepsilon}$ is small or even negative, as the process involves the formation of the HCP structure of lower energy compared to a twin having the FCC stacking. When $\Delta G^{\gamma\rightarrow\varepsilon}$ increases, the formation of the HCP structure becomes more difficult, and consequently, twinning is preferred.

The discussion presented above is summarised in the schematic diagram defined for austenitic Fe-Mn-Cr-C alloys by Remy and Pineau (1977), presented in Figure 4.

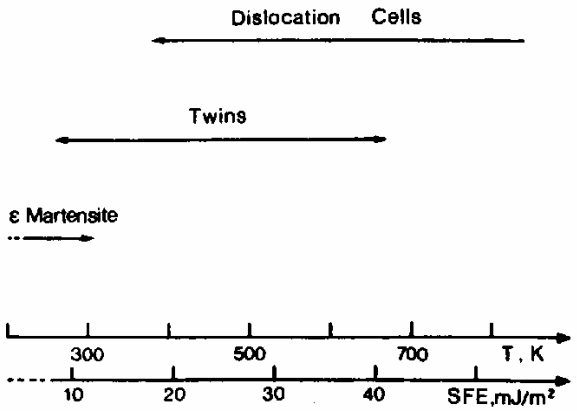

Figure 4 Effect of temperature and stacking fault energy on the deformation microstructures of austenitic Fe-Mn-Cr-C alloys (Remy and Pineau, 1977)

The twinning was found to be an intermediate mode of deformation between the formation of ε-martensite and dislocation cells, corresponding to the SFEs of 10-40 mJ/m^2. Austenitic Co-Ni-Cr-Mo alloys were found to show essentially equivalent behaviour (Remy and Pineau, 1976).

1.2.6 Strain-induced α'-martensite transformation

It has been shown that the BCC α'-martensite phase nucleates at the intersections of the shear bands (Venables, 1962; Lagneborg, 1964; Reed and Guntner, 1964; Kelly, 1965; Mangonon and Thomas, 1970a; Suzuki *et al.*, 1977; Brooks *et al.*, 1979a; Brooks *et al.*, 1979b; Bowkett *et al.*, 1982; Murr *et al.*, 1982). However, some researchers have found the α'-martensite nucleation to take place also within single shear bands (Lee and Lin 2000; Gey *et al.*, 2005). As the shear bands in fact consist of more or less perfect ε-martensite phase, it has been regarded as an intermediate phase in the formation of α'-martensite. Some researchers (Narutani *et al.*, 1982; Narutani, 1989; Lichtenfeld *et al.*, 2006) have reported that the α'-martensite transformation took place without the presence of ε-martensite. However, these findings were based on X-ray diffraction (XRD) measurements. Therefore, ε-martensite phase was probably not absent, but the XRD technique is just unable to detect relatively small fractions of finely dispersed and highly faulted ε-martensite, or the shear bands consisting of mechanical twins.

The orientation between the austenite and α'-martensite phases has been shown to obey the Kurdjumov-Sachs relationship, *i.e.* (Venables, 1962; Lagneborg, 1964; Kelly, 1965; Mangonon and Thomas, 1970a; Murr *et al.*, 1982):

$\gamma\{111\} \parallel \alpha'\{110\}$

$\gamma\langle 110\rangle \parallel \alpha'\langle 111\rangle$.

Mangonon and Thomas (1970a) found that initially the relationship was the Nishiyama, *i.e.*:

$\gamma\{111\} \parallel \alpha'\{110\}$

$\gamma\langle 211\rangle \parallel \alpha'\langle 110\rangle$,

and changed to the Kurdjumov-Sachs as the transformation proceeded. Bowkett *et al.* (1982), however, claimed that it is not possible to distinguish between these two relationships based on the selected-area electron diffraction technique. Recently, the electron backscatter diffraction (EBSD) was utilised to study the orientation relationships (Gey *et al.*, 2005), and Kurdjumov-Sachs relationship was found.

The mechanisms of the α'-martensite nucleation at the shear band intersections have been discussed in numerous investigations. In general, the α'-martensite nucleation involves a process by which an array of Shockley partial dislocations, *i.e.*, another shear band, can penetrate through the other shear band. Olson and Cohen (1972; 1976b) discussed the nucleation of α'-martensite based on the work of Bogers and Burgers (1964). Bogers and Burgers suggested that the BCC structure can be generated from FCC by two successive shears, the first involving a 1/3 FCC twinning shear of austenite and the other a 1/2 FCC twinning shear, referred to as T/3 and T/2, respectively. Olson

and Cohen rationalised the T/3 shear by the spreading of an array of a/6<112> Shockley partial dislocations on every third {111} plane and the T/2 by the spreading of the Shockley partial dislocations on every second {111} plane. As the movement of the Shockley partial dislocations on every second {111} plane produces perfect ε-martensite, Olson and Cohen suggested that an α'-martensite nucleus is formed by the passage of a T/3 shear through an ε-martensite platelet. Since a significant chemical driving force is available, the process transforms the stacking of the atoms from FCC to BCC, and enables the partial dislocations to penetrate through the ε-platelet. Furthermore, the role of the SFE in the nucleation process was discussed. With increasing SFE, the probability of the presence of appropriate arrays of the partial dislocations decreases. Thus, the probability of α'-martensite nucleation is decreased. The intersection of an ε-platelet with a mechanical twin was also thought to be a possible mechanism for α'-martensite nucleation, but the process was considered to require a higher chemical driving force.

Lecroisey and Pineau (1972) considered the case in which a Shockley partial dislocation gliding on the austenite $(1\bar{1}\bar{1})$ plane crosses a deformation twin on the austenite (111) plane. In this case, the plastic deformation associated to the Shockley partial dislocation can propagate in the twin by the following dislocation reaction:

$$\frac{1}{6}\left[1\bar{2}\bar{1}\right] \rightarrow \frac{1}{6}\left[\bar{2}1\bar{1}\right]_t + \frac{1}{18}\left[\bar{1}\bar{1}2\right]_t, \tag{13}$$

where the subscript t indicates that the Burgers vectors are given in the coordinate system of the twin. Alternatively, in the case of a 1/6[112] partial dislocation the following reaction may occur:

$$\frac{1}{6}\left[112\right] \rightarrow \frac{1}{6}\left[112\right]_t + \frac{1}{9}\left[\bar{1}\bar{1}2\right]_t. \tag{14}$$

Both reactions result in the formation of an α'-martensite nucleus with BCC stacking at the shear band intersection, and involve the propagation of the plastic deformation. Furthermore, both reactions require additional energy, since the total self-energy of the dislocations is increased. This additional energy was considered to originate from the chemical free-energy difference of the α'-martensite and austenite phases. The reactions were also assumed to be aided by the stress concentrations due to the piling-up of the partial dislocations.

Suzuki *et al.* (1977) referred to the nucleation of the α'-martensite at the shear band intersection as a "window effect", by which the two shear bands, otherwise being barriers to each other, can easily intersect. Brooks *et al.* (1979a; 1979b) suggested that the α'-martensite nucleation is associated with the piling-up of the Shockley partial dislocations. As the dislocations are forced closer to each other in the pile-up, the atomic structure starts to resemble BCC stacking. As the pile-up reaches the critical size, a rapid growth of an α'-martensite nucleus occurs with the aid of the chemical driving force. Olson and Cohen (1976b) determined the critical size for the martensitic embryo as follows:

$$n^{CR} = \frac{2\sigma(n)}{-\rho_A(\Delta G^{\gamma\rightarrow\alpha'} + E^{str})}, \quad (15)$$

where n^{CR} is the thickness of the embryo in atom planes, $\sigma(n)$ is the embryo interfacial energy per unit area, ρ_A is the density of atoms in moles per unit area in a close packed plane, $\Delta G^{\gamma\rightarrow\alpha'}$ is the chemical free-energy difference between the austenite and α'-martensite phases and E^{str} the strain energy due to the transformation strains. For a Fe30Ni austenitic alloy Olson and Cohen (1976b) calculated the critical embryo size of 13.5 close-packed atom planes by using the values of $\Delta G^{\gamma\rightarrow\alpha'}$=-1260 J/mol, E^{str}=500 J/mol and $\sigma(n)$=0.15 J/m^2. Staudhammer *et al.* (1983) used the $\Delta G^{\gamma\rightarrow\alpha'}$ and E^{str} values suggested by Olson and Cohen, but a two times higher surface energy value of 0.3 J/mol, which resulted in the critical embryo thickness of 27 planes, corresponding to the thickness of about 57 Å. In order to validate the calculation, a TEM examination of the α'-martensite embryos in tensile strained AISI 304 steel was carried out. The minimum embryo size was found to be indeed 50-70 Å. Therefore, evidently, the α'-martensite cannot nucleate at the intersections of single stacking faults, but significant overlapping of the stacking faults and piling-up of the Shockley partial dislocations must occur before the α'-martensite nucleation is possible.

The growth of the α'-martensite phase has been found to occur through the continuous nucleation and coalescence of α'-martensite embryos (Murr *et al.*, 1982; Staudhammer *et al.*, 1980; Staudhammer *et al.*, 1983). Murr *et al.* (1982) observed that the α'-martensite nucleates not necessarily throughout the whole shear band intersection volume, but only within certain regions. As a result, the α'-martensite was concluded to exhibit irregular and blocky morphology. In a polycrystalline steel, the α'-martensite content varies from grain to grain depending on the grain orientation (Gey *et al.*, 2005), which is probably attributed to the dependence of the shear band formation and α'-martensite nucleation on the local stress field.

1.3 Factors affecting strain-induced α'-martensite transformation

The extent of the strain-induced α'-martensite transformation is significantly affected by several factors, including the chemical composition, temperature, strain rate, strain state and the grain size of the austenite phase. The variation in the α'-martensite transformation has been shown to have a substantial influence on the mechanical response of metastable austenitic stainless steels. Thus, thorough understanding of the role of each factor is essential when using the steels in engineering applications.

1.3.1 Effect of chemical composition

Alloying makes austenitic stainless steels more stable against the strain-induced α'-martensite transformation. This is a consequence of the alteration of the stacking fault energy and the chemical driving force $\Delta G^{\gamma\rightarrow\alpha'}$. Several empirical formulas have been determined in order to describe the influence of the chemical composition on the tendency to the strain-induced α'-martensite transformation. The first formula was determined by Angel (1954):

$$M_{d30}(°C) = 413 - 462(\%C + \%N) - 9.2\%Si - 8.1\%Mn - 13.7\%Cr - 9.5\%Ni - 18.5\%Mo, \quad (16)$$

where the alloy contents are in weight percent. The M_{d30} temperature represents the temperature at which 50% α'-martensite phase is formed after true tensile strain of 0.3. Nohara *et al.* (1977) modified Angel's equation and included the effect of grain size. As a result, the following formula was obtained:

$$M_{d30}(°C) = 551 - 462(\%C + \%N) - 9.2\%Si - 8.1\%Mn - 13.7\%Cr - 29(\%Ni + \%Cu) - 18.5\%Mo - 68\%Nb - 1.42(GS - 8), \quad (17)$$

where GS is the ASTM grain size number.

1.3.2 Effect of temperature

Above discussion suggests that the formation of strain-induced α'-martensite is affected by two composition-dependent parameters, namely, by the stacking fault energy and the chemical driving force $\Delta G^{\gamma\rightarrow\alpha'}$. Since both of these parameters are also temperature-dependent, the tendency to the strain-induced α'-martensite transformation is sensitive to the temperature, as well. It is well known that the α'-martensite transformation is suppressed with increasing temperature (Angel, 1954; Powell *et al.*, 1958). An example of the temperature dependence found by Angel (1954) is shown in Figure 5. The behaviour is normally attributed to the decrease in the chemical driving force $\Delta G^{\gamma\rightarrow\alpha'}$ with increasing temperature, as indicated in Figure 2. In contrast, although the SFE is known to increase with increasing temperature (Table 1), its role in the suppression of the α'-martensite transformation has not been explicitly demonstrated in literature.

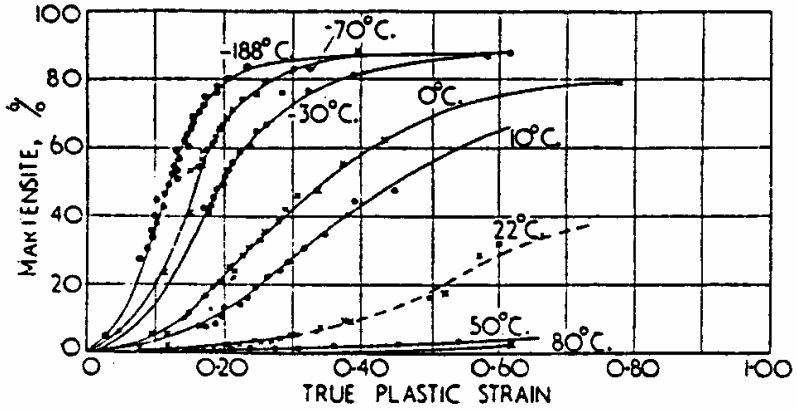

Figure 5 Effect of deformation temperature on formation of strain-induced α'-martensite phase during uniaxial tensile deformation of 18/8-type austenitic stainless steel (Angel, 1954)

1.3.3 Effect of strain and stress state

The extent of the α'-martensite transformation is dependent on the stress and strain state. Powell *et al.* (1958) found that the strain-induced α'-martensite transformation was more rapid under tensile strain compared to compressive strain. Iwamoto *et al.* (1998) found that in compression the transformation rate was initially higher than in

tension, but at higher strains the relation was reversed. Hecker *et al.* (1982) found that more α'-martensite was formed in biaxial tension than in uniaxial tension, when the comparison was made against the maximum principal strain. However, when the comparison was based on the von Mises effective strain, the biaxial and uniaxial tension showed similar trends in α'-martensite formation. This was explained by Murr *et al.* (1982), who found that a higher number of shear band intersections was generated in biaxial tension. Obviously, there are more active slip systems in biaxial tension, which results in a higher number of shear band intersections. Shrinivas *et al.* (1995) reported that in AISI 316 steel cold rolling caused more α'-martensite than uniaxial tension. This was related to the multiple slip systems being activated during rolling.

1.3.4 Effect of austenite grain size

Gonzáles *et al.* (1992) studied the effect of austenite grain size on the strain-induced α'-martensite transformation in AISI 304 steel. The transformation was found to be enhanced by large grain size. This finding is in agreement with Nohara *et al.* (1977) and equation 17, which indicates that the M_{d30} temperature increases with increasing grain size. Also Varma *et al.* (1994) found that large grain size promoted the α'-martensite formation during tensile and cold rolling deformation of AISI 304 and 316 steels. In contrast, Shrinivas *et al.* (1995) found that the formation of α'-martensite during cold rolling increased with decreasing grain size in AISI 304 steel and was grain size independent in AISI 316 steel.

1.3.5 Effect of strain rate

Most investigations carried out in order to clarify the effect of strain rate on the strain-induced α'-martensite transformation have indicated that the transformation is suppressed with increasing strain rate. This has been mostly explained in terms of the adiabatic heating, which decreases the chemical driving force of the transformation (Powell *et al.*, 1958; Bressanelli and Moskowitz, 1966; Neff *et al.*, 1969; Livitsanos and Thomson, 1977; Ferreira *et al.*, 2004). However, Staudhammer *et al.* (1983) suggested that high strain rate may promote more irregular shear band arrays compared to the low strain rate. This may lead to a reduced probability of formation of α'-martensite embryos of the critical size, and thus, suppress the formation of α'-martensite.

On the other hand, it has been found that high strain rate (10^3 s^{-1}) promoted shear band formation in AISI 304 steel compared to the low strain rate (10^{-3} s^{-1}). This led to an increased number of shear band intersections and higher volume fraction of α'-martensite at the early stages of tensile deformation, as illustrated in Figure 6 (Staudhammer *et al.*, 1980; Hecker *et al.*, 1982; Murr *et al.*, 1982). However, at strains higher than 0.25, the α'-martensite transformation was suppressed at the high strain rate. This was attributed to a decrease in the chemical driving force of the transformation due to adiabatic heating.

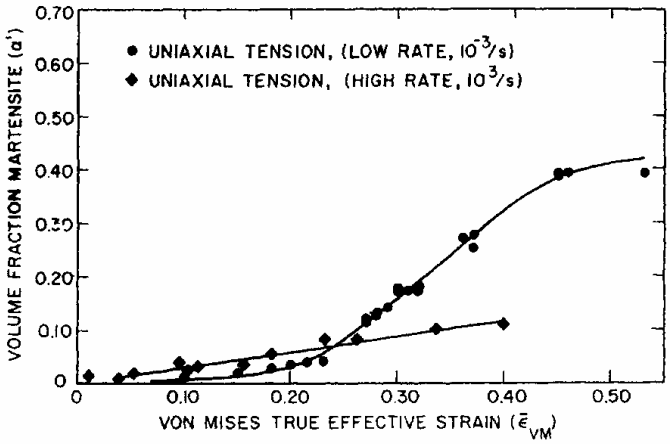

Figure 6 Effect of strain rate on the formation of strain-induced α'-martensite in AISI 304 austenitic stainless steel strained in uniaxial tension (Hecker *et al.*, 1982)

Lee and Lin (2000; 2001; 2002) studied the strain-induced α'-martensite transformation in AISI 304L steel deformed in compression at strain rates ranging between 10^{-3} and 5×10^{3} s^{-1}. Based on TEM examinations, they suggested that the formation of the shear bands was promoted at the high strain rates. Also the volume fraction of the α'-martensite increased with the increasing strain rate. However, due to the high austenite stability of the studied steel, the observed α'-martensite volume fractions were lower than 0.04 and had negligible influence on the mechanical response of the steel.

Ferreira *et al.* (2004) found that a high strain rate promoted the formation of stacking faults and ε-martensite in AISI 304 steel, but suppressed the α'-martensite transformation. It was suggested that the nucleation and movement of partial dislocations was easier at the high strain rates. Therefore, it would be a preferential deformation mode compared to the movement of perfect dislocations. The suppression of the strain-induced α'-martensite transformation was attributed to adiabatic heating.

1.4 Effect of strain-induced α'-martensite transformation on mechanical properties

The influence of microstructural evolution on the mechanical properties of austenitic stainless steels has been a subject of numerous investigations from the 1950's. Although the high work-hardening capacity of austenitic stainless steels has been related to the low stacking fault energy and to the consequent slip planarity, the formation of stacking faults, deformation twins and ε-martensite (*e.g.*, Hecker *et al.*, 1982; Lee and Lin, 2001; Byun *et al.*, 2004), undoubtedly the α'-martensite transformation plays a key role in the mechanical behaviour of metastable austenitic steels. Zackay (1967) suggested that the steels, whose mechanical properties are characterised by the enhancement in the strength and ductility by the strain-induced α'-martensite transformation, could be referred to as TRIP (Transformation-Induced Plasticity) steels. At present, the term "TRIP effect" is widely used to denote the strain-induced α'-martensite transformation itself and its influence on the mechanical behaviour. Furthermore, a group of mild steels have been labelled as "TRIP steels" according to their tendency to transform from the retained austenite to the strain-induced martensite.

1.4.1 Effect of α'-martensite transformation on flow stress and work hardening

The strain-induced α'-martensite transformation is associated with a strong increase in the work-hardening rate (Guntner and Reed, 1962; Reed and Guntner, 1964; Neff *et al.*, 1969; Lecroisey and Pineau, 1972; Huang *et al.*, 1989; Fang and Dahl, 1991; Byun *et al.*, 2004). Consequently, the formation of the strain-induced α'-martensite increases the tensile strength. When the work-hardening rate of metastable steel exhibiting the transformation is plotted as a function of strain, the curve has been found to show first a minimum and then a subsequent maximum (Huang *et al.*, 1989; Fang and Dahl, 1991). Examples of the work-hardening curves of EN 1.4306 (AISI 304L) steel at different temperatures are shown in Figure 7.

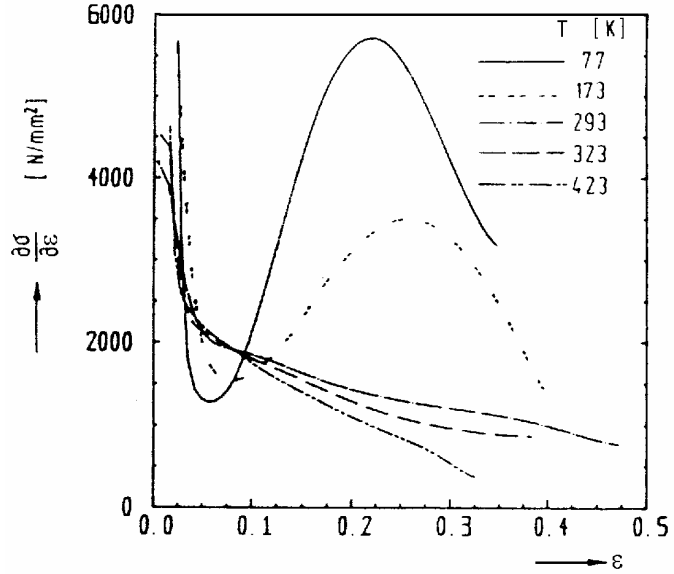

Figure 7 Effect of deformation temperature on the work-hardening rate of austenitic stainless steel EN 1.4306 (AISI 304L) as a function of true strain (Fang and Dahl, 1991)

The behaviour is often referred to as the abnormal work hardening, or as the work-hardening abnormality, since it differs from the behaviour of the most metals and alloys showing continuously decreasing work-hardening rate. The work-hardening maximum has been related to the formation of the α'-martensite phase. As the extent of the α'-martensite transformation is temperature-dependent, the work-hardening rate also exhibits a pronounced variation with temperature, as illustrated in Figure 7.

Another characteristic of the work-hardening behaviour of metastable steel grades is the minimum that is reached before the maximum. The work-hardening minimum has been attributed to the formation of ε-martensite (Reed and Guntner 1964; De *et al.*, 2006). This view was criticised, for instance, by Suzuki *et al.* (1976; 1977), who attributed the low work-hardening rate to the onset of the α'-martensite transformation. Later, the effect has been referred to as a dynamic softening effect, originating from the α'-martensite transformation acting as an additional deformation mechanism along with the slip deformation (Narutani *et al.*, 1982; Olson and Cohen, 1986; Huang *et al.*, 1989). Fang and Dahl (1991) related the effect only to the volume change occurring during the transformation.

1.4.2 Effect of α'-martensite transformation on ductility

Numerous studies have focussed on the understanding of the influence of the TRIP effect on the ductility. Although some researchers have explained the enhanced ductility in terms of the excessive formation of deformation twins and stacking faults, the most widely accepted view is that the α'-martensite transformation governs the ductility. Furthermore, it has been shown that it is not the total amount but the rate and the point at which the α'-martensite transformation takes place, which is important (Powell *et al.*, 1958; Bressanelli and Moskowitz, 1966; Neff *et al.*, 1969; Sanderson and Llewellyn, 1969; Rosen *et al.*, 1972; Livitsanos and Thomson, 1977; Huang *et al.*, 1989). Consequently, when the uniform or total elongation of a metastable austenitic stainless steel is plotted as a function of the deformation temperature, the curve exhibits a peak value, as shown in Figure 8.

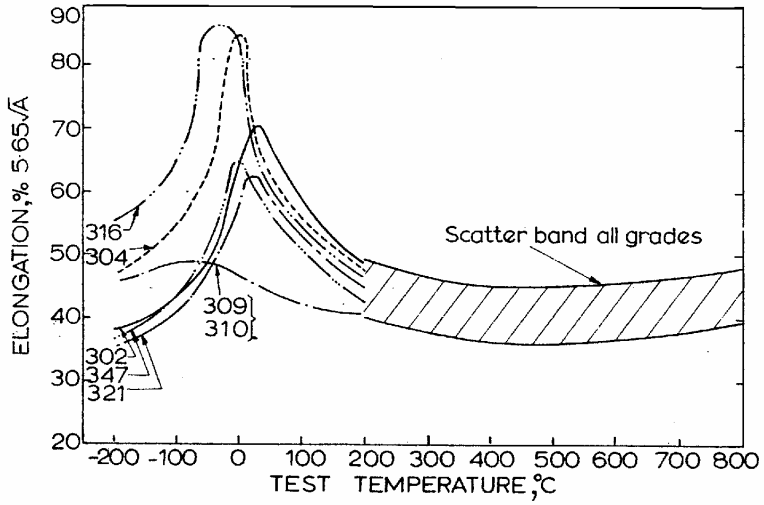

Figure 8 Influence of deformation temperature on the elongation to fracture of various austenitic stainless steel grades (Sanderson and Llewellyn, 1969)

The behaviour reflects the temperature dependence of the austenite stability. Maximum uniform elongation is reached when the highest α'-martensite transformation rate and the associated work-hardening peak occur at high strain levels (Olson and Cohen, 1986; Huang *et al.*, 1989; Tsuchida and Tomota, 2000; Iwata and Tsuta, 2000; Tomota *et al.*, 2004). On the right hand side of the elongation peak the temperature is such that the transformation is prevented, and as a consequence, the elongation is reduced. At the lower temperatures, *i.e.*, on the left side of the elongation peak, the α'-martensite transformation occurs rapidly, resulting in rapid work hardening at low strains and consequent premature fracture.

Although in some studies the high elongation of the steels exhibiting the TRIP effect has been explained in terms of the transformation strain (Cherkaoui *et al.*, 2000), it has been claimed that neither the transformation strain nor the volume change related to the transformation can alone account for the enhanced ductility. Bhadeshia (2002) showed with a simple theoretical study that if austenitic steel is fully transformed to martensite, the elongation due to the transformation strain can be only 15% maximum. Narutani *et al.* (1982) carried out tensile testing of metastable austenitic steel at -196°C at which stress-assisted transformation took place. They found that the slope of the strain vs. α'-martensite volume fraction curve had a constant value of 0.12, which corresponds to the

transformation strain of 0.12 when the aggregate is fully transformed to martensite. Higher variation of the total elongation resulting from the altering transformation behaviour can be seen in Figure 8, indicating that beyond the transformation strain alone, also another mechanism accounting for the improved ductility must be operative.

Although it has been suggested (Bressanelli and Moskowitz, 1966) that reduced ductility at low temperatures may be due to the brittleness of the α'-martensite, the SEM examinations of the fracture surfaces have shown that the failure mechanism in the austenitic stainless steels is always ductile dimple type (Hecker *et al.*, 1982). Furthermore, Ilola (1999) compared the impact toughness of various austenitic Cr-Mn and Cr-Ni austenitic steels. AISI 304LN steel, showing the lowest austenite stability, exhibited the best impact toughness, and did not have the ductile to brittle transition at all.

1.4.3 Strengthening mechanisms

Significant inconsistency still exists in explaining the strengthening mechanisms of metastable austenitic stainless steels and the strengthening effect of the strain-induced α'-martensite phase. The most widely accepted view is that the flow stress of metastable austenitic steel is controlled by 1) the static hardening effect of the α'-martensite phase and 2) the dynamic softening effect due to the transformation strain (*i.e.*, due to the operation of the α'-martensite transformation as an alternative deformation mechanism) (Narutani *et al.*, 1982; Olson and Cohen, 1986). Some authors have distinguished between the strengthening effects of the dislocation substructures in the austenite phase and the direct strengthening effect of the α'-martensite phase (Huang *et al.*, 1989; Lee and Lin, 2001; Byun *et al.*, 2004). Since the highly dislocated α'-martensite phase is much harder than the austenite phase, the austenite-martensite mixtures have been regarded as composites of soft austenitic matrix with hard martensite dispersions (Mangonon and Thomas, 1970b; Tamura, 1982). Mangonon and Thomas (1970b) found a linear relationship between the yield strength and α'-martensite volume fraction, and suggested that the flow stress of an austenite-martensite mixture is best described with a rule of mixtures. The high strength and the direct strengthening effect of the α'-martensite phase was demonstrated by Spencer *et al.* (2004), who carried out *in-situ* neutron diffraction stress measurements during the uniaxial tensile testing of stable AISI 316L steel at room temperature. Before the tensile testing, the test material was pre-strained at 77 K, which resulted in the α'-martensite content of 30%. The stress measurements indicated that the α'-martensite phase sustained a clearly higher stress than the austenite phase. Therefore, the α'-martensite was concluded to act as the reinforcing phase.

Guimarães and De Angelis (1974) developed a model based on an assumption that the ledges on the semi-coherent austenite/martensite interfaces act as sources of dislocations in the austenite. Accordingly, they assumed that the martensite transformation affects the flow stress by increasing the dislocation density of the austenite phase. The model was verified with the experimental data of Fe-Ni-C-alloy. Eckstein and Guimarães (1984) carried out quantitative microscopy and mechanical testing on Fe-Ni-C austenite-martensite mixtures. They concluded that the martensite phase acts as hard dispersions within the soft austenitic matrix. The plastic deformation was found to take place mainly in the austenite, and the strengthening contribution of the martensite was related to the decrease in the effective grain size of the austenite with increasing

martensite content. Narutani (1989) showed that the linear relationship between the flow stress and the square root of the dislocation density of the austenite phase of AISI 301 steel remained valid up to α'-martensite content of 20%. Furthermore, the dislocation density of the α'-martensite was found to be much higher than that of the austenite. It was concluded that below the α'-martensite content of 20% the formation of α'-martensite strengthens the steels by accelerating the dislocation generation in the austenite phase. This was attributed to the accommodation of the volume expansion related to the transformation. At the higher martensite contents, the strengthening was related to the "hardening effect of the martensite by itself", which was, however, not further explained.

1.5 Constitutive equations and modelling of strain-induced α'-martensite transformation

Modelling of the kinetics of the strain-induced transformation and the resulting mechanical response has been of interest since the discovery of the TRIP effect. The development of the constitutive equations has become more and more important due to the growing use of FEM in the engineering applications, for example, in the automotive industry. FEM simulation necessitates an accurate constitutive equation capable to predict the material behaviour. In the case of metastable steels, this is not straightforward due to the complex interaction between the external conditions, microstructural evolution and mechanical response. The kinetic models and constitutive equations for metastable steels reported in literature are discussed in the following section. Furthermore, during the recent years the mechanisms of the TRIP effect have been a subject of numerous investigations performed in the fields of micromechanical modelling and continuum mechanics. This topic is briefly reviewed in section 1.5.2.

1.5.1 Macroscopic models

Ludwigson and Berger (1969) made one of the first attempts to model the kinetics of the strain-induced α'-martensite transformation and the stress-strain curves of metastable austenitic stainless steels. They assumed that the α'-martensite volume fraction is a continuous function of strain, and that the strength of both the austenite and α'-martensite phases contribute to the flow stress. Probably the best known model to predict the kinetics of the strain-induced α'-martensite transformation was developed by Olson and Cohen (1975). They presumed that the α'-martensite is nucleated at the shear band intersections, and that the nucleation and growth process of α'-martensite is controlled by two parameters, α_{OC} and β_{OC}. As a result, the following equation for the α'-martensite volume fraction $f^{\alpha'}$ as a function of true plastic strain ε was obtained:

$$f^{\alpha'} = 1 - \exp(-\beta_{OC}(1 - \exp(-\alpha_{OC}\varepsilon))^n). \quad (18)$$

The parameter α_{OC} controls the rate of the shear band formation. It was assumed to be dependent on the stacking fault energy and strain rate. The parameter β_{OC} is proportional to the probability that the α'-martensite is nucleated at a shear band intersection, and it is dependent on the chemical driving force and temperature. The exponent n describes the rate of the formation of the shear band intersections, and it was

found to have the constant value of 4.5. The model predicts a sigmoidal $f^{\alpha'}$ vs. ε curve, and it has been shown to agree well with the experimental data.

Later, numerous researchers have further developed the Olson-Cohen model or developed alternative kinetic models. The Olson-Cohen kinetic model has been a basis for numerous attempts to develop constitutive equations. Stringfellow *et al.* (1992), based on the work of Olson and Cohen, developed a kinetic model and a constitutive equation taking into account the deformation temperature, plastic strain and stress state. Tomita and Iwamoto (1995) generalised the model of Stringfellow *et al.* by including the effects of the strain rate and adiabatic heating. Later, the model was further developed by adding the effect of stress state (Iwamoto *et al.*, 1998). Iwamoto and Tsuta (2000) modified the Olson-Cohen model by taking into account the effect of austenite grain size. Serri *et al.* (2005a; 2005b) utilised Iwamoto's and Tsuta's transformation kinetics model in the simulation of sheet metal forming of AISI 304 steel. Lichtenfeld *et al.* (2006) applied the Olson-Cohen model to high strain rate deformation by taking into account the variation of the parameters α and β with temperature. Shin *et al.* (2001) proposed a new kinetic model, which considers the strain-induced transformation as a relaxation process of internal strain energy, aiding the chemical driving force.

Narutani *et al.* (1982) developed a constitutive model for the flow stress based on the rule of mixtures. The model included a correction for the dynamic softening effect due to the α'-martensite formation. Cortés *et al.* (1992) developed a constitutive equation for the flow stress by using an energetic criterion. The model was based on the assumption that the sum of the energies consumed to deform each phase is equal to the total energy consumed to deform the aggregate. The model was extended to take into account multiaxial loading by Tsuta and Cortés (1993). Hänsel *et al.* (1998) developed a non-isothermal model for the transformation kinetics that took into account the adiabatic heating during the deformation. Based on the kinetic model, a work-hardening model was established by using the rule of mixtures to determine the sum of the work-hardening contributions of both phases. The model was applied to the simulation of deep drawing process. Schedin *et al.* (2004) implemented the model in FEM simulation of sheet metal stamping.

1.5.2 Micromechanical and mesoscopic modelling

In addition to the macroscopic modelling of the transformation kinetics and development of the constitutive equations, the strain-induced martensitic transformations and TRIP effect have been investigated in terms of micromechanical or continuum modelling in micro- and mesoscales. Some work carried out on this field is briefly reviewed in the following.

Levitas *et al.* (1999) performed numerical modelling of the strain-induced nucleation of the α'-martensite at the shear band intersections based on the previously developed mesoscopic continuum thermomechanical theory (Levitas, 1998). It was shown that the model was able to predict the well-known features of the strain-induced transformation: the nucleation event took place at the shear band intersections during the intersection events. Furthermore, it was shown that the nucleation occurred sequentially in the presence of multiple intersections. A more fundamental approach was taken by Cherkaoui *et al.* (1998; 2000), who carried out micromechanical modelling of the strain-induced martensitic transformation. The model developed was able to predict the

stress-strain behaviour and the martensite volume fractions as a function of strain. Furthermore, the model was utilised in the prediction of deformation textures of AISI 304 steel (Kubler *et al.*, 2003; Petit *et al.*, 2005). In addition to the research mentioned above, micromechanical modelling of the TRIP effect has been carried out also by, for instance, Diani *et al.* (1995), Tsuchida and Tomota (2000), Fischer *et al.* (2000), Han *et al.* (2004) and Garion *et al.* (2002; 2006).

2 AIMS OF THE STUDY

The research work presented in this thesis was started as a part of the Fifth European Community Framework Programme project LIGHT&SAFE, which aimed to study the usability of austenitic stainless steels in crash-relevant parts of passenger cars. The LIGHT&SAFE project focussed on metastable steel grades exhibiting the TRIP effect, since these grades show high strength and work-hardening capacity, making them attractive materials in terms of crashworthiness.

During sheet metal forming and a car crash, high strain rates occur. Adiabatic heating at the high strain rates may also cause a substantial increase in temperature. Therefore, the present work concentrated on the effects of the strain rate and temperature on the microstructural evolution of metastable austenitic stainless steels and on the interplay between the microstructural evolution and the mechanical behaviour of the steels. The understanding of the physics behind the observed material behaviour is necessary to enable the selection of the optimal material. Furthermore, nowadays FEM simulations are widely used by the automotive industry to predict the material behaviour during forming operations and car crash. A better understanding of the physical material behaviour is necessary to develop better material models for simulations.

The objective of this thesis was twofold: 1) to study the effect of the various factors, including the chemical composition, strain rate and temperature, on the mechanical properties and the strain-induced α'-martensite transformation and 2) to understand the influence of the α'-martensite transformation on the mechanical properties of metastable austenitic stainless steels. This thesis concentrated only on the physical metallurgy of the austenitic stainless steels. The relation between the material behaviour and crash performance of the stainless steel parts has been discussed elsewhere (Talonen and Hänninen, 2006). Although the present thesis is a monograph, part of the results has already been published (Talonen *et al.*, 2004; 2005; 2006).

3 EXPERIMENTAL PROCEDURES

Three metastable austenitic stainless steel compositions were chosen for the experiments. Mechanical testing was carried out by means of uniaxial tensile tests in the rolling direction at different strain rates and deformation temperatures. The deformation microstructures were examined using various experimental techniques. X-ray diffraction and magnetic measurements were used for phase identification. XRD line broadening analysis was used to measure the dislocation densities of the austenite and α'-martensite phases and the intrinsic stacking fault energies of the test materials. The load distribution between the austenite and α'-martensite phases was studied by *in-situ* XRD stress measurements carried out during uniaxial tensile tests. The formation of shear bands in the austenite phase was examined by using scanning and transmission electron microscopy. Optical metallography and coupled quantitative image analysis was utilised to study the morphology of the strain-induced α'-martensite phase and its effect on work hardening.

3.1 Test materials

The test materials used in this study were austenitic stainless steel grades EN 1.4301 (AISI 304) and EN 1.4318 (AISI 301LN). One heat of EN 1.4301 steel and two heats of EN 1.4318 steel, designated as the EN 1.4318-1 and the EN 1.4318-2, were used in the experiments. The chemical compositions of the test materials are given in Table 2. Test materials EN 1.4301 and EN 1.4318-1 were received as 1 mm and EN 1.4318-2 as 1.5 mm thick sheets in 2B delivery condition (SFS-EN 10088-2, 1995). The grain sizes determined according to the standard ASTM E 112-96 (1997) and the M_{d30} temperatures calculated according to Nohara *et al.* (1977) (equation 17) are given in Table 3. The EN 1.4318 steel grades had low nickel and high nitrogen content, and exhibited higher M_{d30} temperatures and lower austenite stability than the EN 1.4301 steel. Therefore, the EN 1.4301 steel is later referred to as the stable grade and the EN 1.4318 steels as the unstable grades.

Table 2 Chemical compositions of the test materials in weight percents

Steel grade	C	Si	Mn	Cr	Ni	Mo	Cu	N	Fe
EN 1.4301	0.041	0.33	1.71	18.2	8.1	0.32	0.37	0.054	bal.
EN 1.4318-1	0.019	0.48	1.61	17.6	6.6	0.14	0.22	0.094	bal.
EN 1.4318-2	0.017	0.51	1.34	17.4	6.6	0.15	0.14	0.145	bal.

Table 3 Grain sizes and M_{d30} temperatures (Nohara *et al.*, 1977) of the test materials

Steel grade	Mean intercept length (μm)	ASTM Grain size number	M_{d30} temperature (°C)
EN 1.4301	5.9	11.4	-16
EN 1.4318-1	11.6	9.5	37
EN 1.4318-2	14.8	8.9	23

3.2 Tensile tests

Mechanical testing of the test materials was carried out by means of uniaxial tensile tests. The objectives of the tensile tests were to study the effect of chemical composition, strain rate and deformation temperature on the mechanical response. The

effect of the strain rate was studied on the EN 1.4301 and EN 1.4318-1 steels, and the effect of the deformation temperature on the EN 1.4318-2 steel. All tensile testing was carried out in the rolling direction.

3.2.1 Tensile testing at various strain rates

The tensile tests were carried out on the EN 1.4318-1 and EN 1.4301 steels at the nominal strain rates of 3×10^{-4}, 10^{-1} and 200 s^{-1} at room temperature in air. The tests at the strain rates of 3×10^{-4} and 10^{-1} s^{-1} were performed with a servohydraulic MTS 810 tensile testing machine. The tests at strain rate 200 s^{-1} were performed with a hydraulic high speed tensile testing machine at Delft Technical University. A more detailed description of the test procedures and test samples has been given in (Talonen *et al.*, 2005).

The adiabatic heating during the high-speed deformation was monitored by means of temperature measurements at the strain rate of 10^{-1} s^{-1}. This was considered to be high enough to cause practically adiabatic condition, since the duration of the tests at this strain rate was only a few seconds. Three thermocouples were welded on the gauge section of the tensile test samples. The temperature data was recorded with a National Instruments SCB-68 data logger. The rate of data acquisition was 100 data points per second.

3.2.2 Tensile testing at various temperatures

The effect of deformation temperature on the mechanical response and the microstructural evolution of the EN 1.4318-2 steel was studied by performing tensile tests at the constant temperatures of -40, 0, +24, +40 and +80°C. The tests were conducted at the Outokumpu Stainless Research Laboratory in Tornio at the strain rate of 3×10^{-4} s^{-1}. The equipment consisted of a Zwick Z250 tensile testing machine, a SFL EC1639 environmental chamber and a Maytec PMA-12/V7 extensometer. The tests were carried out on machined samples with 50 mm gauge length. All testing was performed in a gas (air or nitrogen) atmosphere.

3.3 Ferritescope measurements

A Ferritescope (Helmut Fischer GmbH, model MP3C) was used for the quantification of the ferromagnetic α'-martensite phase. The device was calibrated with δ-ferrite standard samples and the results were converted to the α'-martensite contents with the correlation factor of 1.7 (Talonen *et al.*, 2004). The effect of sheet thickness on the results was compensated by means of a correction curve provided by the manufacturer of the device. Before the Ferritescope measurements the surfaces of the samples were electropolished with Struers Lectropol-5 equipment by using A2 electrolyte (78 ml perchloric acid, 120 ml distilled water, 700 ml ethanol and 100 ml butyl cellosolve) at 34 V for 30 s.

3.4 X-ray diffraction measurements

The microstructures of the test materials were analysed by means of X-ray diffraction. The X-ray diffraction experiments had three objectives: 1) to identify the phases in the deformed samples, 2) to carry out X-ray diffraction line broadening analysis in order to analyse the distribution of plastic deformation between the different phases and 3) to determine the stacking fault energies of the test materials.

The equipment used in the XRD analysis consisted of a Siemens Kristalloflex 710H high voltage generator, a CoKα X-ray tube, an Inel flat monochromator (Ge crystal), an Inel CPS 120 position sensitive detector and an Inel MPG goniometer. The use of the crystal monochromator enabled the complete elimination of the Kα_2 and Kβ radiation components. In order to obtain better counting statistics and to reduce the effects of texture, the samples were rotated around the surface normal (ϕ angle) during the measurements. The angle at which the X-ray beam entered the sample surface (Ω angle) had a constant value of 10°.

Samples with the dimensions of 10×10 mm^2 used in the line broadening analysis and for phase identification were cut from the strained tensile test samples with an abrasive cutting machine. The surfaces of the samples were ground with SiC emery papers up to roughness of 2500 and electropolished with A2 electrolyte at 34 V for 30 s.

The SFE measurements were carried out on powder specimens, since the measurement of stacking fault probability is sensitive to the presence of long range residual stresses. The powders were machine ground with an emery paper tool and compacted with silicon paste. The average particle size of the powders was determined by a microscope to be less than 50 μm.

3.5 X-ray diffraction line broadening analysis

Plastic deformation causes broadening of the X-ray diffraction lines. According to its origin, the broadening is divided in size and strain broadening. The size broadening is caused by the crystal defects that split the perfect crystal to small coherently diffracting domains. These defects involve not only the grain boundaries, but also the stacking and twin faults, dislocation substructures (*e.g.*, cell boundaries) and even single dislocations. The strain broadening is caused by the lattice distortions due to the presence of crystal defects, including dislocations and point defects. In the case of plastically deformed polycrystalline material with a regular grain size (order of microns), the presence of the dislocations is clearly the most important origin of both size and strain broadening. Therefore, the XRD line broadening analysis can be utilised in estimating the dislocation densities of the crystalline materials.

The most widely used measure of the XRD line broadening is the integral breadth, defined as the ratio of the integrated intensity and the height of the XRD line profile. Sometimes the full width at the half maximum (FWHM) is used instead.

3.5.1 Size and strain broadening

The influence of small coherent domain size on XRD line broadening was first found by Scherrer, who derived the following expression, known as Scherrer's equation, for the volume-weighted coherent domain size ⟨D⟩ (Klug and Alexander, 1974):

$$\langle D \rangle = \frac{K\lambda}{\beta_S \cos\theta}, \tag{19}$$

where K is constant (close to unity), λ is wavelength and β_S is integral breadth due to the size broadening in radians in the 2θ scale. The relation between the strain broadening β_D in radians and the microstrain is given by (Klug and Alexander, 1974):

$$e = \frac{\beta_D}{4\tan\theta}, \tag{20}$$

where e is maximum upper limit of lattice distortions. The definition of e is vague, since it does not involve information about the distribution of strain. A better measure of the microstrain is the root mean square microstrain (RMSS), which for the Gaussian strain distribution is (Balzar, 1999):

$$\langle \varepsilon^2 \rangle^{1/2} = \left(\frac{2}{\pi}\right)^{1/2} e. \tag{21}$$

A physical XRD line profile is a convolution of the components β_S and β_D. Therefore, if one wants to determine the values of ⟨D⟩ and $\langle \varepsilon^2 \rangle^{1/2}$, the broadening components β_S and β_D need to be separated. In general, the separation can be performed in two alternative ways either by using 1) the Warren-Averbach method or 2) the integral breadth method.

The Warren-Averbach method (Warren and Averbach, 1950; 1952; Warren, 1990) involves the expression of the XRD line profile in terms of Fourier coefficients, from which the domain size and microstrain distributions can be derived. In the integral breadth methods, the line shape is described by the integral breadth (or in some instances by the FWHM). They are divided in single-line methods (de Keijser *et al.*, 1982), Voigt multiple-line integral breadth methods (Langford, 1978; Balzar and Ledbetter, 1993; Balzar, 1999) and simplified integral breadth methods (Klug and Alexander, 1974). Although the simplified integral breadth methods have been shown to involve serious limitations due to the assumptions made concerning the shapes of the line profiles (Langford, 1980; Balzar, 1992; Balzar and Popović, 1996; Balzar *et al.*, 2004), they have been rather widely applied in experimental studies (*e.g.*, Narutani, 1989; Hoffmann *et al.*, 1997; Hoffmann *et al.*, 2001; Pešička *et al.*, 2003).

The separation of the size and strain broadening components is based on the fact that the size broadening is independent and the strain broadening is dependent on the reflection order. Therefore, by analysing at least two orders of reflections the separation can be realised. An exception is made by the single line methods that, however, due to their limited accuracy should be used only when a single reflection is available.

In this study, two approaches, the simplified integral breadth method and the Voigt multiple-line integral-breadth method were utilised. For brevity, these are later referred

to as the integral breadth method (IBM) and the Voigt method (VM). With the equipment used, two orders of reflections were available from both the austenite and α'-martensite phases. No analysis was carried out on the ε-martensite phase due to its low volume fraction.

3.5.2 Integral breadth method (IBM)

Before further analysis, the instrumental contribution has to be removed from the measured XRD line profiles. In the case of the integral breadth method, the instrumental broadening was subtracted from the experimental data by assuming that the line shapes are Gaussian. In that case, the integral breadth of the pure line profile β is (Klug and Alexander, 1974):

$$\beta = \sqrt{\beta_E{}^2 - \beta_I{}^2}\,, \tag{22}$$

where β_E is the integral breadth of the measured diffraction line profile and β_I is the integral breadth measured from a strain-free reference sample. An annealed austenitic stainless steel sample was used as a reference, since it was found to show even narrower line profiles than the standard silicon powder NIST SRM 640c.

The integral breadth method necessitates the assumption that the size and strain broadening components obey some specific distribution. This is the most important limitation of the technique, and may cause systematic error in the values of ⟨D⟩ and e. However, it has been shown that the strain broadening can be approximated with a Gaussian function and the size broadening with a Lorentzian function (Klug and Alexander, 1974). The integral breadth of the convolution of a Gaussian function of breadth β_G and a Lorentzian function of breadth β_L is given by (Ruland, 1965; Schoening, 1965):

$$\beta = \beta_G \frac{\exp\left[-(\beta_L/\beta_G)^2/\pi\right]}{1 - 2\mathrm{erf}\left[\sqrt{2/\pi}(\beta_L/\beta_G)\right]}, \tag{23}$$

where erf(x) is the error function, defined as:

$$\mathrm{erf}(x) = \frac{1}{\sqrt{2\pi}} \int_0^x \exp\left(\frac{-t^2}{2}\right) dt\,. \tag{24}$$

Rather complicated equation can be approximated with the following expression determined by Halder and Wagner (1966):

$$\frac{\beta_L}{\beta} = 1 - \left(\frac{\beta_G}{\beta}\right)^2. \tag{25}$$

By assuming that $\beta_L=\beta_S$ and $\beta_G=\beta_D$, combining the equations 19, 20 and 25 leads to:

$$\frac{K\lambda}{\beta\cos\theta\langle D\rangle} = 1 - \left(\frac{16e^2\tan^2\theta}{\beta^2}\right), \tag{26}$$

which can be rearranged as (Klug and Alexander, 1974):

$$\frac{\beta^2}{\tan^2\theta} = \frac{K\lambda}{\langle D\rangle}\left(\frac{\beta}{\tan\theta\sin\theta}\right) + 16e^2 . \quad (27)$$

If at least two orders of reflections are available, ⟨D⟩ and e can be solved from the slope and y-intercept of the $\beta^2/\tan^2\theta$ vs. $\beta/\tan\theta\sin\theta$ plot. Austenite 111 and 222 and α'-martensite 110 and 220 reflections were used in the present analysis. The shapes of the line profiles were modelled with the Voigt function by using the Microcal Origin software.

3.5.3 Voigt method (VM)

In the integral breadth method, systematic errors may arise due to the assumptions made about the distributions of the size and strain broadening components. The classical way to avoid any bias due to the assumptions is to use the Stokes (1948) deconvolution method to apply the instrumental correction, and the Warren-Averbach approach (Warren and Averbach, 1950; 1952; Warren, 1990) for the separation of the size and strain broadening components. However, both of these methods require high quality data and are severely affected by the overlapping of the diffraction lines (as the austenite 111 and α'-martensite 110 lines in the present case). Recently, an alternative but equivalent method based on the Voigt-function modelling has been developed (Balzar, 1992; Balzar and Ledbetter, 1993), referred to as the Voigt multiple-line integral-breadth method. Furthermore, a PC program BREADTH (Balzar, 2006) utilising the method is available, which was used in the present study. The program uses the Gaussian and Lorentzian broadening components of the Voigt function of two or more reflections as the input data, generates the size and strain Fourier coefficients and calculates the surface- and volume-weighted domain sizes and the root mean square microstrain.

Before the data analysis with the BREADTH, the experimental Lorentzian and Gaussian components wG_E and wL_E were determined by means of least square fitting with Microcal Origin software. To obtain the pure broadening components wG and wL, the instrumental correction was made separately for both components by using the following formulas (Balzar, 1999):

$$wG = \sqrt{wG_E{}^2 - wG_I{}^2} \quad (28)$$

$$wL = wL_E - wL_I , \quad (29)$$

where wG_I and wL_I are the Gaussian and Lorentzian components of the instrumental broadening, respectively.

3.5.4 Calculation of dislocation density

The presence of the dislocations contributes to both size and strain broadening. Therefore, the dislocation density can, in principle, be estimated based on the microstrain or domain size alone. However, accurate quantification of the dislocation density is difficult, since numerous simplifications have to be made concerning the

dislocation arrangement, interaction between the dislocations, texture and elastic anisotropy. Therefore, several approaches leading to different quantitative results have been suggested in literature. It is also noteworthy that in all the following calculations any other sources of broadening beyond the dislocations are not taken into account. Although the influence of the dislocation arrangement on the XRD line broadening has been discussed in literature (*e.g.*, Wilkens, 1970; 1979; Wang *et al.*, 1982), in the present study these effects were not considered. Instead, a rather simple approach presented in the following was used.

Gay *et al.* (1953) defined the relationship between the domain size and the dislocation density by assuming that the dislocations split the lattice into domains so that each domain is defined by a single dislocation. Consequently, the dislocation density is given by:

$$\rho_D = \frac{1}{\langle D \rangle^2}. \tag{30}$$

Williamson and Smallman (1956) suggested that the dislocations split the lattice into blocks with the size ⟨D⟩. If each surface of the (cubic) block contains N dislocations, the dislocation density is given by:

$$\rho_D = \frac{3N}{\langle D \rangle^2}. \tag{31}$$

For a uniform dislocation distribution N=1, and for dislocation cell structures and tilt boundaries N>1. Consequently, Williamson's and Smallman's model predicts at least three times higher dislocation density compared to Gay's model. These simple models have been criticised. For instance, Ungár *et al.* (2001) claimed that a single dislocation cannot destroy the coherence of the scattering, and the coherent domain size does not correspond to the average distance between the dislocations. Furthermore, the estimation of the dislocation density from the domain size of FCC metals is made more difficult by the presence of stacking faults. As they split the crystal to domains similarly as the dislocations, they also contribute to the size broadening and affect the value of ⟨D⟩. Warren (1990) suggested that the domain size ⟨D⟩ measured from 111 and 222 reflections is affected by the stacking and twin faults according to the following expression:

$$\frac{1}{\langle D \rangle} = \frac{1}{\langle D \rangle_{true}} + \frac{(1.5\alpha + \beta_T)}{a}\frac{\sqrt{3}}{2}, \tag{32}$$

where $\langle D \rangle_{true}$ is the true domain size, α is the stacking fault probability and β_T is the twin fault probability. Unfortunately, in the present study it was not possible to determine the faulting term $(1.5\alpha+\beta_T)$, since it would have required the determination of ⟨D⟩ from at least two sets of multiple-order hkl-reflections. With the equipment used in the present study only the austenite 111 and 222 reflections could be detected. Furthermore, due to the bulk samples possessing residual stresses, not even the accurate determination of α was possible. Therefore, the effects of faulting on ⟨D⟩ were neglected.

The dislocation density can be calculated also from the microstrain. If it is assumed that the microstrain originates only from the dislocations present in the crystal, the dislocation density is obtained by dividing the total strain energy of the crystal lattice E_{tot} by the self-energy of a dislocation line per unit length E_d (Williamson and Smallman, 1956):

$$\rho_S = \frac{E_{tot}}{E_d}. \tag{33}$$

The total strain energy E_{tot} is obtained from the microstrain as follows (Williamson and Smallman, 1956):

$$E_{tot} = \frac{3E\langle\varepsilon^2\rangle}{2}, \tag{34}$$

where E is Young's modulus and $\langle\varepsilon^2\rangle$ is the mean square microstrain. The self-energy of a dislocation per unit length is given by:

$$E_d = F\frac{Gb^2}{4\pi\mu}\ln\left(\frac{r}{r_0}\right), \tag{35}$$

where G is the shear modulus, b is the Burgers vector, μ is a constant characteristic of the dislocation type ($1-\nu$ for an edge dislocation and 1 for a screw dislocation), r_0 is the radius of the dislocation core and r is the distance between adjacent dislocations. F is a factor that describes the variation of the dislocation energy from the average value due to interaction with other dislocations. By combining equations 33-35 and by assuming that $E=2G(1+\nu)=(13/5)G$, the following formula for the dislocation density is obtained:

$$\rho_S = \frac{78\left\langle\varepsilon^2\right\rangle\pi\mu}{5Fb^2\ln\left(\frac{r}{r_0}\right)}. \tag{36}$$

The dislocation density may be estimated also by combining ρ_D and ρ_S. Williamson and Smallman (1956) defined the dislocation density as the geometric mean of ρ_D and ρ_S:

$$\rho = \sqrt{\rho_D\rho_S}, \tag{37}$$

which by the substitution of equations 30 and 36 results in:

$$\rho = \sqrt{\rho_D\rho_S} = \frac{\left\langle\varepsilon^2\right\rangle^{1/2}}{\langle D\rangle b}\sqrt{\frac{78\pi\mu}{5\ln\left(\frac{r}{r_0}\right)}}. \tag{38}$$

In the present analysis, equation 38 was used to calculate the dislocation densities. The factor μ describing the dislocation type was assumed to lie between the extreme values corresponding to the edge and screw dislocations, *i.e.*, 0.85. Since the tested steels

exhibited low SFE, the calculations on the austenite phase were carried out assuming that all dislocations are extended dislocations consisting of two Shockley partial dislocations with b_p=0.147 nm. The effect of the presence of stacking faults on the size broadening was neglected due to the limitations of the equipment described above. For the α'-martensite phase b=0.25 nm was used. The radius of the dislocation core was assumed to be 1 nm and the distance between adjacent dislocations a half of the domain size. With these input data, equation 38 becomes almost equivalent with the formula suggested by Mikkola and Cohen (1965):

$$\rho = \frac{2\sqrt{3}\left\langle \varepsilon^2 \right\rangle^{1/2}}{\langle D \rangle b}. \tag{39}$$

3.6 Stacking fault energy measurements

Since no compositional equations for SFE taking into account the nitrogen content are available, the XRD was used to measure the stacking fault energy of the studied steels. The XRD measurement of the SFE is based on the measurement of the dislocation density by means of the XRD line broadening analysis and the measurement of the stacking fault probability from the diffraction line displacements. The theoretical background of the technique was thoroughly reviewed by Reed and Schramm (1974), and the technique was applied to determine the classical compositional equation of SFE for austenitic steels (Schramm and Reed, 1975).

The use of the position sensitive detector enabled the collection of the necessary data for both SFP and line broadening analysis simultaneously. The XRD exposure of about 24 h was repeated 5 times for each test material. All measurements were carried out at room temperature.

3.6.1 Stacking fault probability

The stacking fault probability (SFP), *i.e.*, the probability that a stacking fault occurs on an {111} plane of the austenite phase can be determined from the displacements of austenite reflections (Paterson, 1952; Warren, 1990). The displacement of a diffraction line in the 2θ scale due to the faulting is given by (Warren, 1990):

$$\Delta(2\theta)^\circ = \frac{90\sqrt{3}\alpha \tan\theta}{\pi^2 h_0^2 (u+b)} \sum_b (\pm) L_0 , \tag{40}$$

where α is the stacking fault probability and $\Sigma_b(\pm)L_0/h_0^2(u+b)$ is a constant specific to each hkl reflection. The values of $\Sigma_b(\pm)L_0/h_0^2(u+b)$ for austenite 111, 200, 220, 311 and 222 reflections are given in Table 4.

Table 4 Constants $\Sigma_b(\pm)L_0/h_0^2(u+b)$ for austenite 111, 200, 220, 311 and 222 reflections (Warren, 1990)

hkl	$\Sigma_b(\pm)L_0/h_0^2(u+b)$
111	1/4
200	-1/2
220	1/4
311	-1/11
222	-1/8

To avoid errors due to incorrect positioning of the sample in the diffractometer, the SFP is commonly determined by measuring the distance between two adjacent austenite reflections. From Table 4 it can be seen that the constant $\Sigma_b(\pm)L_0/h_0^2(u+b)$ has a positive value for 111 and 220 reflections and a negative value for the other reflections. Therefore, by measuring the distance between, for instance, 111 and 200 reflections from both cold-worked and annealed samples the SFP can be calculated as follows (Warren, 1990):

$$\alpha = \frac{\Delta(2\theta_{200} - 2\theta_{111})_{CW} - \Delta(2\theta_{200} - 2\theta_{111})_{ANN}}{-90\sqrt{3}\left(\frac{\tan\theta_{200}}{2} + \frac{\tan\theta_{111}}{4}\right)}\pi^2 , \tag{41}$$

where $\Delta(2\theta_{200}\text{-}2\theta_{111})_{CW}$ and $\Delta(2\theta_{200}\text{-}2\theta_{111})_{ANN}$ are the distances between 200 and 111 reflections in cold-worked and annealed samples, respectively. However, in this study the need of an annealed and stacking fault free sample was avoided by a novel procedure described in the following. In the case of a powder specimen free of any long range residual stresses, the line positions are assumed to be affected only by the lattice spacing according to Bragg's law and by the stacking faults according to equation 40. Therefore, by combining Bragg's law and equation 40, the following formula with two unknown parameters (interplanar spacing d and stacking fault probability α) is obtained:

$$2\theta = 2\arcsin\left(\frac{\lambda}{2d}\right) + \frac{90\sqrt{3}\alpha\tan\theta}{\pi^2 h_0^2 (u+b)}\sum_b (\pm)L_0 . \tag{42}$$

With the XRD equipment used, five austenite reflections were measured simultaneously. Therefore, a set of five equations was obtained from each measurement, and the two unknowns (SFP α and lattice spacing d) could be solved by regression analysis.

3.6.2 Determination of stacking fault energy

In the equilibrium condition the relation between the SFE and the separation distance between the partial dislocations w, *i.e.*, the width of a stacking fault is determined by the balance between the energy bound to the fault and the repulsive force between the partial dislocations (equations 5 and 6). Since in the FCC lattice a stacking fault is formed by the dissociation of a single perfect dislocation, there is a direct relationship between the stacking fault probability and the dislocation density (Smallman and Westmacott, 1957):

$$\alpha = \rho w d_{111} = \rho w \frac{a}{\sqrt{3}}, \tag{43}$$

where d_{111} is the spacing between {111} planes and a is the lattice parameter. Reed and Schramm (1974) used the mean square microstrain averaged over 50 Å $\langle \varepsilon_{50}^2 \rangle$ to calculate the dislocation density. By combining equations 5, 36 and 43, and by considering the possible uncertainties due to dislocation type, elastic anisotropy and interaction between the dislocations, Reed and Schramm obtained the following equation for the SFE:

$$\gamma = \frac{K_{111}\omega_0 G a A^{-0.37}}{\pi\sqrt{3}} \frac{\left\langle \varepsilon_{50}^{\ 2} \right\rangle}{\alpha}, \tag{44}$$

where K_{111} and ω_0 are constants that depend on the dislocation configuration and A is the elastic anisotropy factor (Zener anisotropy). Although it has been questioned whether ω_0 has a constant value with varying strain (Teng *et al.*, 1992), in this study the constant ω_0 determined by Schramm and Reed (1975) was used, resulting in the following formula:

$$\gamma = 17800 \frac{\left\langle \varepsilon_{50}^{\ 2} \right\rangle}{\alpha} (\mathrm{mJ/m^2}). \tag{45}$$

The mean square microstrains $\langle \varepsilon_{50}^2 \rangle$ were determined by the Voigt method described in section 3.5.3.

3.7 *In-situ* XRD stress measurements during tensile straining

The load partitioning between the austenite and α'-martensite phases during the tensile deformation of the unstable EN 1.4318-1 steel was analysed by means of *in-situ* X-ray diffraction stress measurements. Tensile test samples, shown in Figure 9, were plastically strained at strain increments of about 0.02. Straining was carried out by hand with a specially designed screw vice. Therefore, accurate control of the strain rate was not possible. However, the strain rate was kept as close to 3×10^{-4} s^{-1} as possible. After each strain increment, the XRD stress measurement was carried out on the gauge section of the sample (Figure 9, location A) with Stresstech X3000 stress measurement equipment by using the $\sin^2\psi$ method (Noyan and Cohen, 1987). Austenite 311 and α'-martensite 211 reflections and MnKα radiation were used. The X-ray beam was collimated with a ∅3 mm collimator. Before the XRD measurements, the surfaces of the gauge sections of the samples were electropolished.

Since the XRD equipment enabled the measurement of only one reflection at a time, separate specimens were used for the stress measurements on the austenite and α'-martensite phases. The macroscopic stress level was measured with two strain gauges attached to both sides of the sample at the location B (Figure 9). The α'-martensite volume fraction was measured after each strain increment with the Ferritescope. Since the Ferritescope measurements were carried out on the samples under a tensile stress, the effect of the stress on the Ferritescope readings (the Villari effect) was compensated

with an empirical correction curve determined by comparing the Ferritescope readings from stressed and unstressed samples.

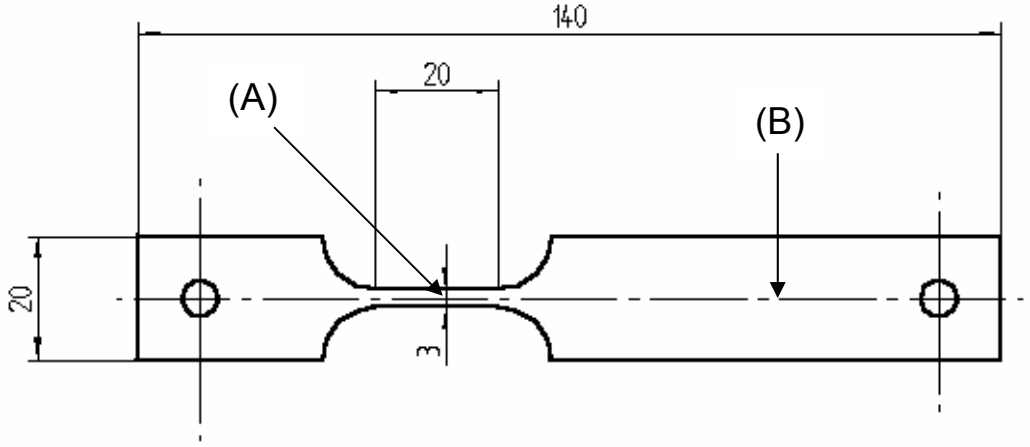

Figure 9 Tensile test sample used in *in-situ* XRD stress measurements. (A) indicates location of XRD stress measurement and (B) location of strain gauges

The XRD stress analysis is based on the measurement of lattice spacing $d_{\psi\phi}$ at several ψ angles. The sample and laboratory coordinate systems and angles ψ and ϕ are illustrated in Figure 10.

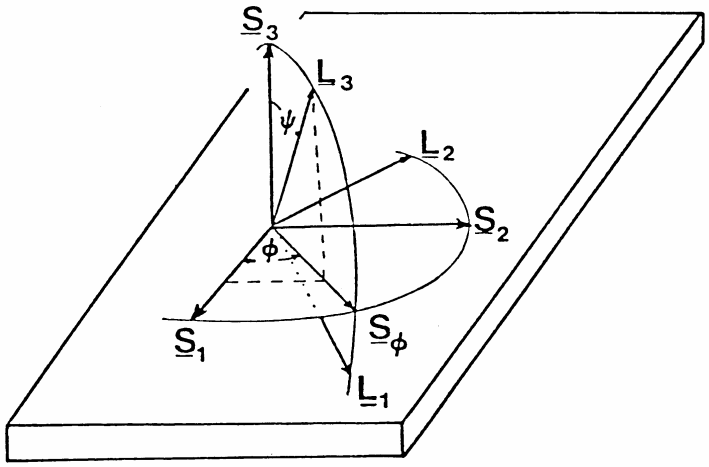

Figure 10 Definition of coordinate systems $\underline{L}_i$ and $\underline{S}_i$ and angles ψ and ϕ in XRD stress measurement (Noyan and Cohen, 1987)

The orientation of the sample is defined by the axes $\underline{S}_i$. Coordinates $\underline{L}_i$ define the laboratory coordinate system. Axis $\underline{L}_3$ is normal to the atom planes whose lattice spacing is measured with XRD. Based on the lattice spacing measurements, the elastic strains can be calculated by using the following equation (Noyan and Cohen, 1987):

$$\left(\varepsilon'_{33}\right)_{\phi\psi} = \frac{d_{\phi\psi} - d_0}{d_0} = \varepsilon_{11}\cos^2\phi\sin^2\phi + \varepsilon_{12}\sin 2\phi\sin^2\psi + \varepsilon_{22}\sin^2\phi\sin^2\psi + \varepsilon_{33}\cos^2\psi + \varepsilon_{13}\cos\phi\sin 2\psi + \varepsilon_{23}\sin\phi\sin 2\psi, \quad (46)$$

where d_0 is unstressed lattice spacing. If the elastic strain ε_{11} in direction $\underline{S}_1$ is to be measured, and ε_{12}, ε_{13}, ε_{23} and ε_{33} are assumed to be zero, equation 46 reduces to:

$$\frac{d_{\phi\psi} - d_0}{d_0} = \varepsilon_{11} \sin^2 \phi \,. \tag{47}$$

Consequently, in the absence of the shear stress components the $d_{\psi\phi}$ vs. $\sin^2\psi$ plot is linear, and the elastic strain ε_{11} is obtained from its slope. The elastic strain ε_{33} in the $\underline{S}_3$ direction is often assumed to be zero due to the small penetration depth of the X-rays. In this condition, the lattice spacing measured at ψ=0 can be used as the stress-free lattice spacing d_0.

In the conditions described above, the stress in the $\underline{S}_1$ direction is obtained from the lattice strain ε_{11} as follows (Noyan and Cohen, 1987):

$$\sigma_{11} = \frac{E}{1+\nu} \varepsilon_{11} \,, \tag{48}$$

where the term $E/(1+\nu)$ is referred to as the X-ray elastic constant. Its accurate determination in the present case was problematic due to the texture evolution during the plastic deformation, and due to the multiphase nature of the test material. For simplicity, the following values suggested by the measurement software for FCC and BCC iron based alloys were used: FCC E=196 GPa and ν=0.28 and BCC E=211 GPa and ν=0.30.

3.8 Scanning electron microscopy

Deformation microstructures of the tensile strained test materials were examined with a Zeiss Ultra 55 field emission gun scanning electron microscope (FEG-SEM). By using the electron channelling contrast imaging (ECCI) (Joy *et al.*, 1982; Wilkinson and Hirsch, 1997; Simkin and Crimp, 1999) technique, it was possible to visualise the microstructural features, including dislocation sub-structures, shear bands and martensite phases resulting from the plastic deformation. An acceleration voltage of 10 kV and a working distance of 3 mm were used. The SEM examination was performed on the surfaces of the tensile strained test samples. Before the examination, the surfaces were electropolished with A2 electrolyte at 34 V for 60 s.

3.9 Transmission electron microscopy

The deformation microstructures of the EN 1.4318-1 steel tensile strained at the strain rates of 3×10^{-4} and 200 s^{-1} were examined by transmission electron microscopy (TEM). The TEM examination was carried out by VTT (Technical Research Centre of Finland) with a Phillips CM200 field emission gun scanning transmission electron microscope (FEG-STEM). The specimens were first mechanically thinned to 80 μm and subsequently electropolished with twin-jet equipment at 17 V at room temperature. The electrolyte used contained 90% acetic acid and 10% perchloric acid.

3.10 Optical metallography

The morphology of the strain-induced α'-martensite phase formed in the EN 1.4318-1 steel at the strain rate of 3×10^{-4} s^{-1} was studied by means of optical metallography. The experiments had two objectives. Firstly, the average particle size of the α'-martensite was determined in order to study the dispersion hardening effect caused by the strain-induced α'-martensite transformation. Secondly, the percolation of the α'-martensite phase, *i.e.*, the formation of infinite clusters of α'-martensite phase was examined in order to find the percolation threshold value of $f^{\alpha'}$. A classical example of the percolation is the behaviour of a mixture of insulating and conducting components. The mixture becomes conductive when the volume fraction of the conducting component exceeds the percolation threshold. Analogously, it was presumed that when the α'-martensite volume fraction exceeds the percolation threshold, the influence of the α'-martensite phase on the mechanical response of the aggregate is abruptly changed.

Cross-sectional samples were cut from the tensile test samples parallel and transverse to the tensile axis with an abrasive cutting machine. The samples were mounted in resin and ground with SiC emery papers with roughnesses of 80, 180, 320, 800, 1200 and 2500. The ground samples were electropolished with A2 electrolyte at 20 V for 30 s. Two different etchants were used. Electrolytical etching with a mixture of 60 ml nitric acid and 40 ml distilled water was used to reveal the austenite grain boundaries. The etching was carried out at 1.0 V and the etching time was about 8 min. To reveal the α'-martensite phase a mixture of two solutions was used: 0.15 g sodium-metabisulfite in 100 ml distilled water and 10 ml hydrochloric acid in 100 ml distilled water. In order to colour the α'-martensite phase dark enough for the image analysis, the etching time was varied between 2 and 5 min depending on the α'-martensite volume fraction.

The samples were examined with Nikon Epiphot 200 optical microscope. Five digital micrographs of 2560×1920 pixels were taken from each sample at arbitrary locations. The magnification was such that the size of one pixel equalled 0.056 μm. Therefore, each micrograph covered an area of about 143×107 μm^2. The micrographs were converted to binary bitmaps with Paint Shop Pro image processing software. Due to inadequate contrast between the finely dispersed austenite and α'-martensite phases, the conversion from greyscale to binary images involved the appearance of single pixels, especially at the austenite-α'-martensite interfaces. Since these false indications would have affected the determination of the particle and cluster sizes, they were removed before further analysis.

The particle size of the α'-martensite phase was determined by means of chord length measurements. The average chord lengths and the chord length distributions were determined with a MATLAB routine programmed specifically for this purpose. The routine determined also the α'-martensite volume fractions. Another MATLAB routine, based on the Hoshen and Kopelman algorithm (Hoshen and Kopelman, 1976), was used to analyse the clustering and percolation of the α'-martensite phase. It determined the number and average size of the α'-martensite clusters, the size of the largest cluster, and specified whether the α'-martensite phase formed an infinite percolating cluster.

4 RESULTS

4.1 Tensile tests

4.1.1 Effect of strain rate on tensile behaviour

The effect of strain rate on the true stress-strain curves of the EN 1.4318-1 and EN 1.4301 steels is illustrated in Figures 11 and 12, respectively. The yield strength of both materials increased with increasing strain rate, indicating clear positive strain rate sensitivity. The unstable and stable steels showed different work-hardening behaviours, which is best illustrated by comparing the work-hardening rates (WHR) (=first derivatives of the stress-strain curves) of the steels, presented with the thick lines in Figures 13 and 14. The thin lines in Figures 13 and 14 are the corresponding true stress-strain curves, and the intersections of the true stress-strain and WHR curves represent the onset of plastic instability according to Considére's criterion. A distinct difference between the two steels was found. The EN 1.4301 steel exhibited continuously decreasing WHR, typical of single-phase metals and alloys. Instead, the EN 1.4318-1 steel showed similar work-hardening abnormality as reported in previous investigations on metastable steel grades (Huang *et al.*, 1989; Fang and Dahl, 1991; De *et al.*, 2006). The behaviour was characterised by well defined minimum and maximum in the WHR curve plotted as a function of strain. When the strain rate increased, the maximum became lower and was shifted to a higher strain level.

The variation of the work-hardening rate with the varying strain rate affected the uniform elongation of the steels. With the unstable EN 1.4318-1 steel the shift of the work-hardening rate maximum to a higher strain with increasing strain rate slightly increased the uniform elongation. A reverse effect was observed with the stable EN 1.4301 steel. When the strain rate increased, a significant decrease in the uniform elongation occurred. From Figure 14 it may be observed that this was attributed to the rapidly decreasing WHR at the high strain rates.

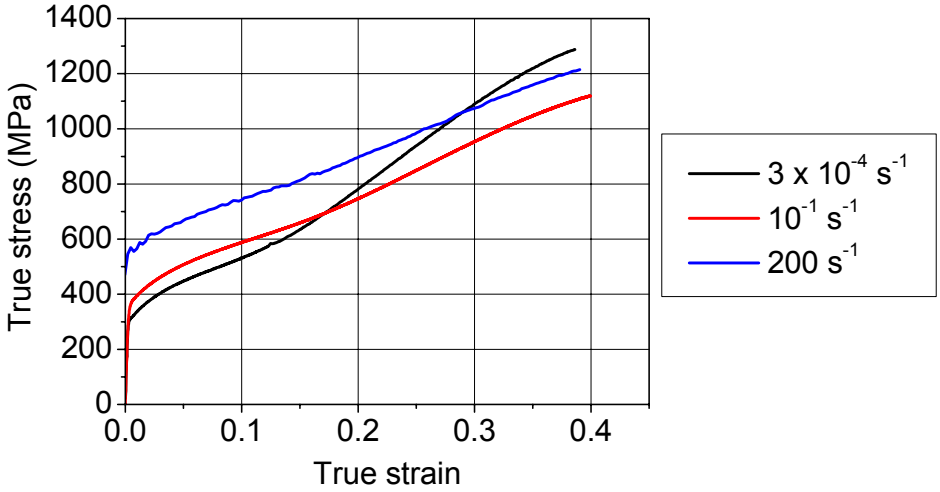

Figure 11 True stress-strain curves of EN 1.4318-1 steel at strain rates 3×10^{-4}, 10^{-1} and 200 s^{-1} at room temperature

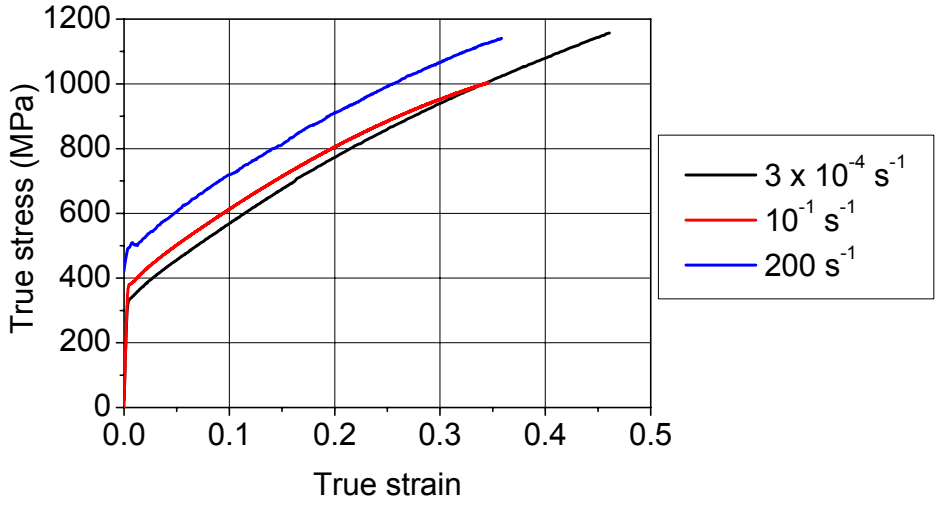

Figure 12 True stress-strain curves of EN 1.4301 steel at strain rates 3×10^{-4}, 10^{-1} and 200 s^{-1} at room temperature

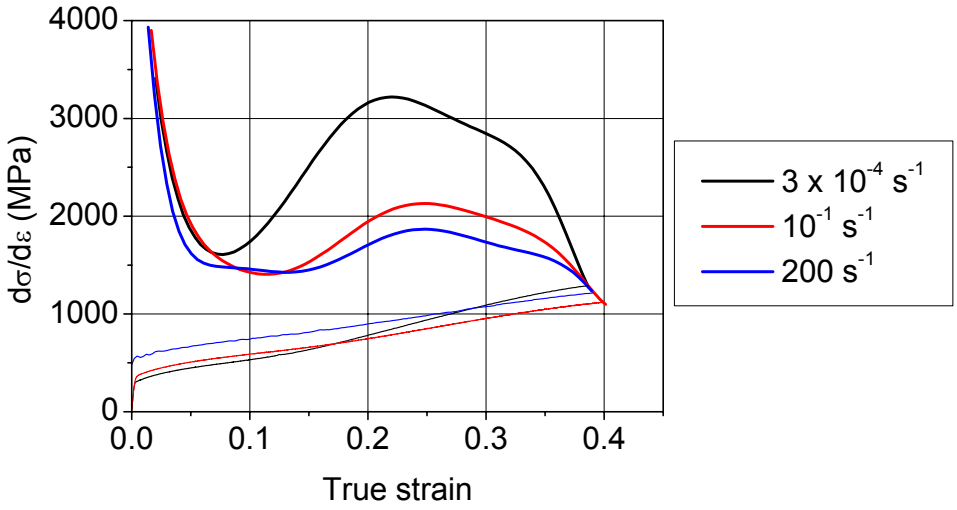

Figure 13 Work-hardening rates and true stress-strain curves of EN 1.4318-1 steel at strain rates 3×10^{-4}, 10^{-1} and 200 s^{-1} at room temperature

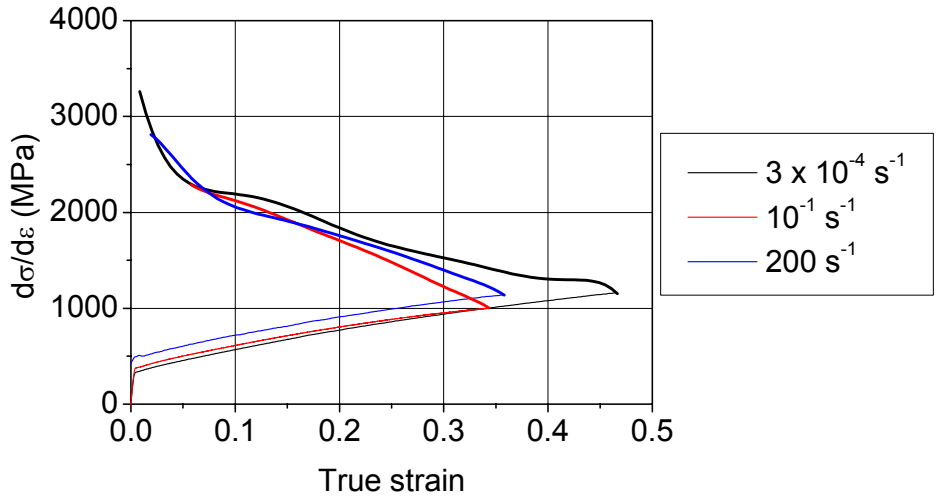

Figure 14 Work-hardening rates and true stress-strain curves of EN 1.4301 steel at strain rates 3×10^{-4}, 10^{-1} and 200 s^{-1} at room temperature

4.1.2 Adiabatic heating at high strain rates

The increase in the temperature of the tensile test samples tested at 10^{-1} s^{-1} at room temperature is presented as a function of true plastic strain in Figure 15. The measured temperatures are shown with the continuous black lines. The dashed red lines show the theoretical temperature increase, determined by assuming that the mechanical work done to the test samples was entirely converted to heat according to the following equation:

$$\Delta T = \frac{1}{\rho_d C}\int \sigma d\varepsilon , \tag{49}$$

where ρ_d is density and C is specific heat. The stable and unstable steels showed different characteristics. The stable EN 1.4301 steel exhibited a temperature increase of about 40 K, and the calculation overestimated the temperature increase. This is a consequence of the storage of the mechanical energy in the microstructure. It is, however, noteworthy that the fraction of stored energy, which for most metals and alloys is of the order of 0.1 (Bever, 1973), was significantly higher. The measured heating of the unstable EN 1.4318-1 steel was much higher, about 80 K. Contrary to the stable steel, the calculation overestimated the heating of the unstable steel at low strains, but underestimated at high strains. This was due to the negative free-energy change related to the strain-induced α'-martensite transformation, which was not taken into account in equation 49, and led to the higher adiabatic heating of the unstable steel.

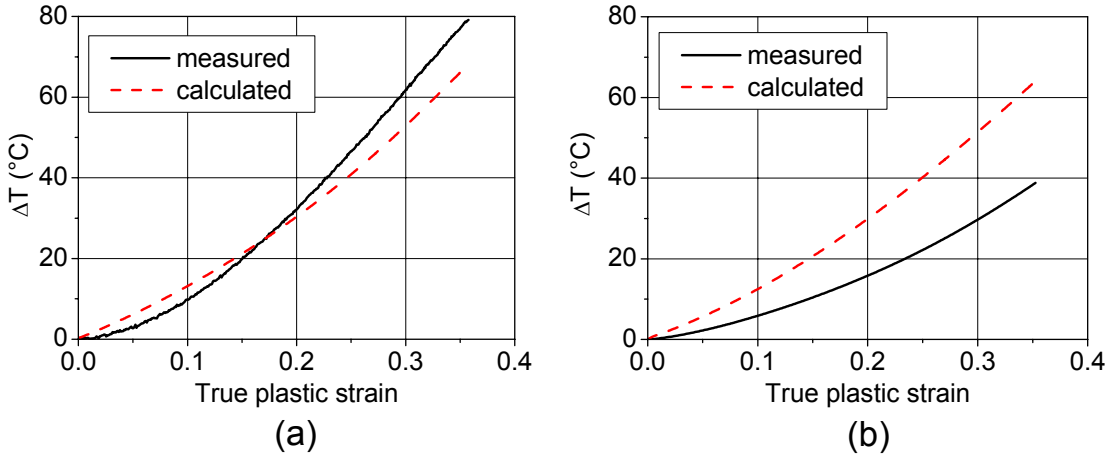

Figure 15 Measured and calculated temperature increases during uniaxial tensile deformation of (a) EN 1.4318-1 and (b) EN 1.4301 steels at 10^{-1} s^{-1} as a function of true plastic strain

4.1.3 Effect of temperature on tensile behaviour

The effect of temperature on the stress-strain curves of the EN 1.4318-2 steel tensile strained at 3×10^{-4} s^{-1} is illustrated Figure 16. The corresponding work-hardening rate curves are shown in Figure 17. The temperature had a strong influence on the mechanical response. Beyond the intrinsic effect of the temperature on the yield and tensile strengths, the work-hardening rate was significantly affected by the temperature. At the low temperatures, the abnormal work-hardening behaviour similar to the EN 1.4318-1 steel was observed, characterised by the work-hardening minima and maxima. However, with increasing temperature, the WHR peak shifted to higher strains and

decreased, and finally disappeared at 80°C. Analogously with the EN 1.4318-1 and EN 1.4301 steels, the uniform elongation was determined by the WHR according to Considére's criterion. Thus, the uniform elongation was strongly dependent on the temperature, and the lowest elongation was obtained at the low temperatures due to the rapidly increasing and decreasing WHR.

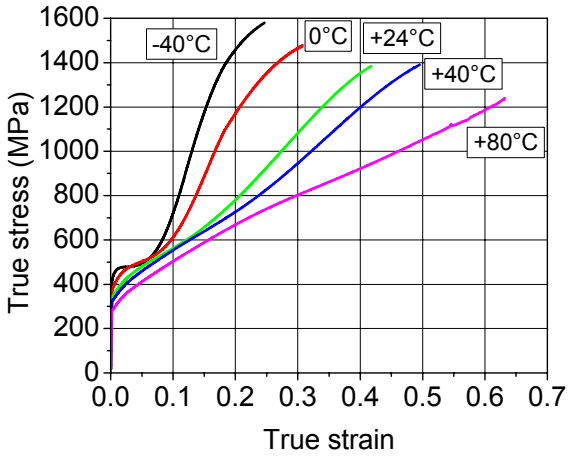

Figure 16 True stress-strain curves of EN 1.4318-2 steel tensile tested at strain rate 3×10^{-4} s^{-1} at temperatures -40, 0, +24, +40 and +80°C

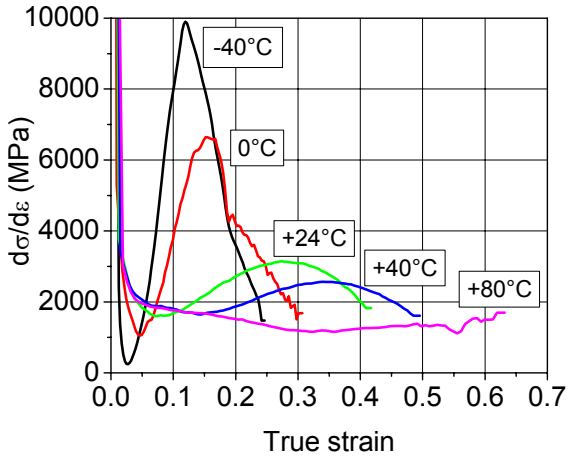

Figure 17 Work-hardening rate of EN 1.4318-2 steel tensile tested at strain rate 3×10^{-4} s^{-1} at temperatures -40, 0, +24, +40 and +80°C

4.2 Formation of strain-induced α'- and ε-martensite phases

4.2.1 Formation of α'-martensite

The volume fraction of strain-induced α'-martensite phase in the EN 1.4318-1 and EN 1.4301 steels tensile strained at various strain rates at room temperature is plotted as a function of true plastic strain in Figure 18. Each data point represents the α'-martensite volume fraction measured with the Ferritescope from an individual test sample after the straining to the requested plastic strain. The α'-martensite volume fraction in the EN 1.4318-2 steel tensile strained at 3×10^{-4} s^{-1} at various temperatures is plotted as a function of true plastic strain in Figure 19. The lines shown in Figures 18 and 19

represent the results of least squares fitting of the Olson-Cohen model (equation 18) to the experimental data. Constant value of 4.5 was used for the exponent n. The parameters α_{OC} and β_{OC} obtained by the fitting are shown in Table 5.

The results presented in Figures 18 and 19 demonstrate the strong influence of the chemical composition, strain rate and temperature on the austenite stability. The EN 1.4318 steel grades having the higher M_{d30} temperatures showed extensive α'-martensite formation at room temperature, whereas in the more highly alloyed EN 1.4301 steel the significant transformation occurred only at the lowest strain rate at high strain levels. Furthermore, the transformation of the EN 1.4301 steel was almost entirely suppressed at the higher strain rates. However, also a weak opposite effect of the strain rate was observed at the strain rate of 200 s^{-1} at the strains below 0.25, where the transformation was slightly enhanced by the high strain rate. Hecker *et al.* (1982) reported about a similar effect on AISI 304 steel. However, in the present case the promoting effect of the strain rate was weak. The results on the EN 1.4318-2 steel demonstrate the importance of the temperature in the austenite stability. The strain-induced α'-martensite transformation was markedly retarded with increasing temperature.

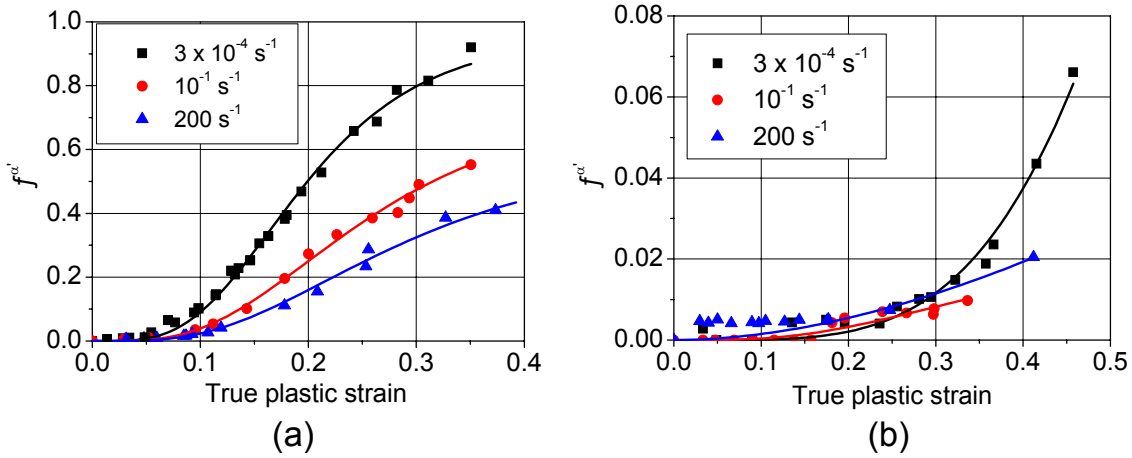

Figure 18 Volume fraction of strain-induced α'-martensite $f^{\alpha'}$ as a function of true plastic strain in (a) EN 1.4318-1 and (b) EN 1.4301 steels tensile strained at strain rates 3×10^{-4}, 10^{-1} and 200 s^{-1} at room temperature

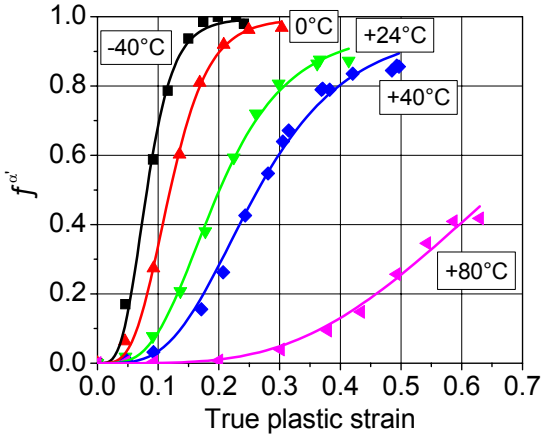

Figure 19 Volume fraction of strain-induced α'-martensite $f^{\alpha'}$ as a function of true plastic strain in EN 1.4318-2 steel tensile tested at strain rate 3×10^{-4} s^{-1} at temperatures -40, 0, +24, +40 and +80°C

The fitting results supported fairly well the hypotheses of the Olson-Cohen model. With an increasing strain rate, the parameter α_{OC} remained rather unaffected, but the parameter β_{OC} decreased, indicating a decreasing nucleation probability of the α'-martensite. Here, a remark has to be made: the Olson-Cohen model is an isothermal model, which was not the case in the tensile tests at high strain rates. Despite this, the observed fit between the model and the experimental data was good. The experiments on the EN 1.4318-2 steel showed that with increasing temperature the parameter α_{OC} decreased, indicating reduced generation of the shear bands. However, unlike suggested by Olson and Cohen (1975) and Hecker *et al.* (1982), the parameter β_{OC} did not seem to go to zero with increasing temperature, but in fact showed the highest value at the highest temperature (+80°C).

Table 5 Parameters α_{OC} and β_{OC} of Olson and Cohen's kinetic model for EN 1.4318-1 steel tensile strained at room temperature determined by least squares fitting

Strain rate	3×10^{-4} s^{-1}	10^{-1} s^{-1}	200 s^{-1}
α_{OC}	5.8±0.3	6.0±0.2	5.9±0.3
β_{OC}	3.8±0.5	1.5±0.1	0.9±0.1

Table 6 Parameters α_{OC} and β_{OC} of Olson and Cohen's kinetic model for EN 1.4318-2 steel tensile strained at strain rate 3×10^{-4} s^{-1} determined by least squares fitting

Temperature	-40°C	0°C	+24°C	+40°C	+80°C
α_{OC}	11.7±1.2	7.8±0.5	5.9±0.2	4.3±0.3	1.3±0.2
β_{OC}	6.1±1.4	6.6±1.1	3.6±0.3	4.0±0.5	9.1±5.8

The first derivatives $df^{\alpha'}/d\varepsilon$ of the modelled transformation curves of the EN 1.4318-1 and EN 1.4301 steels, representing the rate of the α'-martensite transformation, are shown in Figure 20. The transformation rate curves of the EN 1.4318-2 steel are shown in Figure 21.

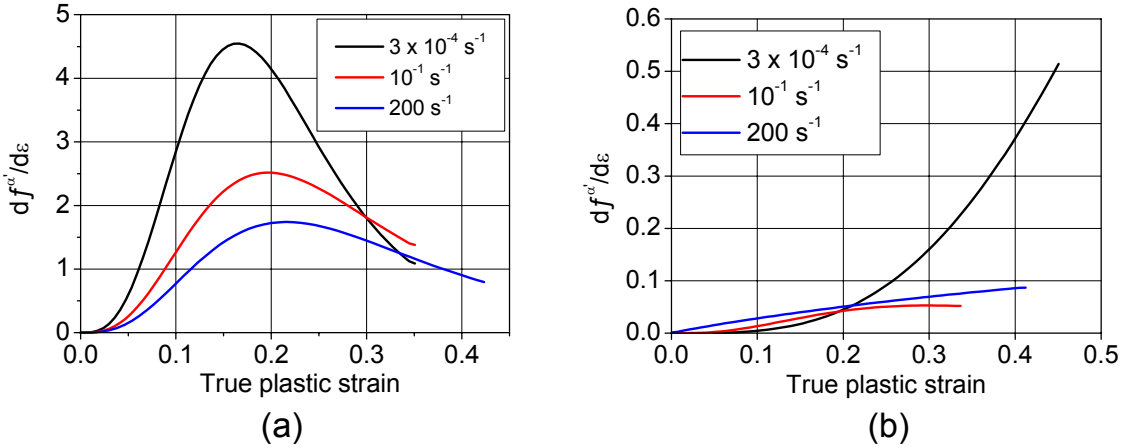

Figure 20 Rate of α'-martensite transformation $df^{\alpha'}/d\varepsilon$ as a function of true plastic strain in (a) EN 1.4318-1 and (b) EN 1.4301 steel at strain rates 3×10^{-4}, 10^{-1} and 200 s^{-1} at room temperature

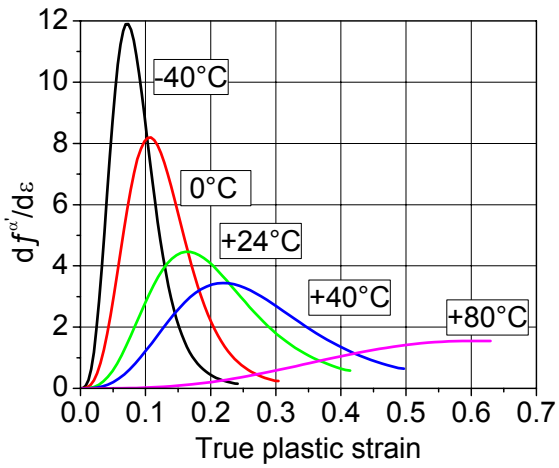

Figure 21 Rate of α'-martensite transformation $df^{\alpha'}/d\varepsilon$ as a function of true plastic strain in EN 1.4318-2 steel at strain rate 3×10^{-4} s^{-1} at temperatures -40, 0, +24, +40 and +80°C

The transformation rate curves revealed a close relationship between the mechanical response and the strain-induced α'-martensite transformation. The transformation rate curves of the unstable steel grades showed maxima whose height and location showed a similar strain rate and temperature dependence as the maxima in the WHR curves. In all cases, the maximum transformation rate was reached at a slightly lower strain than the WHR maximum. An excellent correlation was found at all studied strain rates and temperatures. Furthermore, at the low strain rate (3×10^{-4} s^{-1}) the transformation rate reached the highest value close to the α'-martensite volume fraction of 0.3 irrespective of the chemical composition or temperature. At the higher strain rates, the maximum was reached a bit earlier. Experimental results on several different austenitic stainless steel alloys not included in this thesis also supported the above finding, and in fact, similar behaviour can be found in almost every study presented in literature (*e.g.*, Angel, 1954).

The results presented above show that the α'-martensite transformed only after a certain plastic strain, depending on the chemical composition, strain rate and temperature. However, the processes leading to the strain-induced α'-martensite transformation, including the generation of the nucleation sites and the nucleation itself, are essentially controlled by the stress, as discussed in section 1.2. Therefore, it is reasonable to present the α'-martensite volume fractions as a function of applied stress. These plots are shown in Figures 22 and 23. The stress values were obtained by dividing the applied load at the end of the straining by the cross-sectional area of the sample measured after loading. Thus, the stress values represent the true stress values taking into account also the volume change due to the α'-martensite transformation.

Figures 22 and 23 indicate that there was a critical stress level for the onset of the α'-martensite transformation. The critical stress was much lower for the unstable EN 1.4318 steel grades compared to the stable EN 1.4301 steel. Furthermore, the critical stress increased with increasing strain rate and temperature. In the beginning, the relationship between $f^{\alpha'}$ and σ showed a parabolic shape. At the intermediate volume fractions, a rather linear relation was observed, but again at the high volume fractions a deviation from the linear trend was seen.

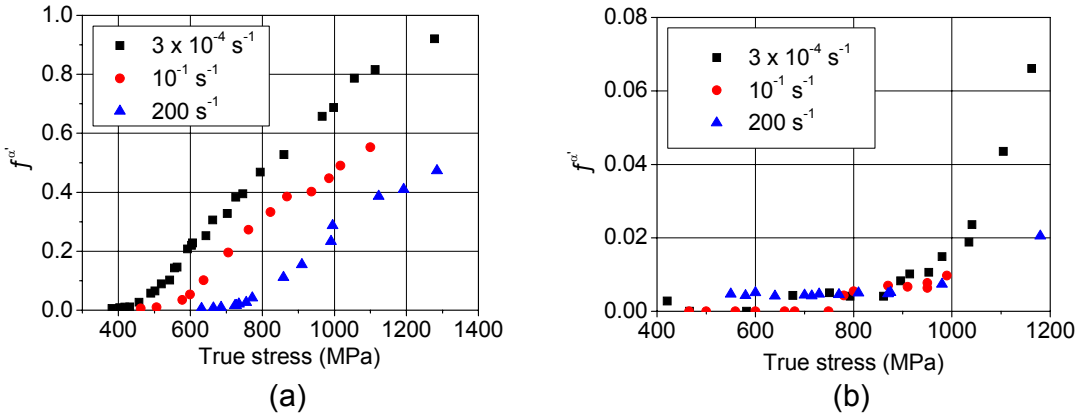

Figure 22 α'-martensite volume fraction $f^{\alpha'}$ as a function of true stress in (a) EN 1.4318-1 and (b) EN 1.4301 steels tensile strained at strain rates of 3×10^{-4}, 10^{-1} and 200 s^{-1} at room temperature

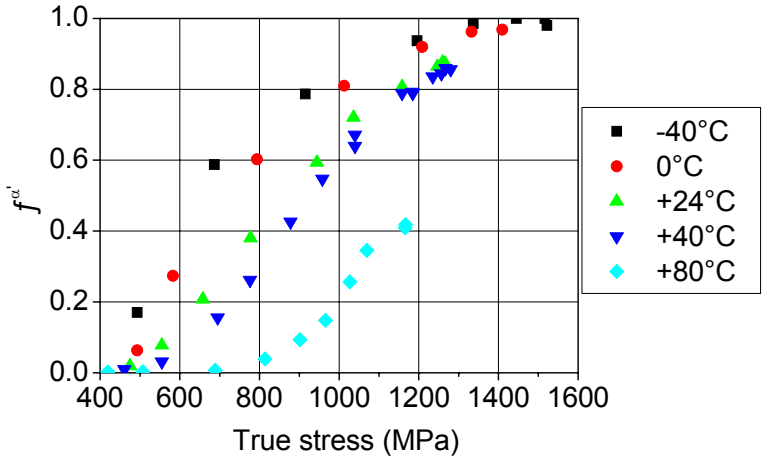

Figure 23 α'-martensite volume fraction $f^{\alpha'}$ as a function of true stress in EN 1.4318-2 steel tensile strained at strain rate 3×10^{-4} s^{-1} at temperatures of -40, 0, +24, +40 and +80°C

Fang and Dahl (1991) suggested that the flow stress of a metastable austenitic stainless steel is linearly proportional to the square root of $f^{\alpha'}$. Figure 24 presents the square root of the α'-martensite volume fraction of the EN 1.4318-1 steel as a function of the flow stress. Except for the beginning, the parabolic part of the $f^{\alpha'}$ vs. σ curve appears now to be linear. Furthermore, the plots show a well defined abrupt change in the slope at $(f^{\alpha'})^{1/2}\approx0.55$, corresponding to $f^{\alpha'}\approx0.3$. The change in the slope indicates that the volume fraction of 0.3 is somehow critical point, at which the strengthening effect of the α'-martensite phase is abruptly changed. One possible explanation for the observed behaviour might be the formation of a percolating cluster of α'-martensite.

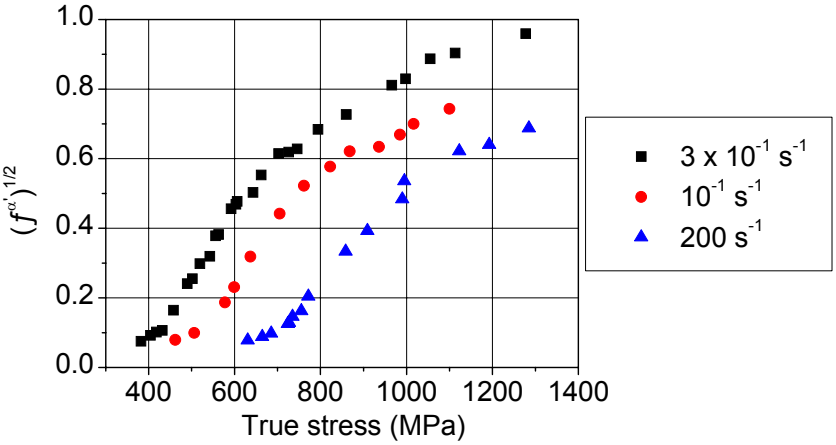

Figure 24 Square root of α'-martensite volume fraction $f^{\alpha'}$ as a function of true stress in EN 1.4318-1 steel tensile strained at strain rates 3×10^{-4}, 10^{-1} and 200 s^{-1} at room temperature

4.2.2 Formation of ε-martensite

The XRD measurements performed on the deformed samples indicated only weak ε-martensite reflections. Thus, no attempts to conduct quantitative analysis were made. However, a clear dependency between the chemical composition, deformation temperature and the presence of the ε-martensite reflections was found. In the unstable EN 1.4318-1 steel strained at room temperature, weak $\varepsilon10\bar{1}1$ reflections were distinguishable from the background within the plastic strain regime of 0.10-0.25. No influence of the strain rate on the ε-martensite formation could be observed. The EN 1.4318-2 steel tested at -40 and 0°C showed slightly better defined $\varepsilon10\bar{1}1$ reflections around the plastic strain of 0.1. An example of the $\varepsilon10\bar{1}1$ reflection of the highest intensity found in the EN 1.4318-2 steel is shown in Figure 25. In the EN 1.4301 steel strained at room temperature and in the EN 1.4318-2 steel strained at temperatures higher than 0°C no ε-martensite reflections could be distinguished from the background. Therefore, according to the results, the presence of the ε-martensite reflections was favoured by the low alloying and low temperature, both factors decreasing the SFE.

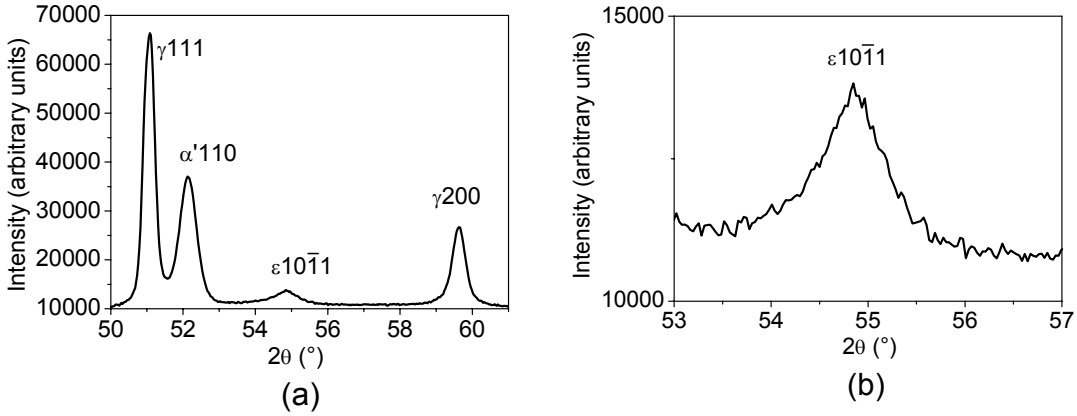

Figure 25 (a) γ111, $\varepsilon10\bar{1}1$, γ200 and α'110 reflections measured from EN 1.4318-2 steel strained to true plastic strain 0.09 at strain rate 3×10^{-4} s^{-1} at -40°C and (b) magnification of $\varepsilon10\bar{1}1$ reflection

4.3 Results of X-ray diffraction line broadening analysis

Integral breadths of the austenite 111 and 222, α'-martensite 110 and 220 and ε-martensite $\varepsilon 10\bar{1}1$ reflections of the EN 1.4318-1 steel tensile strained at 3×10^{-4} s^{-1} at room temperature are plotted as a function of true plastic strain in Figure 26. Other studied steels exhibited essentially similar characteristics, and the integral breadths are not given here, but the further analysis of these results is presented in the following sections.

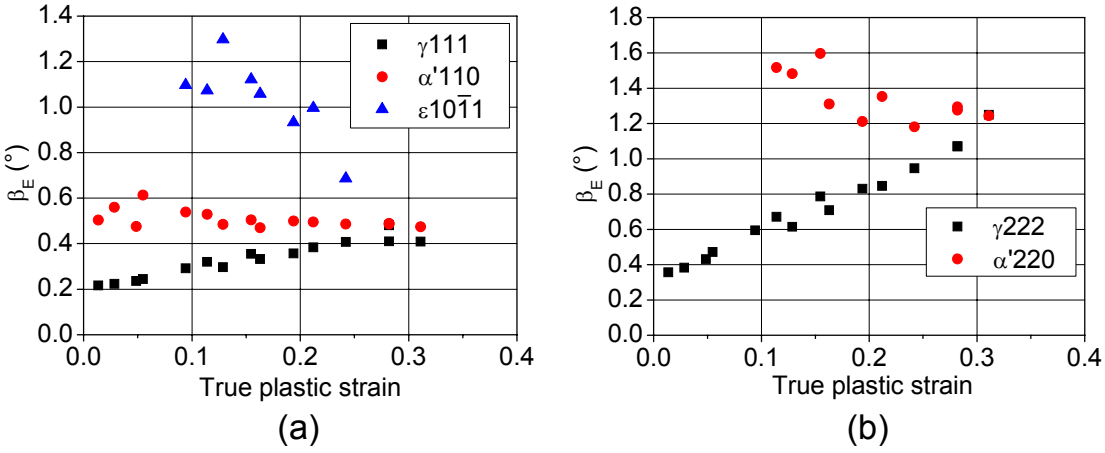

Figure 26 Integral breadths β_E of the measured (a) austenite 111, α'-martensite 110 and ε-martensite $10\bar{1}1$ reflections and (b) austenite 222 and α'-martensite 220 reflections in EN 1.4318-1 steel tensile strained at 3×10^{-4} s^{-1} at room temperature

Comparison between the integral breadths of the reflections of various phases reveals interesting features: integral breadths of the austenite reflections increased with increasing plastic strain, whereas the α'-martensite reflections were initially much broader, and with increasing plastic strain the integral breadths remained relatively unchanged. This indicates that the plastic deformation took place mostly in the austenite phase. The only detected ε-martensite reflection $\varepsilon 10\bar{1}1$ exhibited high integral breadth compared to the austenite and α'-martensite reflections. Due to the low intensities, accurate determination of the integral breadth of the $\varepsilon 10\bar{1}1$ reflections was difficult. However, it seems that the integral breadth did not significantly change with increasing plastic strain.

Two approaches, *viz.*, the integral breadth and the Voigt methods, were used to estimate the microstrains, domain sizes and dislocation densities from the XRD line broadening data. The results on the austenite phase are summarised in the following two sections. The comparison of the results obtained by IBM and VM is presented in section 4.3.3. The analysis of the XRD line broadening results on the α'-martensite phase are presented in section 4.3.4.

4.3.1 Analysis of austenite phase by integral breadth method

The root mean square microstrains $\langle\varepsilon^2\rangle^{1/2}$ and domain sizes $\langle D\rangle$ of the austenite phase in the EN 1.4318-1, EN 1.4301 and EN 1.4318-2 steels determined by the integral breadth method (equation 21) are plotted as a function of true plastic strain in Figures 27, 28 and 29, respectively.

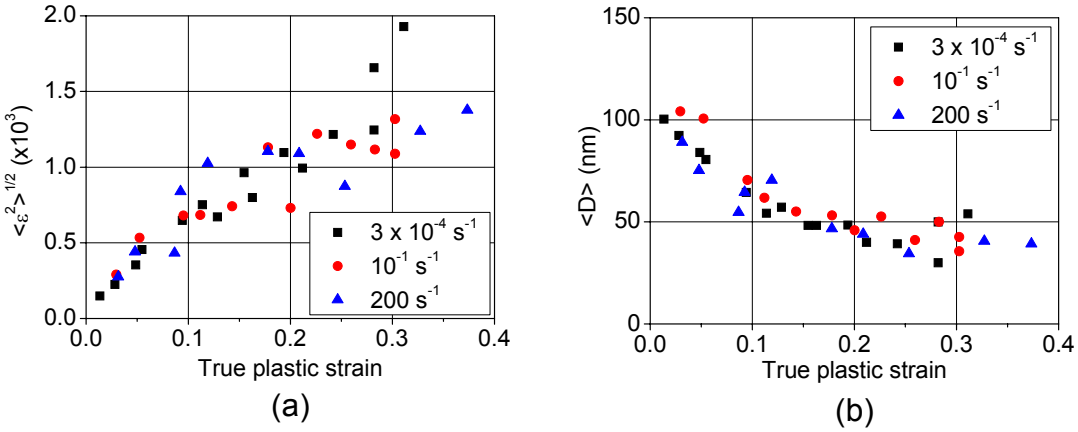

Figure 27 (a) Root mean square microstrain $\langle\varepsilon^2\rangle^{1/2}$ and (b) domain size $\langle D\rangle$ of austenite phase calculated by IBM as a function of true plastic strain in EN 1.4318-1 steel tensile strained at strain rates 3×10^{-4}, 10^{-1} and 200 s^{-1} at room temperature

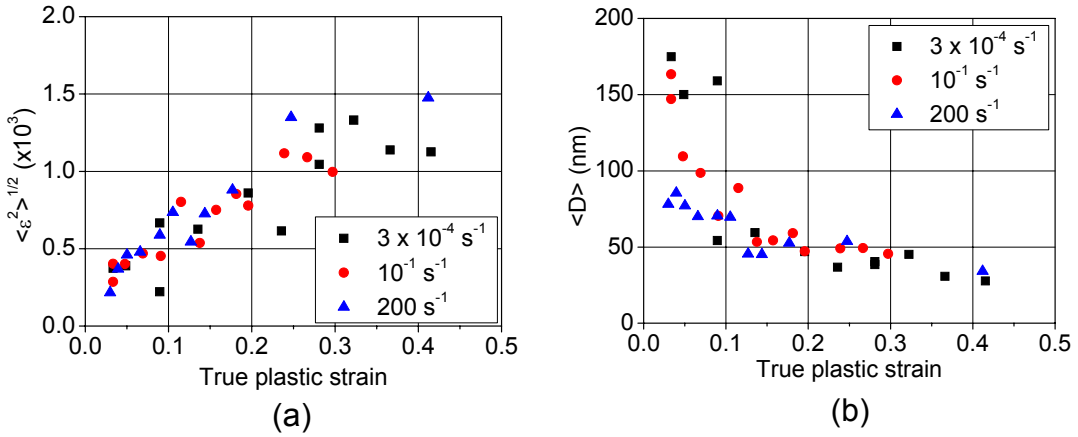

Figure 28 (a) Root mean square microstrain $\langle\varepsilon^2\rangle^{1/2}$ and (b) domain size $\langle D\rangle$ of austenite phase calculated by IBM as a function of true plastic strain in EN 1.4301 steel tensile strained at strain rates 3×10^{-4}, 10^{-1} and 200 s^{-1} at room temperature

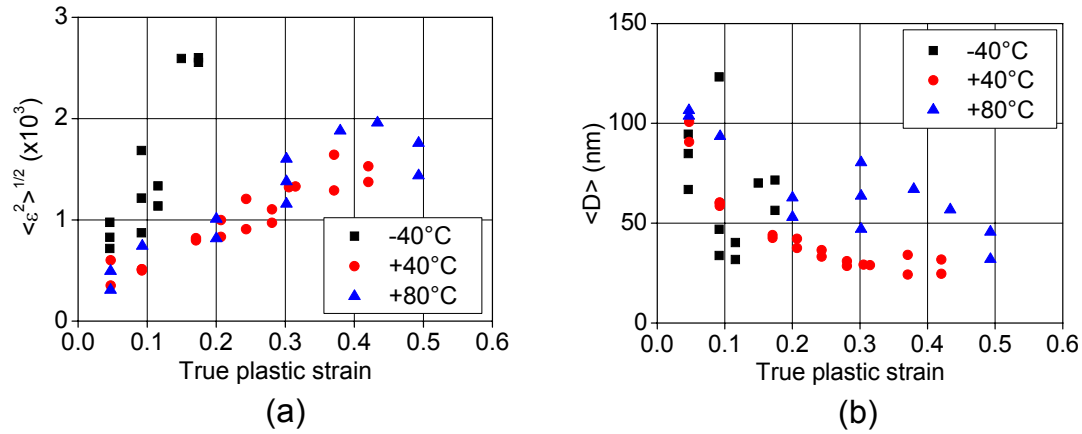

Figure 29 (a) Root mean square microstrain $\langle\varepsilon^2\rangle^{1/2}$ and (b) domain size $\langle D\rangle$ of austenite phase calculated by IBM as a function of true plastic strain in EN 1.4318-2 steel tensile strained at strain rate 3×10^{-4} s^{-1} at temperatures -40, +40 and +80°C

The RMSS increased and ⟨D⟩ decreased with increasing plastic strain in all studied steels, reflecting increasing dislocation density. The extent of the strain-induced α'-martensite transformation affected especially the RMSS: in the EN 1.4318-2 steel strained at -40°C the RMSS increased rapidly compared to the higher temperatures, indicating that the rapid α'-martensite transformation accelerated the dislocation generation in the austenite phase. Also in the EN 1.4318-1 steel the RMSS at a given plastic strain was higher than that in the stable EN 1.4301 steel. The effect of α'-martensite transformation on the domain size was found to be weaker so that the differences between the test conditions and materials were difficult to find.

The dislocation densities were calculated from the microstrain and domain size using equation 38. Figure 30 shows the dislocation density of the austenite phase as a function of true plastic strain in the test materials tensile strained at the strain rate of 3×10^{-4} s^{-1}. The results clearly reflected the influence of the α'-martensite transformation on the dislocation density of the austenite phase, as indicated by the values of RMSS and ⟨D⟩: in the unstable EN 1.4318-1 steel the dislocation density of the austenite at a given plastic strain was higher than that in the stable EN 1.4301 steel. In the EN 1.4318-2 steel the rate of the α'-martensite transformation was found to be strongly dependent on the temperature. Consequently, the dislocation density of the austenite increased more rapidly at the low temperatures. Thus, the results suggest that the rapid work hardening associated to the strain-induced α'-martensite transformation is related to the rapid generation of the dislocations in the austenite phase.

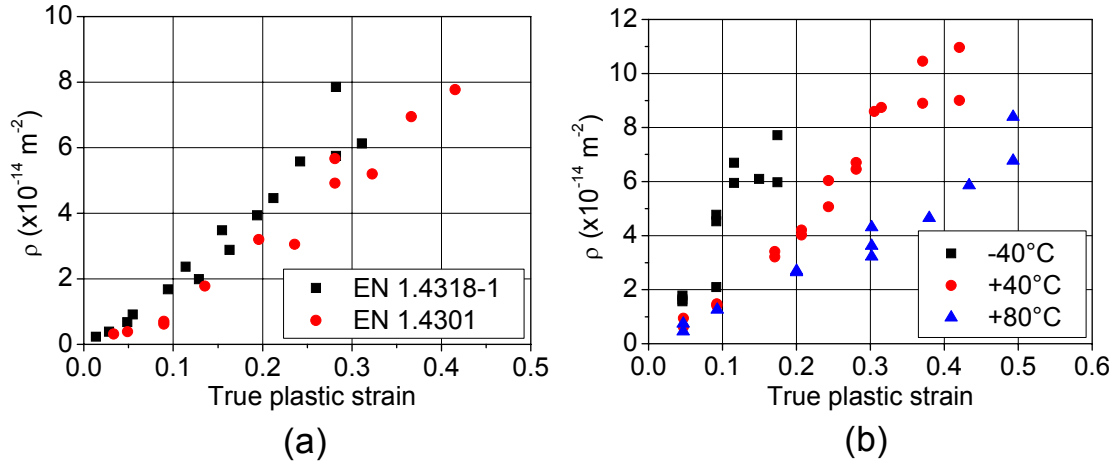

Figure 30 Dislocation density of austenite phase calculated by IBM as a function of true plastic strain in (a) EN 1.4318-1 and EN 1.4301 steels tensile strained at 3×10^{-4} s^{-1} at room temperature and in (b) EN 1.4318-2 steel tensile strained at 3×10^{-4} s^{-1} at temperatures -40, +40 and +80°C

The flow stress σ of a polycrystalline single-phase metal is known to be linearly proportional to the square root of the dislocation density ρ according to the relation:

$$\sigma = \sigma_0 + \alpha_0 Gb\sqrt{\rho}\,, \tag{50}$$

where σ_0 and α_0 are constants, G is shear modulus and b is Burgers vector. Therefore, it is reasonable to express the results of the dislocation density measurements in the form of flow stress vs. square root of dislocation density plots. Figure 31 shows the σ-$\rho^{1/2}$

plots of the austenite phase of the EN 1.4318-1 steel tensile strained at the strain rates of 3×10^{-4}, 10^{-1} and 200 s^{-1}.

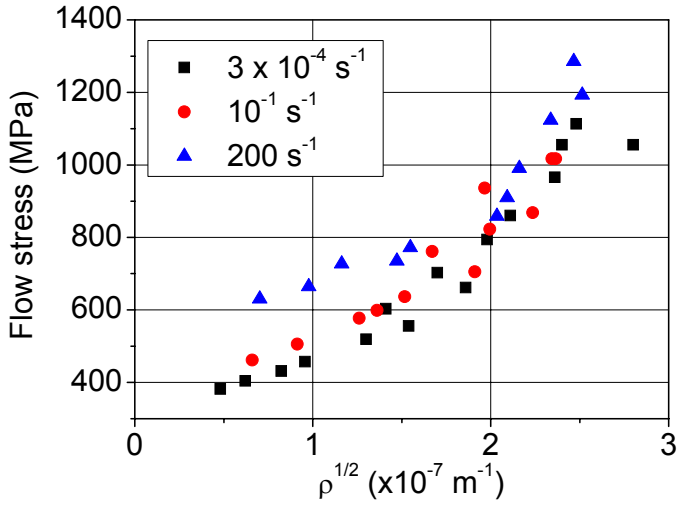

Figure 31 Flow stress as a function of square root of dislocation density of austenite phase in EN 1.4318-1 steel tensile strained at strain rates 3×10^{-4}, 10^{-1} and 200 s^{-1} at room temperature. Dislocation densities were calculated by IBM and equation 38.

According to the results, the linear dependence between the flow stress and the square root of the dislocation density of the austenite phase was valid in spite of the formation of the strain-induced α'-martensite phase. However, the experimental results deviated from the linear trend at the high stresses, corresponding to the high α'-martensite volume fractions. Comparison of the plots shown in Figure 31 with the results presented in Figure 24 reveals that the deviation from the linear trend occurred at the point at which the stress vs. square root of α'-martensite volume fraction plots showed a change in the slope. Thus, the point corresponded to the α'-martensite volume fraction of about 0.3.

It is also interesting to examine the effect of strain rate on the relationship between the flow stress and dislocation density. Below the changing point of the slope, the higher strain rate resulted in the higher flow stress at a given dislocation density, which is an indication of the reduced thermal activation of the dislocation motion at the high strain rates. However, above the changing point, the plots corresponding to the different strain rates seemed to overlap.

The σ-$\rho^{1/2}$ plots of the austenite phase of the EN 1.4301 steel are shown in Figure 32. In contrast to the behaviour of the EN 1.4318-1 steel, the relationship was found to be linear. This results obviously from the fact that only little α'-martensite was formed in the course of the plastic deformation. It is also noteworthy that the strain rate did not have as strong influence on the flow stress at a given dislocation density as for the EN 1.4318-1 steel, but the plots determined at the different strain rates almost overlapped.

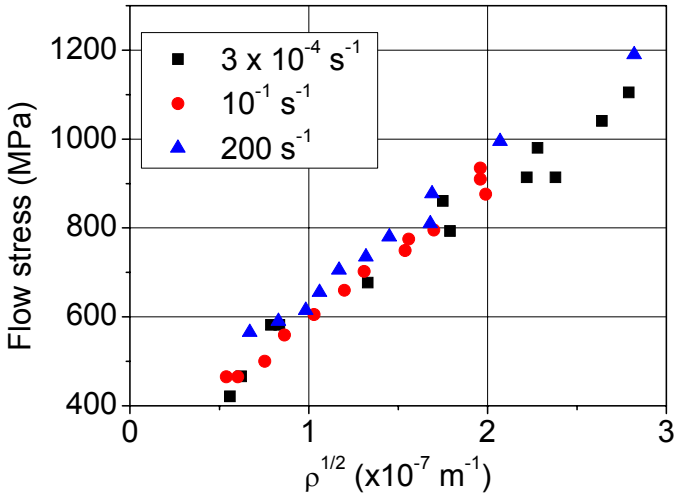

Figure 32 Flow stress as a function of square root of dislocation density of austenite phase in EN 1.4301 steel tensile strained at strain rates 3×10^{-4}, 10^{-1} and 200 s^{-1} at room temperature. Dislocation densities were calculated by using IBM and equation 38.

Figure 33 shows the σ-$\rho^{1/2}$ plots of the austenite phase of the EN 1.4318-2 steel tensile strained at 3×10^{-4} s^{-1} at temperatures of -40, +40 and +80°C. Although the number of data points was limited and the data showed high scattering, the influence of the variation of the α'-martensite transformation rate with the deformation temperature can be seen in the plots. At +80°C, the plot was linear, as only little α'-martensite was formed. At -40°C α'-martensite was formed rapidly, resulting in the change of the slope of the σ-$\rho^{1/2}$ plot.

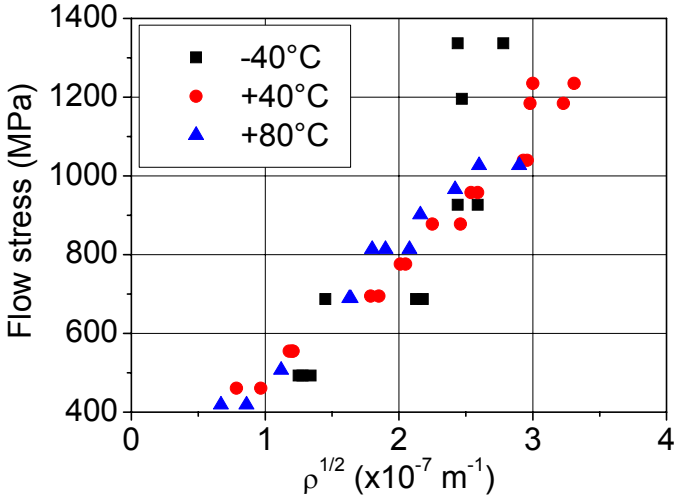

Figure 33 Flow stress as a function of square root of dislocation density of austenite phase in EN 1.4318-2 steel tensile strained at strain rate 3×10^{-4} s^{-1} at temperatures -40, +40 and +80°C. Dislocation densities were calculated by using IBM and equation 38.

The non-linear behaviour of the σ-$\rho^{1/2}$ plots of the unstable steel grades indicates that in addition to the enhanced dislocation generation in the austenite phase, the strain-induced α'-martensite transformation has also another strengthening contribution, which becomes operative at high α'-martensite volume fractions. The slope of the σ-$\rho^{1/2}$ plots

became higher when the α'-martensite volume fraction exceeded about 0.3, indicating that the flow stress is no longer determined by the dislocation density of the austenite alone. This may be rationalised in terms of the formation of an infinite, *i.e.*, percolating cluster of the α'-martensite. Thereafter, the two-phase aggregate can no longer be deformed without the deformation of the hard α'-martensite phase, since the α'-martensite constitutes a strong percolating cluster extending through the body. As a consequence, the role of the α'-martensite in determining the flow stress of the aggregate becomes more significant, which manifests itself as the higher slope of σ-$\rho^{1/2}$ plots. The theoretical percolation threshold in a statistical cube lattice is known to be 0.3116 (Stauffer and Aharony, 1994), which corresponds well to the present findings.

When considering the dislocation density measurement results, one must be aware of the simplifications and assumptions made concerning the dislocation arrangements. The dislocation densities were calculated with equation 38, which assumes a completely uniform dislocation distribution and no interaction between the strain fields of adjacent dislocations. It is, therefore, reasonable to compare also the dislocation densities ρ_D and ρ_S, calculated from the microstrain and domain size alone by using equations 30 and 33. Figures 34a and 34b present the comparison of the square roots of these dislocation densities of the austenite phase in the EN 1.4318-1 and EN 1.4301 steels strained at 3×10^{-4} s^{-1}, respectively. The calculations were performed assuming a uniform dislocation distribution and no interaction between the dislocations. The results show that for both steels $\rho_D>\rho_S$. This is most probably caused by the interaction of the stress fields of the adjacent dislocations, which decreases the RMSS, and leads to underestimation of the dislocation density ρ_S. However, taking into account the high scattering, the correlation between ρ_D and ρ_S was quite good. Also the trends, including the change in the slope of the EN 1.4318-1 steel, corresponded well.

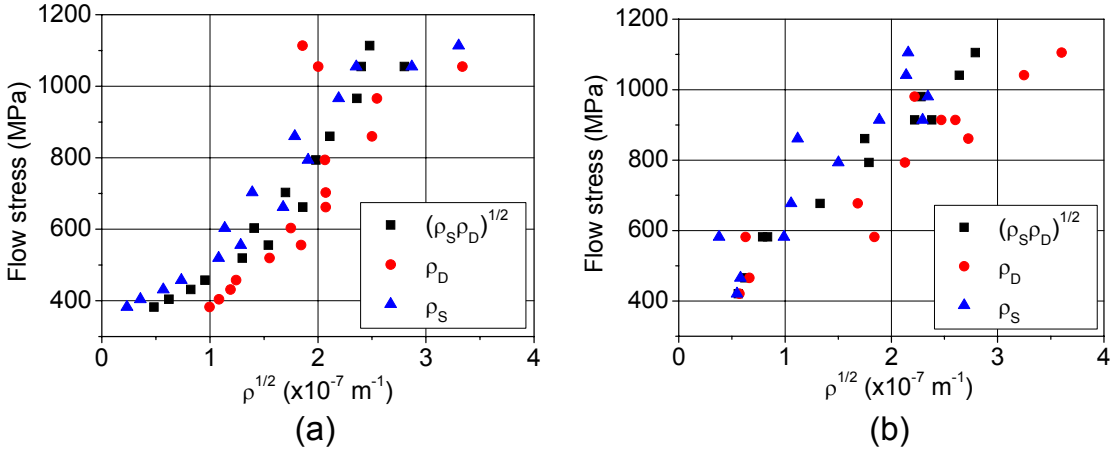

Figure 34 Comparison of the square roots of dislocation densities ρ, ρ_D and ρ_S of austenite phase in (a) EN 1.4318-1 steel and (b) EN 1.4301 steel tensile strained at strain rate 3×10^{-4} s^{-1} at room temperature

4.3.2 Analysis of austenite phase by Voigt method

The root mean square microstrain and the domain size ⟨D⟩ of the austenite phase of the EN 1.4318-1 and EN 1.4301 steels tensile strained at the strain rates of 3×10^{-4}, 10^{-1} and 200 s^{-1} are plotted as a function of true plastic strain in Figures 35 and 36, respectively. The Voigt method gave the RMSS as a function of averaging length, which therefore

needed to be chosen. It was assumed that the size of the strain field of a dislocation corresponded to half of the volume-weighted domain size, which was used as the averaging length. The domain sizes reported are the volume-weighted domain sizes.

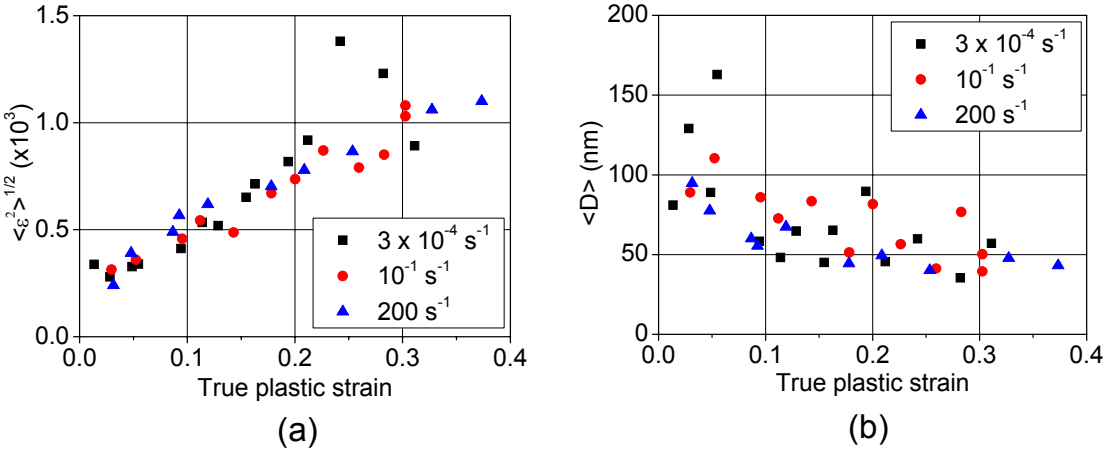

Figure 35 (a) Root mean square microstrain $<\varepsilon^2>^{1/2}$ and (b) domain size ⟨D⟩ of austenite phase calculated by VM as a function of true plastic strain in EN 1.4318-1 steel tensile strained at strain rates 3×10^{-4}, 10^{-1} and 200 s^{-1} at room temperature

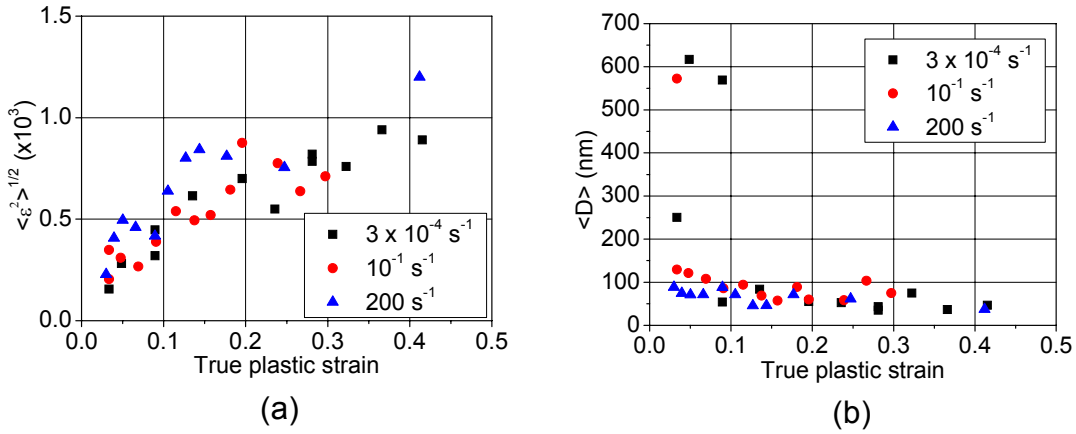

Figure 36 (a) Root mean square microstrain $<\varepsilon^2>^{1/2}$ and (b) domain size ⟨D⟩ of austenite phase calculated by VM as a function of true plastic strain in EN 1.4301 steel tensile strained at strain rates 3×10^{-4}, 10^{-1} and 200 s^{-1} at room temperature

The volume-weighted domain sizes and the corresponding RMSSs determined by means of the Voigt method were used to calculate the dislocation densities, as also the integral breadth method gave the volume-weighted ⟨D⟩ (Balzar, 1999). Furthermore, equation 38 was used. The relation between the flow stress and the square roots of the dislocation densities of the austenite phase in the EN 1.4318-1 and EN 1.4301 steels are shown in Figure 37. The dislocation densities obtained by the VM showed higher scattering, but quantitatively the results correlated fairly well with the results obtained by the IBM.

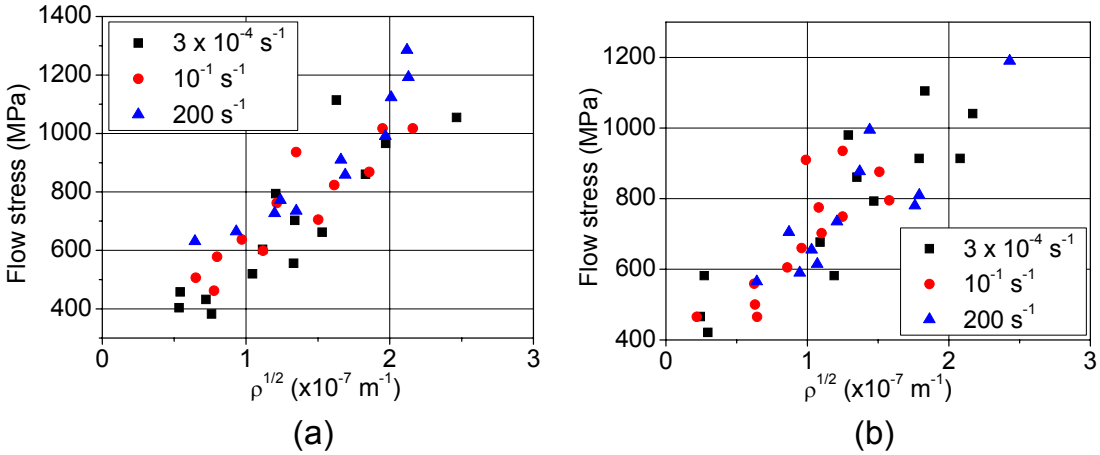

Figure 37 Relation between flow stress and square root of dislocation density of austenite phase of (a) EN 1.4318-1 and (b) EN 1.4301 steels tensile strained at 3×10^{-4}, 10^{-1} and 200 s^{-1}. Dislocation densities were calculated by using Voigt method and equation 38.

4.3.3 Comparison of integral breadth and Voigt methods

In general, a good correlation between the integral breadth and Voigt methods was found. However, the integral breadth method indicated higher root mean square microstrains. This probably originates from the omitting of the Lorentzian component of the strain broadening. Another distinct feature was that the results obtained by the Voigt method showed higher scattering. Obviously, this was a consequence of the poor quality of the XRD data, which in particular affected the data analysis of the EN 1.4318-1 steel. At the high α'-martensite volume fractions the austenite reflections, especially γ222, were so weak that accurate determination of the line shape by the Voigt function and the precise determination of the Gaussian and Lorentzian broadening components was impossible.

The dislocation densities of the austenite phase of the EN 1.4318-1 and EN 1.4301 steels calculated by the IBM and VM are compared in Figures 38 and 39, respectively. At a given stress level, the Voigt method gave lower dislocation densities, and the results showed higher scattering. But what is more important, the trends indicated by both methods were equivalent, *i.e.*, the EN 1.4301 steel showed a continuously linear relation between the flow stress and the square root of the dislocation density, whereas the unstable EN 1.4318-1 steel had a changing point in the slope. However, due to the high scattering in the case of the VM, the change in the slope was hardly observable. Also the results of the linear fit to the data are shown in Figures 38 and 39. With the EN 1.4318-1 steel, fitting was limited below the changing point, where the dislocation density of the austenite was assumed to have a stronger effect on the flow stress. Interestingly, the slope of the EN 1.4318-1 steel was considerably lower than that of the stable EN 1.4301 steel, *i.e.*, at a given dislocation density the stable steel showed higher flow stress. However, after the changing point at about 650 MPa the slope of the EN 1.4318-1 steel became higher than the slope of the EN 1.4301 steel.

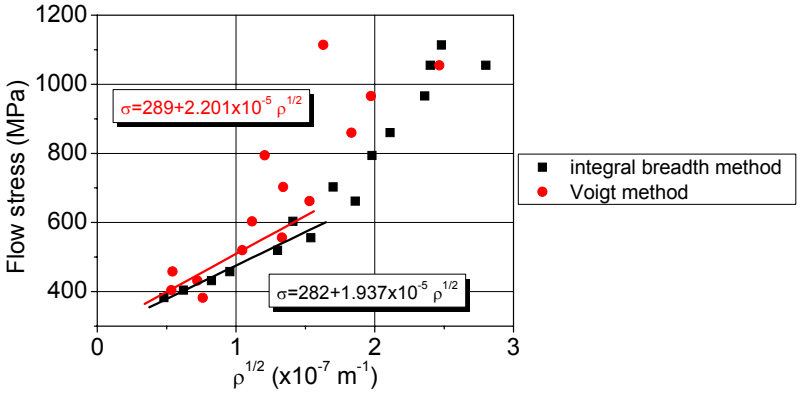

Figure 38 Comparison of the flow stress vs. square root of dislocation density of austenite plots determined by IBM and VM for EN 1.4318-1 steel tensile strained at strain rate 3×10^{-4} s^{-1} at room temperature

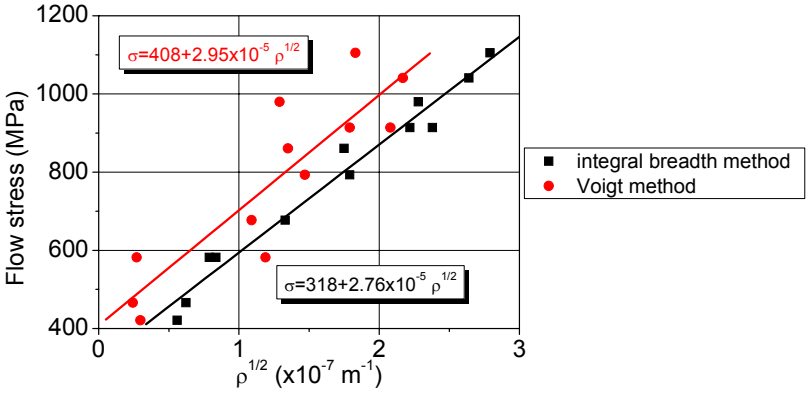

Figure 39 Comparison of the flow stress vs. square root of dislocation density of austenite plots determined by IBM and VM for EN 1.4301 steel tensile strained at strain rate 3×10^{-4} s^{-1} at room temperature

The results of the XRD line broadening analysis showed fairly good correlation with the dislocation density measurement results on austenitic stainless steels presented in literature. Staudhammer and Murr (1980) measured dislocation densities between 10^{14}-10^{15} m^{-2} (corresponding to $\rho^{1/2}=10^7$-3.2×10^7 m^{-1}) from cold rolled and shock loaded AISI 304 and 316 steels in their TEM experiments. Lee and Lin (2002) carried out TEM dislocation density measurements on AISI 304L steel strained in compression. They found the dislocation density to be linearly proportional to the square of the flow stress, and the measured dislocation densities varied between 10^{15}-5×10^{15} m^{-2} ($\rho^{1/2}=3.2\times10^7$-7×10^7 m^{-1}). Hoshino (1983) measured with XRD dislocation densities of 10^{14}-2×10^{15} m^{-2} ($\rho^{1/2}=10^7$-4.5×10^7 m^{-1}) from the austenite phase in deformed metastable austenitic stainless steel. Narutani (1989) performed XRD line broadening analysis on AISI 301 steel by means of the integral breadth method. The results ranged between 10^{14} and 2.5×10^{15} m^{-2} ($\rho^{1/2}=10^7$-5×10^7 m^{-1}).

4.3.4 XRD line broadening analysis of α'-martensite phase

The XRD line broadening analysis of the strain-induced α'-martensite phase was carried out using the integral breadth method on the EN 1.4318-1 steel tensile strained

at room temperature at 3×10^{-4} s^{-1} and on the EN 1.4318-2 steel tensile strained at 3×10^{-4} s^{-1} at -40°C, which exhibited significant formation of the α'-martensite phase. Obviously, the line broadening analysis could not be carried out when the α'-martensite volume fraction was low due to the low intensity of the diffraction lines. The lowest limit for the analysis was about $f^{\alpha'}$=0.2. Figure 40 presents the root mean square microstrains and domain sizes of the α'-martensite phase as a function of true plastic strain in the EN 1.4318-1 and EN 1.4318-2 steels. The root mean square microstrain of the α'-martensite phase was overall significantly higher than that of the austenite phase, whereas the domain size was mostly smaller. Both of these findings imply that the α'-martensite has a higher dislocation density than the austenite phase. Furthermore, both RMSS and ⟨D⟩ showed rather constant values, or even opposite trends compared to the austenite phase.

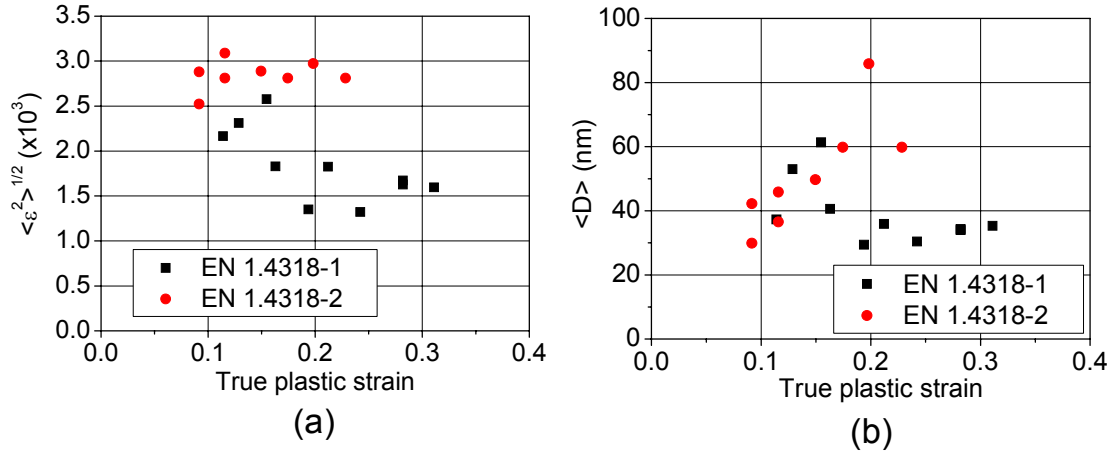

Figure 40 (a) Root mean square microstrain $\langle\varepsilon^2\rangle^{1/2}$ and (b) domain size ⟨D⟩ of the α'-martensite phase determined by IBM in EN 1.4318-1 steel strained at 3×10^{-4} s^{-1} at room temperature and in EN 1.4318-2 steel strained at 3×10^{-4} s^{-1} at -40°C

The dislocation densities of the α'-martensite phase of the EN 1.4318-1 and EN 1.4318-2 steels, calculated with equation 38, are plotted as a function of true plastic strain in Figure 41. The corresponding dislocation densities of the austenite phase are also shown.

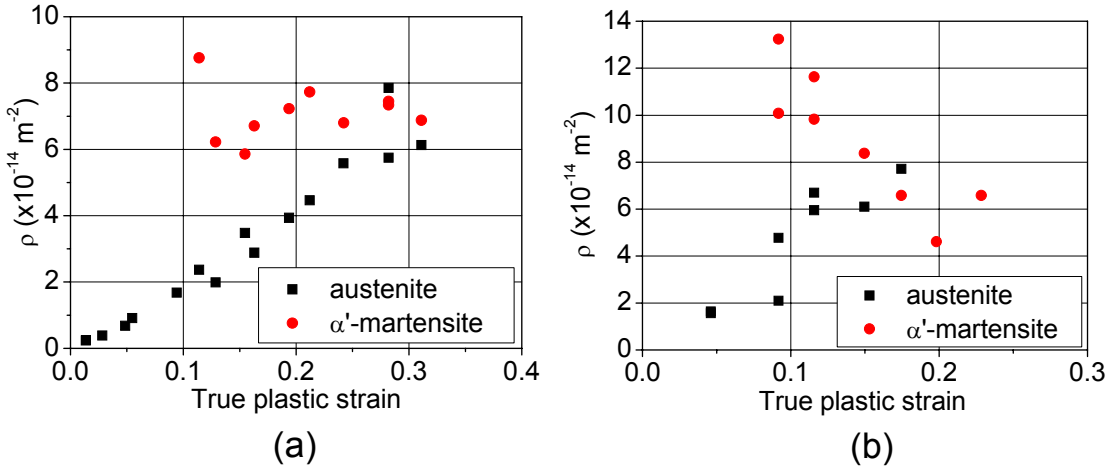

Figure 41 Dislocation density of the austenite and α'-martensite phases determined by IBM as a function of true plastic strain in (a) EN 1.4318-1 steel strained at 3×10^{-4} s^{-1} at room temperature and (b) EN 1.4318-2 steel strained at 3×10^{-4} s^{-1} at -40°C

The dislocation density measurement results showed two important features, also indicated by the ⟨D⟩ and RMSS: the dislocation density of the α'-martensite phase remained relatively constant, or even seemed to decrease with increasing plastic strain. Furthermore, the dislocation density of the α'-martensite was much higher than that of the austenite phase. Only at the late stages of the plastic deformation, when the α'-martensite volume fraction was almost 1, the dislocation density of the austenite reached the dislocation density of the α'-martensite.

When analysing the XRD broadening analysis results of the α'-martensite phase, it must be noticed that the information obtained by the XRD analysis is an average from the volume covered by the X-ray beam. As new α'-martensite embryos are formed continuously throughout the plastic deformation, the results of the XRD broadening analysis are an average from several α'-martensite nuclei having different deformation histories, depending on whether the nuclei were formed at the early or later stages of the deformation.

However, the results of the line broadening analysis show that the dislocation density of the α'-martensite phase is initially high compared to the austenite phase and is not significantly changed in the course of the plastic deformation of the austenite-α'-martensite aggregate. This means that in the early stages of the deformation, the α'-martensite particles are much harder than the austenite, and probably cause dispersion hardening. Because the RMSS, ⟨D⟩ and ρ of the α'-martensite did not change much with the increasing plastic strain, the plastic deformation is believed to occur mainly in the austenite phase. However, the calculated dislocation density seemed to slightly decrease, especially in the EN 1.4318-2 steel strained at -40°C, in which a large amount of α'-martensite was formed rapidly. The decreasing ρ is probably not an indication of the decreasing dislocation density, but evidence of the dynamic recovery and formation of low-energy dislocation structures (LEDS). These phenomena decrease the RMSS and increase ⟨D⟩, both of which were observed to some extent. As the dislocation structures of the α'-martensite are a result from the phase transformation, and are probably far from a stable configuration, even a small amount of plastic deformation can cause a significant rearrangement of the dislocations in the α'-martensite phase. Consequently, as the approach used in this study was not able to provide quantitative information about the dislocation arrangement, the experimental results are believed to underestimate the actual dislocation density of the α'-martensite phase.

Narutani (1989) carried out XRD line broadening analysis on metastable austenitic stainless steel, and found that the α'-martensite exhibited a much higher dislocation density than the austenite phase. The dislocation density of the α'-martensite was found to be 1.9×10^{16} m^{-2}. Pešička *et al.* (2003) measured dislocation densities of 9.26×10^{14} and 9.4×10^{14} m^{-2} from 12Cr martensitic steel by TEM and XRD, respectively. Hoffmann *et al.* (1997) carried out XRD dislocation density measurements on hardened plain carbon steels with C contents varying between 0.10 and 0.43%. The dislocation densities of the martensites having the low and high C contents were found to be 10^{15} and 5×10^{15} m^{-2}, respectively. Therefore, the results of the present study, indicating the dislocation densities ranging between 6×10^{14} and 14×10^{14} m^{-2}, seem to correlate fairly well with the measured dislocation densities of the thermally induced martensites. As discussed above, the dislocation density is most probably underestimated by the XRD

line broadening analysis, since the analysis does not take into account the presence of the LEDS.

4.3.5 Reliability of XRD line broadening analysis

A rather good correlation between the measured dislocation densities and the results presented in the literature was found. Nevertheless, the dislocation density measurements performed by means of the XRD line broadening analysis have several sources of uncertainty and systematic errors.

As shown in Figure 26, the measured integral breadths showed consistent trends, *i.e.*, the integral breadths of the austenite lines increased with increasing plastic strain, whereas the α'-martensite lines were rather unaffected. However, the accuracy of the determination of the microstrain and domain size was limited, because only two orders of reflections were available. Consequently, a data set comprising only two data points had to be used for determining the slope and y-intercept of equation 27 (*i.e.*, e and ⟨D⟩). Similarly, the separation of the size and strain broadening components in the Voigt method relied on only two data points. Obviously, this reduced the reproducibility of the measurements. However, for both e and ⟨D⟩ rather good trends were obtained, as shown in Figures 27-29 and 35-36. It is also noteworthy that the errors arising from the scatter of the integral breadth measurement results were compensated in the calculation of dislocation densities. This may be rationalised by examining equations 27 and 38. If the deviation of the measured integral breadth makes the slope of equation 27 to increase, the y-intercept decreases correspondingly. It is further observed that the RMSS is proportional to the square root of the y-intercept, whereas the domain size is inversely proportional to the slope. Thus, any deviation of the integral breadth caused an error of same sign in both RMSS and domain size. From equation 38 it appears that in the calculation of the dislocation density the RMSS is in the numerator and the domain size in the denominator. Thus, the deviations in the RMSS and domain size due to the experimental errors of β tended to be compensated in the calculation of the dislocation densities.

When using the IBM, systematic errors may arise due to the assumptions made concerning the shapes of the microstrain and domain size distributions. This applies both to the removal of the instrumental broadening and the determination of the microstrain and domain size. In the Voigt method these errors were avoided. However, a fairly good correlation between the IBM and VM was observed, indicating that also the results of the IBM were representative. The only distinct difference was that the Voigt method indicated lower values of RMSS than the IBM.

The most serious limitation of the XRD line broadening analysis was related to the estimation of the dislocation densities. The estimation of the dislocation densities relied on simple models, neglecting any other sources of broadening. A completely random dislocation arrangement and no interaction between the dislocations were assumed, which are certainly not true for highly deformed austenitic stainless steels. It is clear that such a simple approach is not capable to give accurate quantitative values of the dislocations densities. However, this was not the objective of the present analysis. Instead, trends in the evolution of the dislocation densities were sought, which appeared to be successful.

4.4 Stacking fault energy measurements

4.4.1 Stacking fault energy measurement results

The results of the stacking fault energy measurements are summarised in Table 7, which shows the measured stacking fault probabilities, mean square microstrains averaged over the distance of 50 Å, the stacking fault energies calculated with equation 45 and the standard deviations of five measurements. As may be expected based on the observed tendencies to the α'-martensite transformation, the unstable EN 1.4318 steel grades had lower SFEs than the stable EN 1.4301 steel, and the least stable EN 1.4318-1 had the lowest SFE.

Table 7 Mean square microstrains averaged over 50 Å, stacking fault probabilities and intrinsic stacking fault energies of the test materials measured by XRD at room temperature

Steel	$\langle\varepsilon_{50}^2\rangle \times 10^6$	$\alpha \times 10^3$	γ (mJ/m^2)
EN 1.4318-1	4.6±0.5	6.4±1.1	12.8±1.5
EN 1.4318-2	4.0±0.6	4.9±2.2	14.7±0.8
EN 1.4301	4.3±0.7	4.3±0.5	17.8±1.2

4.4.2 Reliability of stacking fault energy measurement results

The SFE measurement results exhibited low standard deviations. This signifies good reproducibility of the measurements, but does not tell anything about possible systematic errors. The measurement of the SFE by XRD relied on two parameters extracted from the XRD data: the mean square microstrain and the stacking fault probability. Extracting of these parameters involved several assumptions and complicated calculations, which are discussed in the following.

The uncertainties of the mean square microstrain determination were discussed in section 4.3.5. Since the Voigt method was used in the SFE measurements, the determination of the mean square microstrain should not involve bias. However, the calculation of the dislocation density involves uncertainty due to the assumptions made concerning the dislocation arrangements. Any errors of the model used reflect to the value of the dislocation density, and thus to the SFE. Furthermore, in the present study the estimation of the dislocation density was based only on the mean square microstrain, and the domain size was ignored.

The determination of the SFP is based on the measurement of very small displacements of the line profiles. However, due to the low SFEs of the studied steels, the displacements were measurable and the standard deviations of the SFPs were relatively low. The derivation of the SFP from the line profile displacements involves complicated calculations that have been thoroughly described by Warren (1990). Recently, Velterop *et al.* (2000) discussed the limitations of Warren's approach. It was demonstrated that the relation between the SFP and line profile displacements may be highly non-linear. Nonlinearity may arise if the twin fault probability or domain size is large. Fortunately, the SFPs measured in this study were lower than the SFPs where severe deviation from the linearity was observed by Velterop *et al.* (2000). A thorough analysis of the SFP determination would be beyond the scope of the present thesis. However, it is important

to recognise the limitations of the experimental technique used, and that the results involve several possible sources of systematic error.

In Table 8 the experimental results are compared with the SFEs calculated by using the compositional equations taken from literature. The equation determined by Brofman and Ansell (1978) showed the best correlation with the experimental results, and indicated lower SFE for the EN 1.4318 steels. It is, however, noteworthy that none of the equations included the effect of the nitrogen content, which in the case of the EN 1.4318 steels certainly had a pronounced effect on SFE. Furthermore, the equations have been determined by multiple regression analysis by taking into account only a limited number of alloying elements. Therefore, their applicability to steel compositions differing from the original set of test materials may be questioned.

Table 8 Comparison of the measured stacking fault energies and the stacking fault energies calculated with the compositional equations taken from literature

Steel	Measured γ (mJ/m^2)	Schramm and Reed (1975) (mJ/m^2) *	Rhodes and Thompson (1977) (mJ/m^2) **	Brofman and Ansell (1978) (mJ/m^2) ***
EN 1.4318-1	12.8	6.7	28.0	15.2
EN 1.4318-2	14.7	5.8	21.8	15.3
EN 1.4301	17.8	18.4	29.0	18.4

* $\gamma = -53 + 6.2\%Ni + 0.7\%Cr + 3.2\%Mn + 9.3\%Mo \quad (mJ/m^2)$

** $\gamma = 1.2 + 1.4\%Ni + 0.6\%Cr + 17.7\%Mn - 44.7\%Si \quad (mJ/m^2)$

*** $\gamma = 16.7 + 2.1\%Ni - 0.9\%Cr + 26\%C \quad (mJ/m^2)$

4.5 XRD stress measurements

4.5.1 Results of XRD stress measurements

The tensile stresses measured with the XRD for the austenite and α'-martensite phases and the macroscopic stress measured with the strain gauges are plotted as a function of true plastic strain and α'-martensite volume fraction in Figure 42.

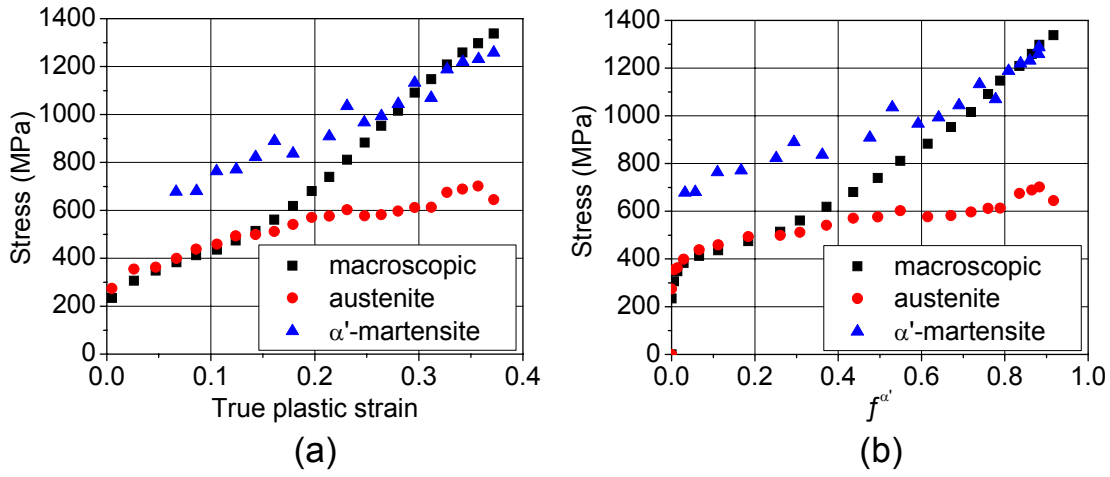

Figure 42 Stress level in austenite and α'-martensite phases measured by XRD and the macroscopic stress measured with strain gauges in EN 1.4318-1 steel as a function of (a) true plastic strain and (b) α'-martensite volume fraction

After each strain increment, the strain gauges indicated significant stress relaxation, of the order of 10% of the applied macroscopic stress. The relaxation was initially rapid, but slowed down in about 60 seconds. Therefore, each XRD stress measurement was started only 60 s after the straining, and the macroscopic stress values shown in Figure 42 are the averages of the macroscopic stress levels recorded in the beginning and at the end of each XRD stress measurement.

The stress analysis results indicated a non-homogeneous distribution of stress between the austenite and α'-martensite phases. The α'-martensite having the higher dislocation density, and thus higher yield strength, showed a higher stress level than the austenite phase. However, the measured stress level in the α'-martensite at low strains was much lower than its yield strength probably was. Narutani (1990) determined the yield strength of α'-martensite as 1480 MPa by pre-straining the test material at 77 K. Therefore, the stress analysis results suggest that the α'-martensite did not deform plastically. Local plastic deformation may, however, have occurred at the stress concentrations, due to, for instance, the irregular shape of the α'-martensite particles.

The stress analysis results support the view of the role of percolation in the stress-strain behaviour of a two-phase aggregate. The stress level in the austenite followed the macroscopic stress up to about $f^{\alpha'}$=0.3, after which the trends deviated from each other. Furthermore, the macroscopic stress and the stress level in the α'-martensite conjoined at $f^{\alpha'}$=0.7. Therefore, the results indicate that the macroscopic stress and the stress level in the matrix phase correlate when the volume fraction of the second phase is below the percolation threshold of 0.3.

4.5.2 Reliability of XRD stress measurements

The XRD stress analysis carried out on a plastically deformed multiphase alloy involves several possible sources of error, which are discussed in the following. In a multiphase aggregate not subjected to an external load, the average of the stresses over the whole body is zero (Noyan and Cohen, 1987):

$$\int_D \sigma_{ij} dD = 0, \tag{51}$$

where D is the volume of the body. In case of an austenite-martensite aggregate under uniaxial tensile stress, the equilibrium condition is, thus, given by:

$$(1 - f^{\alpha'})\sigma_\gamma + f^{\alpha'}\sigma_{\alpha'} = \sigma, \tag{52}$$

where σ_γ is the average stress level in the austenite, $\sigma_{\alpha'}$ is the average stress level in the α'-martensite and σ is the applied (macroscopic) stress. Equation 52 can be used to assess the reliability of the stress measurement results. The stress level calculated according to the equilibrium condition is plotted as a function of strain and compared with the macroscopic stress measured by strain gauges in Figure 43. Deviation of the calculated stress from the measured macroscopic stress is observed. The calculation overestimated the stress level at the low strains and underestimated it at the high strains. One reason for the deviation may be the difference in the extent of stress relaxation in each phase after the straining, as the austenite and α'-martensite phases exhibited

different stress levels. There are also other important sources of error, which are discussed in the following.

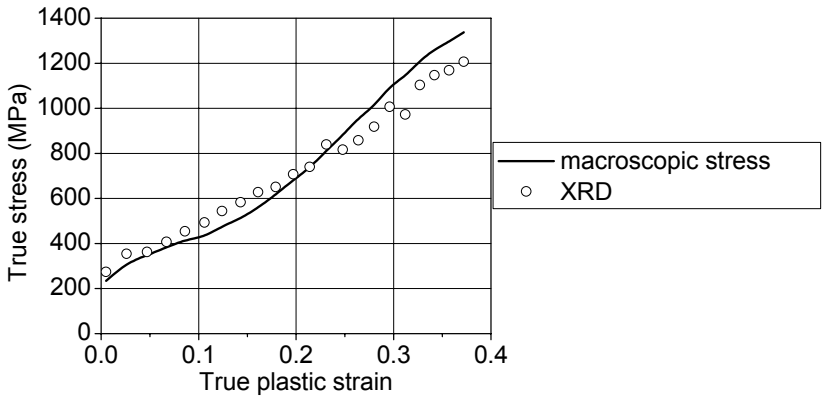

Figure 43 Comparison of the stress calculated by equation 52 by using the XRD stress measurement results and macroscopic stress measured with strain gauges in EN 1.4318-1 steel

Figure 44 shows the examples of the lattice spacing measurements on the austenite and α'-martensite phases, from which the elastic strains and stresses were calculated. Especially the α'-martensite phase showed relatively high deviation from the linear d vs. $\sin^2\psi$ behaviour at high plastic strains.

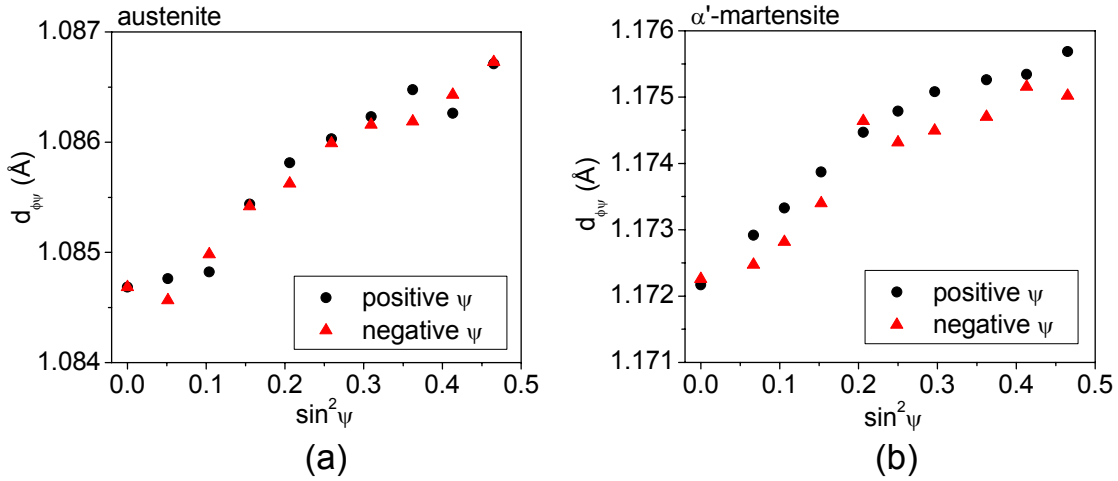

Figure 44 Examples of the $d_{\phi\psi}$ vs. $\sin^2\psi$ plots of (a) austenite and (b) α'-martensite phases of EN 1.4318-1 steel after true plastic strain of 0.35

The deviation from the linearity may be explained in terms of two main reasons: the presence of texture and non-homogeneous stress state. Probably both factors affected the observed behaviour. Texture was certainly present in the highly deformed test material, especially in the strain-induced α'-martensite phase. Furthermore, although the samples were under uniaxial tensile load, the two phase nature of the test material may result in a non-homogeneous stress state. For instance, if a small α'-martensite particle mounted in the austenite is located close to the sample surface, the stress in the $\underline{S}_3$ direction may not be entirely relaxed, resulting in a stress gradient. The irregular morphology of the α'-martensite may also cause stress concentrations in both the austenite and α'-martensite phases. However, both the stress gradients and the texture

are extremely difficult to take into account in the stress analysis (Noyan and Cohen, 1987). Therefore, all data were treated as they were showing linear behaviour. All data showed consistent d values from both negative and positive ψ angles, *i.e.*, the ψ splitting did not occur. This indicates that the shear stress components were absent.

The selection of the XRD elastic constants is a critical step when deriving the stress values from the elastic lattice strains measured with XRD. As described above, in the present work constant values close to the bulk elastic constants were used. However, due to the texture evolution and the relatively high elastic anisotropy of austenitic stainless steels, the XRD elastic constants of the studied phases were certainly affected by the plastic deformation. Unfortunately, this effect is difficult to take into account quantitatively. Some estimation can be performed by considering the extremes of the single crystal elastic constants. For austenitic stainless steels, these are 125 GPa in <100> directions and 273 GPa in <111> directions (Ledbetter, 1984). Although the texture evolution occurs, the XRD elastic constants are believed to remain far from these extreme values.

To summarise, the results of the XRD stress analysis involve error due to the factors discussed above. However, overall the trends in the stress evolution in each phase are believed to be representative, *i.e.*, the α'-martensite phase is subjected to a significantly higher stress than the austenite phase.

4.6 Scanning electron microscopy

The ECC imaging technique proved to be an excellent tool in examining the deformation microstructures of the studied steels. In particular, a clear contrast was obtained from the shear bands formed in the austenite phase during the plastic deformation. Unlike with the TEM, with the ECC imaging it was possible to examine large areas of material in bulk samples. Furthermore, the risk of affecting the microstructural features during the specimen preparation was minimal, since the only specimen preparation necessary was the electropolishing of the sample surfaces. The most important limitation of the technique was that the identification of the phases or the nature of the shear bands was not possible. No attempts were made to study the formation of the α'-martensite phase with the ECC imaging, and the analysis was limited to the detection of the shear bands.

The most distinct feature observed with the ECC imaging was that the occurrence of the shear bands in the deformation microstructures was dependent on the chemical composition, deformation temperature and strain and stress level. Furthermore, a good correlation between the tendencies to shear band and α'-martensite formation was found. In all studied series of samples, the shear bands always appeared before the onset of the α'-martensite transformation.

4.6.1 Deformation microstructures of EN 1.4318-1 and EN 1.4301 steels

The EN 1.4318-1 steel exhibited extensive shear band formation and slip planarity in the austenite phase at both low and high strain rates at room temperature. Figure 45 shows the deformation microstructures formed at the strain rate 3×10^{-4} s^{-1} and Figure 46 the deformation microstructures formed at 200 s^{-1}. Numerous intersecting shear bands

were present even at low strains and stress levels ($\varepsilon<0.05$). It was impossible to see any difference between the samples strained at low and high strain rates.

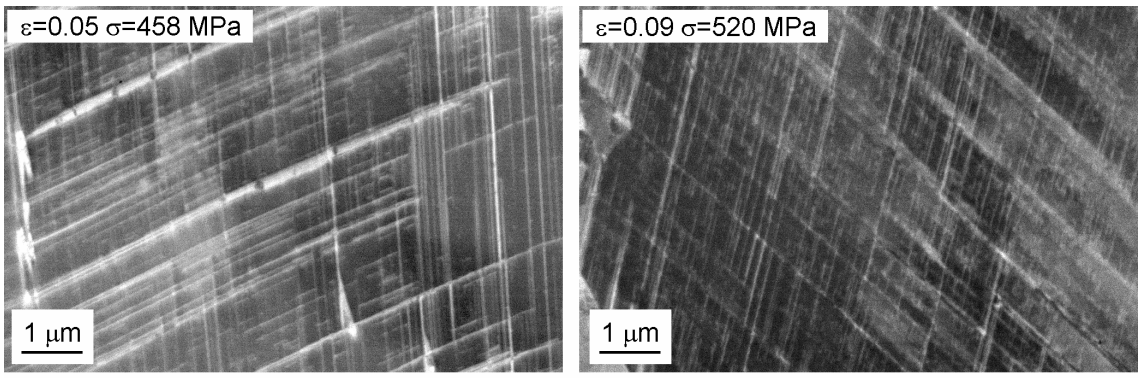

Figure 45 ECC images of deformation microstructures of EN 1.4318-1 steel tensile strained at strain rate 3×10^{-4} s^{-1} at room temperature after true plastic strains of (a) 0.05 and (b) 0.09

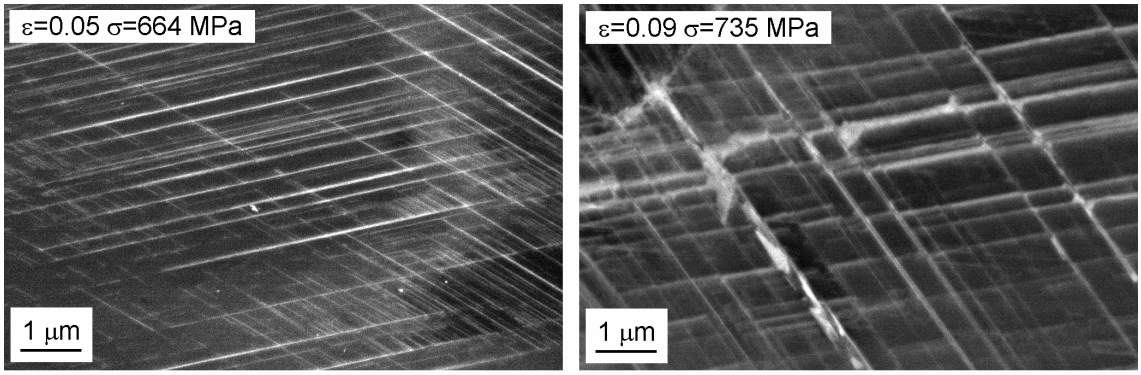

Figure 46 ECC images of deformation microstructures of EN 1.4318-1 steel tensile strained at strain rate 200 s^{-1} at room temperature after true plastic strains of (a) 0.05 and (b) 0.09

In contrast, in the stable EN 1.4301 steel more irregular dislocation structures and only few shear bands occurred at low strains. However, when plastic strain increased, the number of shear bands and shear band intersections increased gradually. The typical features of the EN 1.4301 steel strained at 3×10^{-4} s^{-1} at room temperature are shown in Figure 47. After plastic strain of 0.05, no shear bands extending through the austenite grains could be found, but traces of tangled dislocations and planar defects not extending through the grains were visible (Figure 47a). When the plastic strain increased, initially mainly parallel and later also intersecting shear bands appeared. The shear bands were more sparsely dispersed than in the EN 1.4318-1 steel and also seemed to be thicker.

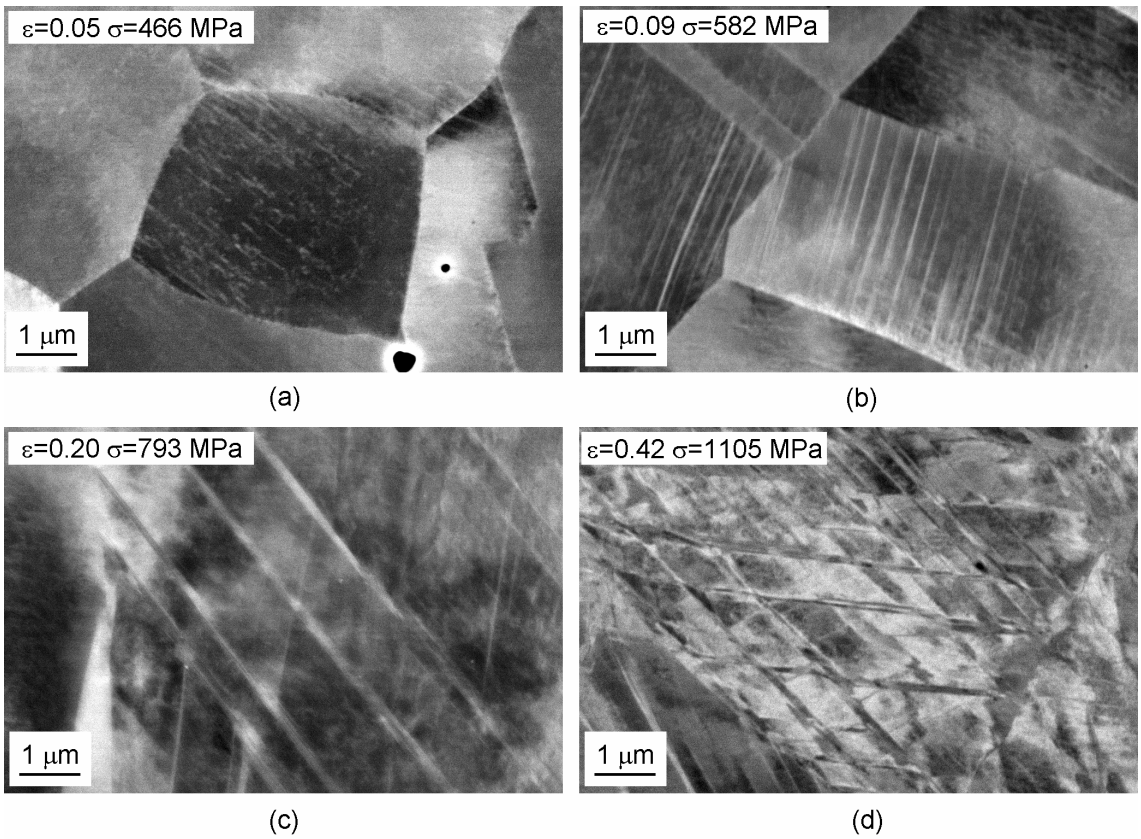

Figure 47 Evolution of the deformation microstructures of EN 1.4301 steel tensile strained at strain rate 3×10^{-4} s^{-1} at room temperature with increasing plastic strain

Figure 48 shows the microstructures of the EN 1.4301 steel strained to true plastic strains of 0.05 and 0.10 at the strain rate 200 s^{-1}. Whereas in the EN 1.4318-1 steel it was difficult to see any effect of the strain rate in the shear band formation, in the EN 1.4301 steel the tendency to the shear band formation seemed to be higher at the high strain rate. This may explain the slightly higher α'-martensite content found at strains below 0.25 (Figure 18b) at the strain rate 200 s^{-1}.

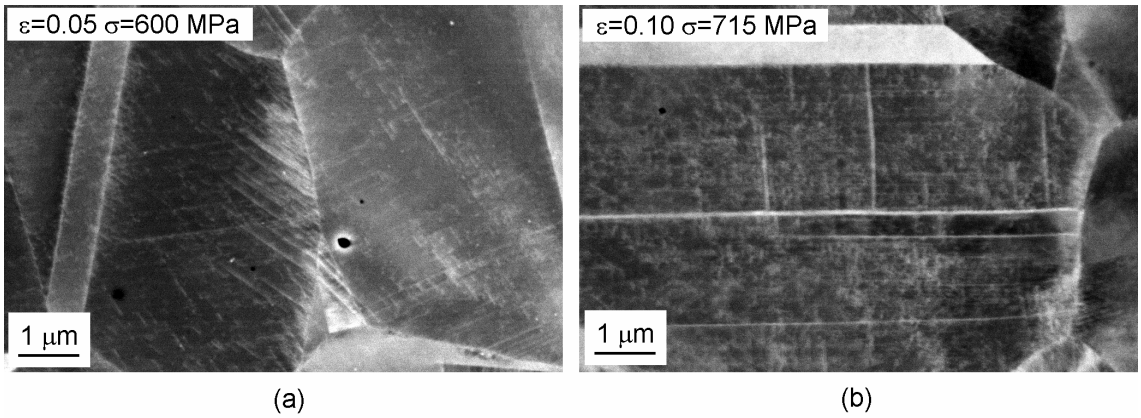

Figure 48 Deformation microstructures of EN 1.4301 steel tensile strained to true plastic strains of (a) 0.05 and (b) 0.10 at strain rate 200 s^{-1} at room temperature

4.6.2 Deformation microstructures of EN 1.4318-2 steel

The deformation temperature and plastic strain were found to have a strong influence on the deformation microstructures of the EN 1.4318-2 steel tensile strained at the strain rate of 3×10^{-4} s^{-1}. The effect of temperature is illustrated in Figure 49, which shows the microstructures formed at different temperatures after plastic strain of 0.05.

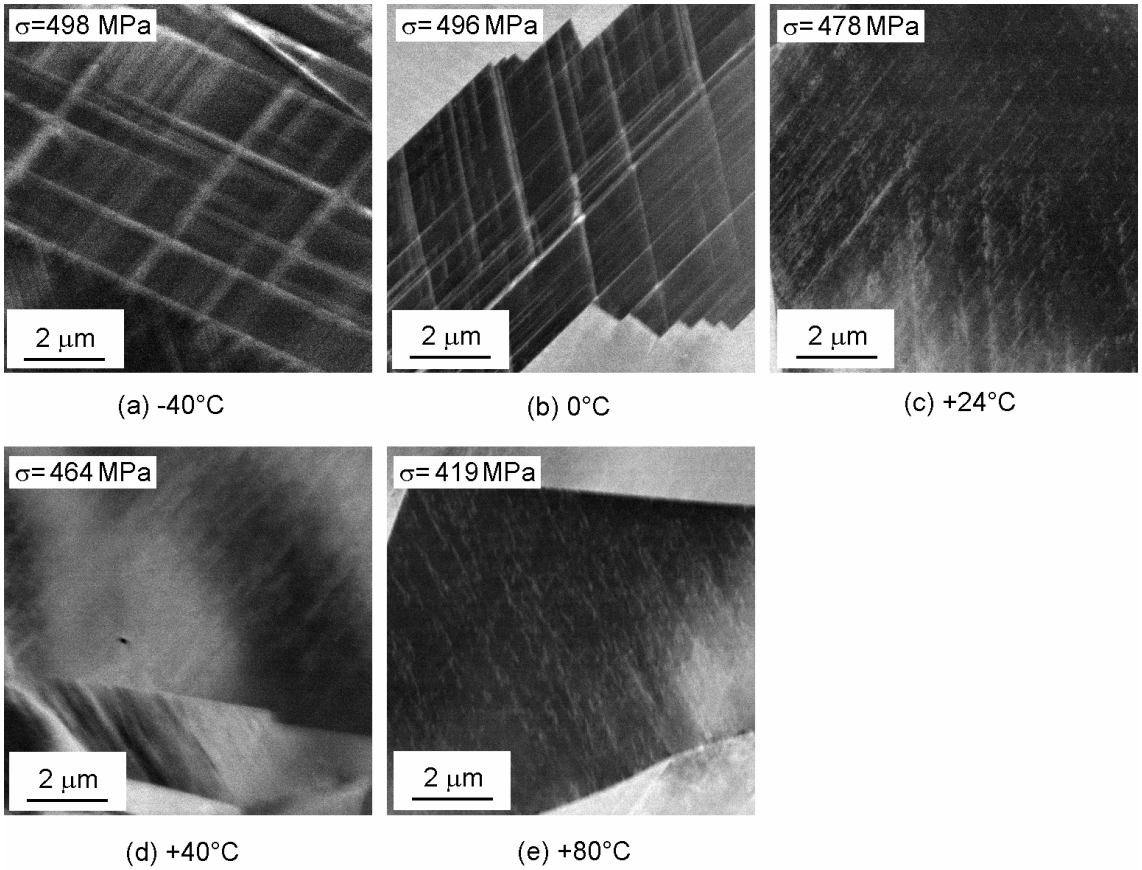

Figure 49 Deformation microstructures of EN 1.4318-2 steel strained to true plastic strain of 0.05 at strain rate 3×10^{-4} s^{-1} at temperatures a) -40°C, b) 0°C, c) +24°C, d) +40°C and e) +80°C

At -40 and 0°C the microstructures were dominated by the shear bands already at the early stages of the deformation, whereas at the higher temperatures no shear bands extending through the austenite grains could be observed. The microstructures were similar to those of the EN 1.4318-1 steel strained at room temperature. At higher temperatures, the microstructures resembled the microstructures of the EN 1.4301 steel strained at room temperature, indicating the presence of the tangled dislocations and narrow planar defects. Furthermore, at high temperatures the shear bands were found to appear after a certain strain and stress level, as in the EN 1.4301 steel. This is illustrated in Figure 50, which shows the evolution of the deformation microstructures in the samples deformed at +80°C to various plastic strains. Well defined shear bands appeared only at strains higher than 0.2. This corresponds well to the onset of the α'-martensite transformation, which took place at about 0.15-0.20 plastic strain (Figure 19).

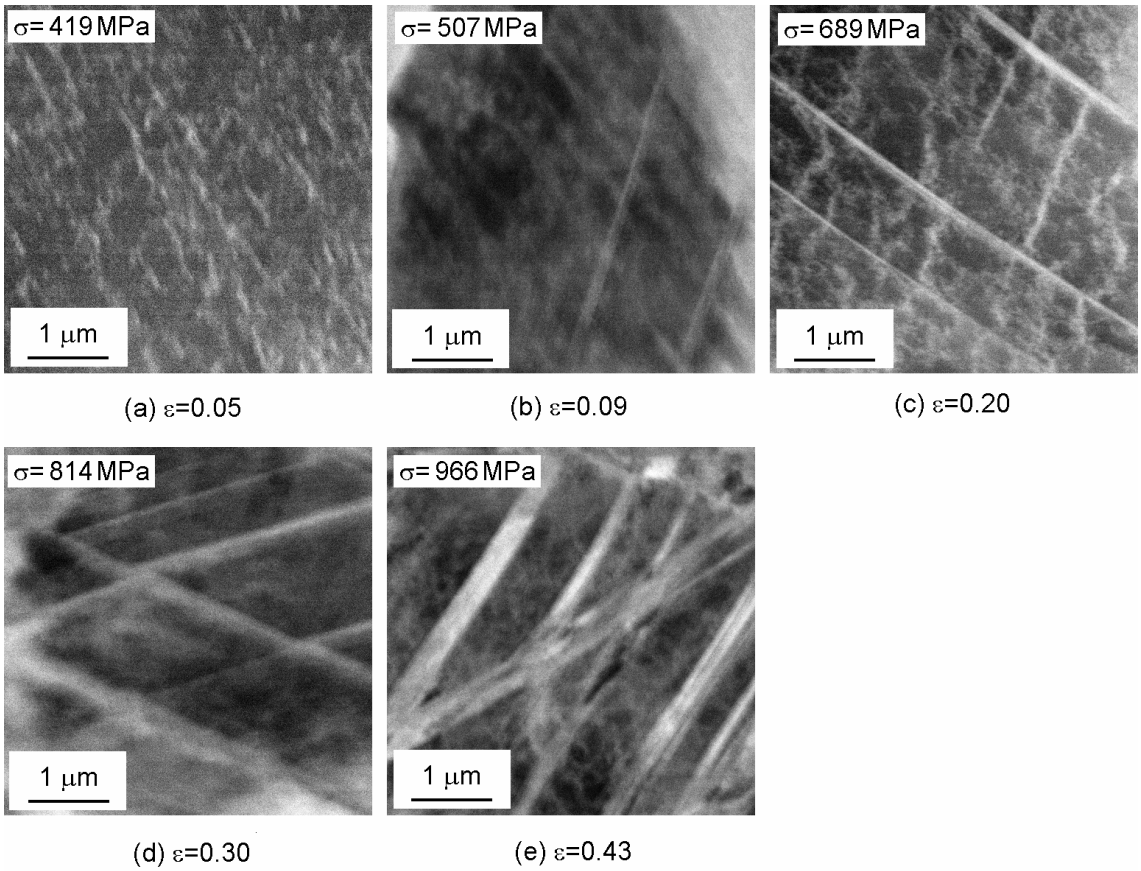

Figure 50 Deformation microstructures of EN 1.4318-2 steel tensile strained to true plastic strains of a) 0.05, b) 0.09, c) 0.20, d) 0.30 and e) 0.43 at strain rate 3×10^{-4} s^{-1} at +80°C

4.7 Transmission electron microscopy

Typical TEM micrographs of the EN 1.4318-1 steel after true plastic strain of 0.05 at the strain rates of 3×10^{-4} and 200 s^{-1} are shown in Figure 51. Higher magnifications from the samples are shown in Figure 52. Figure 53 shows the microstructure of a sample strained to true plastic strain of 0.14 at the low strain rate.

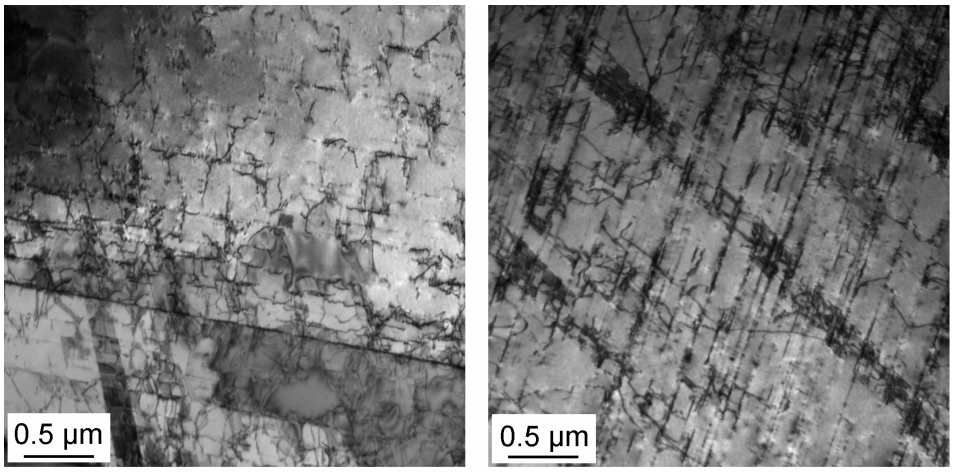

Figure 51 Microstructure of EN 1.4318-1 steel tensile strained to true plastic strain of 0.05 at strain rates (a) 3×10^{-4} and (b) 200 s^{-1} at room temperature

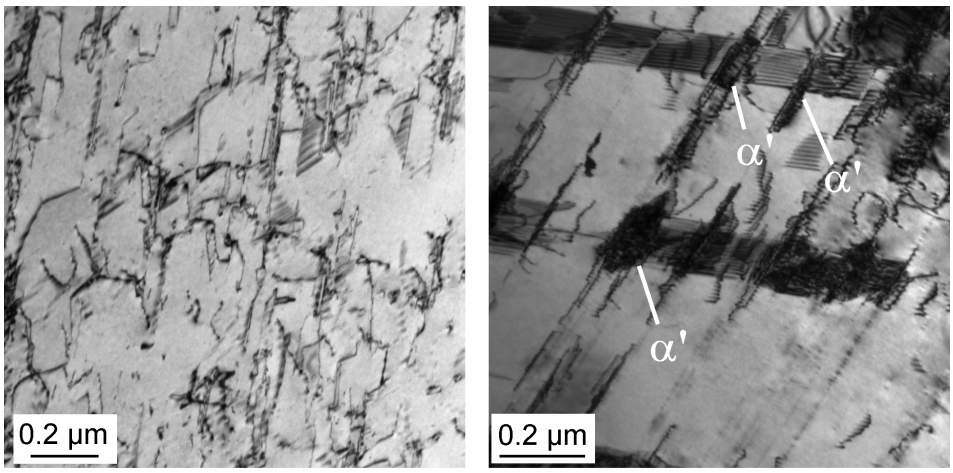

Figure 52 (a) Extended dislocations in EN 1.4318-1 steel tensile strained to true plastic strain of 0.05 at strain rate 3×10^{-4} at room temperature and (b) α'-martensite nucleated at the shear band intersections in EN 1.4318-1 steel tensile strained to true plastic strain of 0.05 at strain rate 200 s^{-1} at room temperature

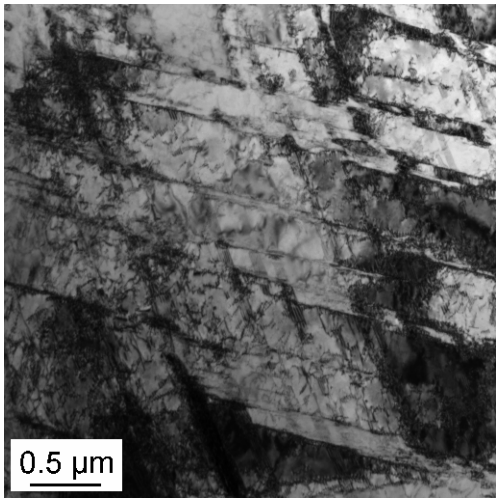

Figure 53 Microstructure of EN 1.4318-1 steel tensile strained to true plastic strain of 0.14 at strain rate 3×10^{-4} s^{-1} at room temperature

The TEM images showed the same features as the ECC images, *i.e.*, the slip planarity and the presence of the shear bands. With TEM it was possible to identify the shear bands as overlapping stacking faults and ε-martensite. No mechanical twins were found. As shown in Figure 52b, the α'-martensite phase nucleated at the intersections of the shear bands. All TEM observations were in accordance with the previous TEM investigations presented in literature.

4.8 Optical metallography

4.8.1 Microstructures

Examples of the optical micrographs of the EN 1.4318-1 steel strained at the strain rate of 3×10^{-4} s^{-1} are shown in Figure 54. A detail of the microstructure shown in Figure 54a is shown in Figure 55. The micrographs were taken from the cross-sections cut parallel to the rolling direction and tensile axis. The α'-martensite phase is etched dark, and the austenite grain boundaries are not etched. The corresponding true plastic strains and α'-martensite volume fractions measured with the Ferritescope are indicated in the figures. The α'-martensite volume fractions were determined also from the micrographs by quantitative image analysis. At low volume fractions, the image analysis indicated higher α'-martensite volume fractions than the Ferritescope, but at the higher fractions a good correlation between the image analysis and the Ferritescope was found.

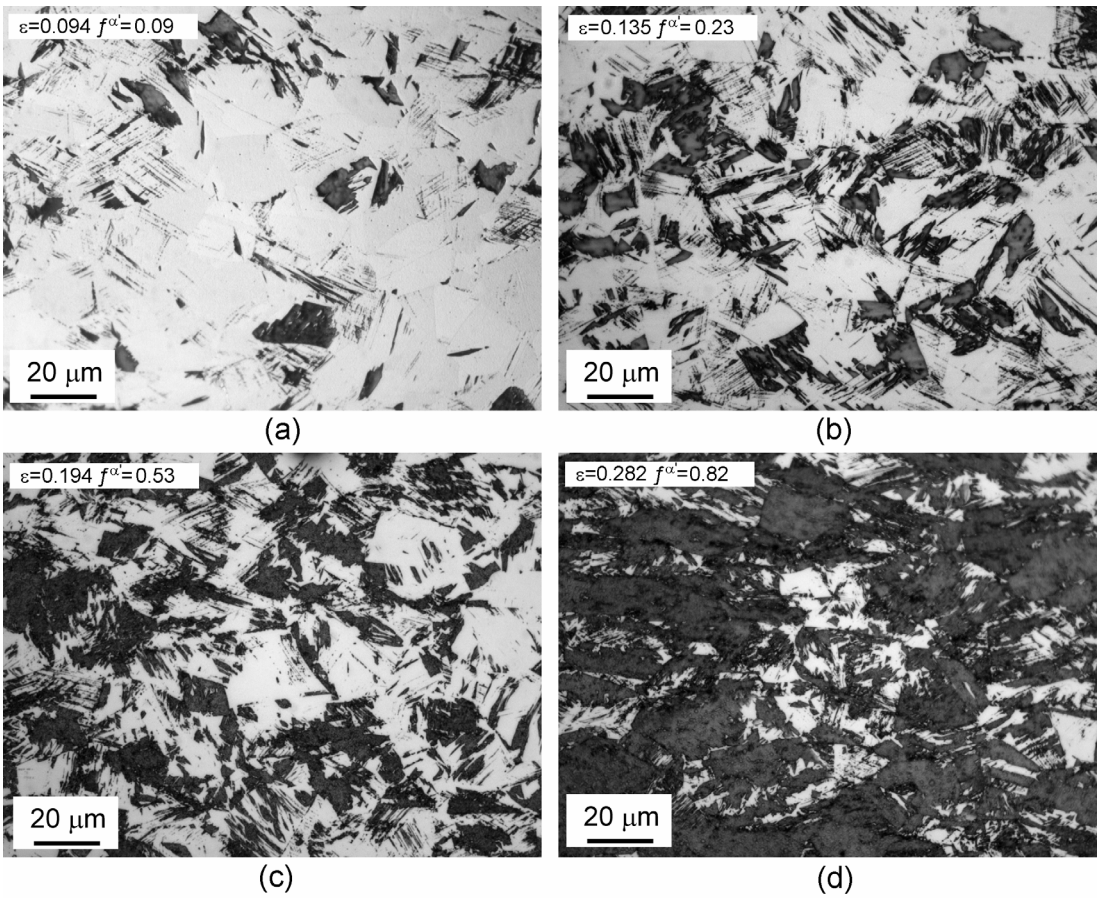

Figure 54 Optical micrographs showing α'-martensite phase etched dark in EN 1.4318-1 steel tensile strained at strain rate 3×10^{-4} s^{-1} at room temperature to true plastic strains of (a) 0.094, (b) 0.135, (c) 0.194 and (d) 0.282

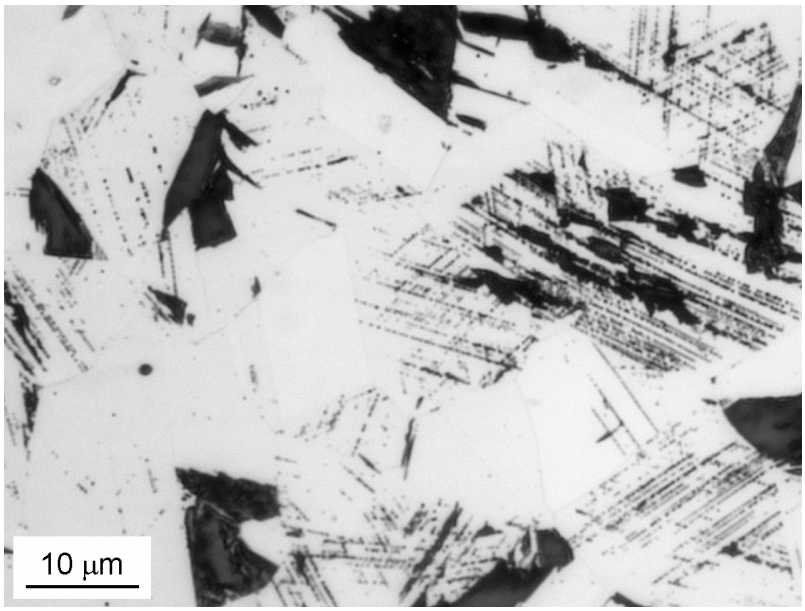

Figure 55 Optical micrograph showing α'-martensite phase etched dark in EN 1.4318-1 steel tensile strained to true plastic strain of 0.094 at strain rate 3×10^{-4} s^{-1} at room temperature

The morphology of the α'-martensite exhibited the well-known features: the nuclei of the α'-martensite were small and located at the intersections of the shear bands, which is well illustrated in Figure 55. However, rather large α'-martensite particles appeared even at low volume fractions, and with increasing $f^{\alpha'}$ irregular blocky structure of α'-martensite was formed. The reliability of the metallographic technique used is difficult to assess. For instance, anisotropic electropolishing and etching may in some instances lead to false indications. However, since a good correlation between the α'-martensite volume fractions measured by the Ferritescope and image analysis was found, the optical micrographs seem to represent the microstructural features well.

4.8.2 Chord length measurements

Figure 56 presents four typical examples of the measured chord length distributions of the α'-martensite phase corresponding to different strain levels and α'-martensite volume fractions. These distributions were measured in the horizontal direction from the samples cut parallel with the rolling direction and tensile axis. The most important features of the distributions are the increasing frequency with decreasing chord length, and the fact that the most distributions showed a maximum between 0.2 and 0.5 μm. This is obviously a consequence of the limited resolution of the optical microscope, which falls in the same range (Vander Voort, 1999). Staudhammer *et al.* (1983) measured the size distribution of the α'-martensite nuclei with TEM, and reported a minimum thickness of 50-70 Å and an average thickness of 250 Å. Therefore, the smallest α'-martensite particles cannot be accurately measured with the optical microscope. The exact effect of this limitation of the optical microscopy on the determination of the size distribution is difficult to estimate. However, since the chord length distributions were broad (*i.e.*, extended to large dimensions), the effect of the limited resolution on the average chord length was believed to be small.

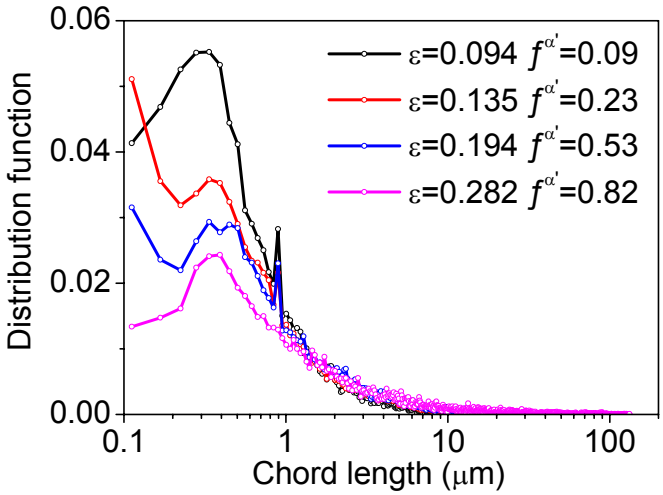

Figure 56 Chord length distribution of α'-martensite particles in EN 1.4318-1 steel tensile strained to various plastic strains at strain rate 3×10^{-4} s^{-1} at room temperature

Average chord lengths of the α'-martensite particles were determined in three directions: parallel and transversally to the tensile axis and also in through-thickness direction. Figure 57 presents the geometric mean of the average chord lengths and the standard deviations of the measurements as a function of the α'-martensite volume fraction. The results indicate that although the α'-martensite nuclei are initially small, relatively large particles or clusters of α'-martensite appeared even at low α'-martensite volume fractions. This is also evident from the micrographs shown in Figures 54 and 55.

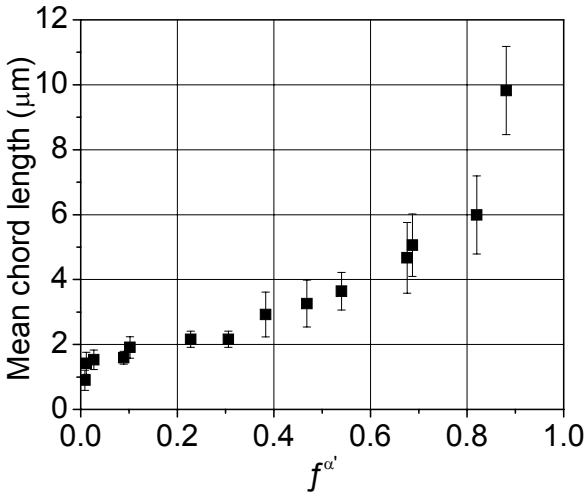

Figure 57 Mean chord length of α'-martensite particles in EN 1.4318-1 steel tensile strained at strain rate 3×10^{-4} s^{-1} at room temperature as a function of α'-martensite volume fraction

4.8.3 Dispersion hardening due to α'-martensite

The chord length measurement results presented above were utilised in the analysis of the dispersion hardening effect of the α'-martensite. According to the XRD line broadening analysis results the dislocation density of the austenite increased with

increasing plastic strain. In contrast, the dislocation density of the α'-martensite was higher and remained relatively unchanged. Furthermore, the XRD stress analysis showed that the α'-martensite exhibited higher flow stress compared to the austenite phase. These features indicate that metastable austenitic stainless steels are plastically non-homogeneous, *i.e.*, the plastic deformation is largely concentrated in the softer austenite phase, and the hard α'-martensite particles cause a dispersion hardening effect. However, there are two fundamental differences between the regular dispersion hardened alloys and the metastable austenitic stainless steels exhibiting the TRIP effect: 1) in the metastable austenitic stainless steels the volume fraction and the size distribution of the dispersions (α'-martensite) change as a function of strain and 2) the phase transformation acts as an alternative deformation mechanism for the slip. Furthermore, the α'-martensite transformation is accompanied by a slight volume increase.

During the plastic deformation of any crystalline material, geometrically necessary dislocations are generated to accommodate the shape change caused by the plastic deformation. When the material contains non-deforming particles (such as α'-martensite), additional dislocations need to be generated in order to preserve the compatibility between the matrix and the dispersions. The generation of the geometrically necessary dislocations was studied by Ashby (1971), who developed a model predicting the amount of the geometrically necessary dislocations as a function of the size and volume fraction of the hard particles and plastic strain. In the present study Ashby's theory was utilised to estimate the dislocation density of the EN 1.4318-1 steel tensile strained at 3×10^{-4} s^{-1} by using the chord length measurement results presented above as the input data. Since Ashby considered only alloys having a constant fraction of particles of a constant size, the original theory was modified to take into account the changes in the α'-martensite volume fraction and the particle size. Furthermore, the α'-martensite particles were assumed to have cubic shape and instead of shear deformation discussed by Ashby uniaxial tension was considered.

The α'-martensite particles within the austenitic matrix are assumed to be located at holes with the volume of L^3. If the material is plastically deformed by the strain increment $\Delta\varepsilon$, the volume of each hole is increased by $\Delta\varepsilon L^3$. If the α'-martensite particles are not plastically deformed, and the elastic strains are neglected, to maintain the compatibility between the phases the volume increase of the holes must be filled by the plastic deformation of the softer austenite phase. This can occur by the generation of the prismatic dislocation loops, as indicated in Figure 58. Each dislocation can fill the volume of bL^2, and thus the number of dislocation loops per particle is given by:

$$n^T = \frac{L\Delta\varepsilon}{b}, \tag{53}$$

where b is Burgers vector of a dislocation loop. In reality, the accommodation may partially occur due to the α'-martensite transformation strain, due to the volume change related to the transformation or by the plastic deformation of the α'-martensite, but for simplicity, these effects were neglected here.

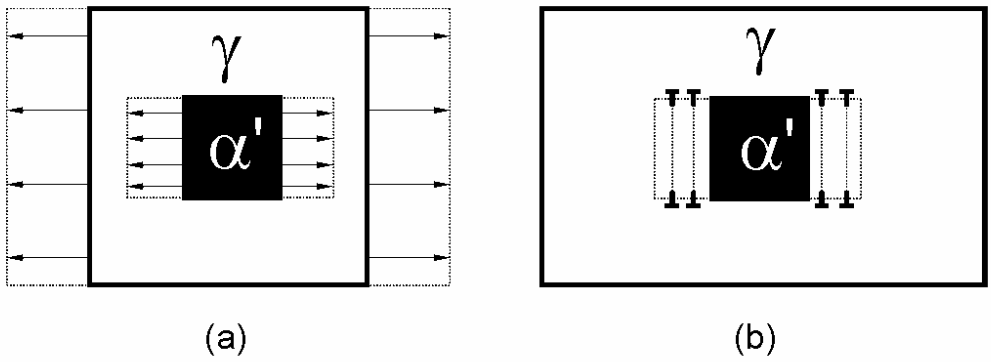

Figure 58 Schematic illustration of the plastic deformation of plastically non-homogeneous austenite-martensite mixture: a) the austenitic matrix (white square) is deformed, whereas the martensite (dark square) remains in the original shape and b) the formation of the prismatic dislocation loops to accommodate the plastic deformation of the austenitic matrix

When the volume fraction and size of the α'-martensite particles are known, the number of particles per unit volume is given by:

$$N_v = \frac{f^{\alpha'}}{L^3}. \tag{54}$$

The loop density N^T (the number of dislocation loops per unit volume) is obtained by multiplying n^T and N_v:

$$N^T = n^T N_v = \frac{f^{\alpha'}\Delta\varepsilon}{bL^2}. \tag{55}$$

The length of each dislocation loop surrounding the α'-martensite particle is 4L (at least). Therefore, the increase in the density of the geometrically necessary dislocations $\Delta\rho_G$ per strain increment $\Delta\varepsilon$ is:

$$\Delta\rho_G = \frac{4f^{\alpha'}\Delta\varepsilon}{bL}. \tag{56}$$

The density of the geometrically necessary dislocations was calculated using the chord lengths of α'-martensite in the EN 1.4318-1 steel strained at 3×10^{-4} s^{-1} presented in Figure 57. For simplicity, the Burgers vector of a perfect dislocation b=2.5 Å was used in the calculation, and the formation of the partial dislocations, stacking faults and ε-martensite was ignored. The square root of the calculated dislocation density is plotted as a function of the flow stress in Figure 59 (red dots), and compared with the XRD measurement results (black squares). A fairly good correlation between the measured and calculated dislocation densities was found, but the calculated dislocation density was consistently lower than the measured dislocation density. This was obviously because the onset of the α'-martensite transformation occurred only after about 0.05 plastic strain, corresponding to the flow stress of 400 MPa. Rapid dislocation multiplication takes place at the early stages of the deformation, and this initial dislocation density generated before the onset of the transformation was not taken into

account in the calculation. From the XRD results presented in Figure 59 (as well as from Figures 38 and 39), the dislocation density of the austenite at the 400 MPa stress level is found to be about 2.5×10^{13} m^{-2} for both EN 1.4318-1 and EN 1.4301 steels. By adding this initial dislocation density ρ_0 to the calculated ρ_G, the values indicated by the blue triangles shown in Figure 59 were obtained. These results showed an excellent correlation with the dislocation densities measured by XRD.

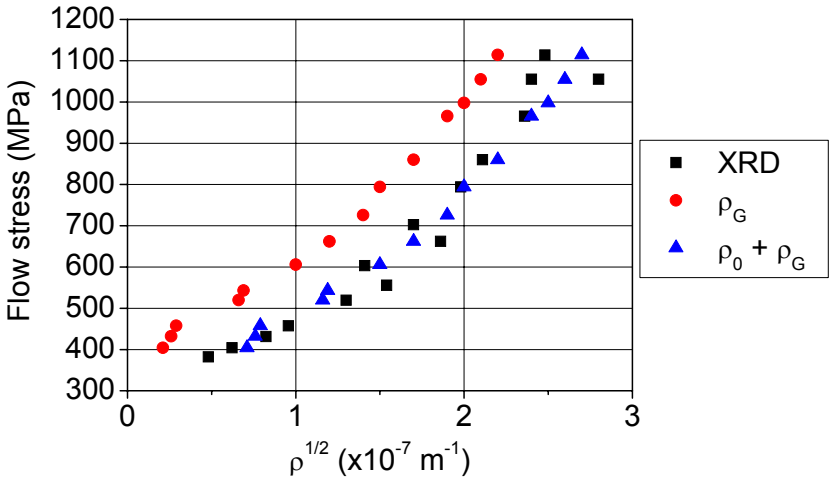

Figure 59 Square root of dislocation density of austenite phase in EN 1.4318-1 steel tensile strained at strain rate 3×10^{-4} s^{-1} at room temperature calculated by using equation 56 and comparison with experimental results presented in Figure 31

A surprising feature of the results shown in Figure 59 is that the correlation between the calculated and measured dislocation densities remained good even at high α'-martensite volume fractions, where the microstructure in fact consists of austenite islands embedded in the α'-martensite matrix. This condition can be analysed by Figure 60. When the aggregate having the high α'-martensite volume fraction deforms plastically, the α'-martensite matrix must deform. Since the austenite islands have a lower dislocation density and yield strength, they co-deform with the matrix. The accommodation of the austenite particles occurs by the generation of dislocation loops, as illustrated in Figure 60.

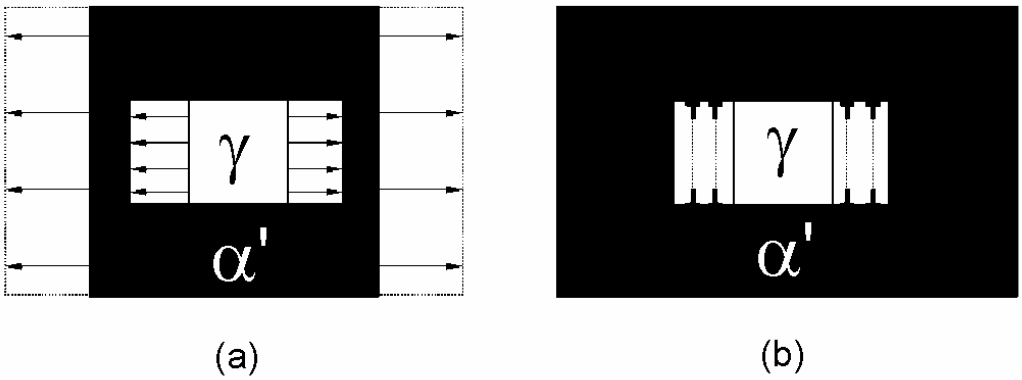

Figure 60 Schematic illustration of the formation of geometrically necessary dislocations at high α'-martensite volume fractions: (a) an austenite particle within the α'-martensite matrix and (b) plastic deformation and formation of the dislocation loops

The density of these dislocations may be calculated equivalently with the treatment presented above. However, instead of considering the particle size of α'-martensite, the particle size of austenite is needed for the calculation. In a two-phase system, the matrix chord length λ^L, *i.e.*, the distance between the particles having the size of L, is given by (Underwood, 1985):

$$\lambda^L = L\frac{1-f^{\alpha'}}{f^{\alpha'}}. \tag{57}$$

Obviously, the matrix chord length of the α'-martensite corresponds to the chord length of austenite. Therefore, the density of the geometrically necessary dislocations can be re-calculated for the situation shown in Figure 60. The number of dislocation loops per austenite particle is given by:

$$n^T = \frac{\lambda^L \Delta\varepsilon}{b}. \tag{58}$$

The number of austenite particles per unit volume is:

$$N_v = \frac{1-f^{\alpha'}}{(\lambda^L)^3}, \tag{59}$$

and the density of the loops per unit volume:

$$N^T = n^T N_V = \frac{(1-f^{\alpha'})\Delta\varepsilon}{(\lambda^L)^2 b}. \tag{60}$$

Each dislocation loop has the length of $4\lambda^L$. Therefore, the increase in the dislocation density per strain increment $\Delta\varepsilon$ is:

$$\Delta\rho_G = \frac{4(1-f^{\alpha'})\Delta\varepsilon}{\lambda^L b}. \tag{61}$$

By combining equations 57 and 61, the following result is obtained:

$$\Delta\rho_G = \frac{4f^{\alpha'}\Delta\varepsilon}{Lb}, \tag{62}$$

which appears to be equivalent with equation 56. Therefore, the density of the geometrically necessary dislocations in the austenite phase can be calculated based on the particle size and volume fraction of the α'-martensite phase even at high α'-martensite volume fractions. However, although the model predicted the dislocation density of the austenite phase correctly, this does not mean that it can predict the dispersion strengthening effect of the α'-martensite correctly. The upper limit for the validity of the modified Ashby's model is probably associated to the percolation threshold of the α'-martensite. As soon as the α'-martensite phase percolates, it starts to have a direct contribution to the flow stress. Consequently, the stress needed to deform

the aggregate is no longer dependent only on the dislocation density of the austenite, but also the α'-martensite must deform in order to accommodate the shape change.

4.8.4 Clustering of α'-martensite phase

The presence of percolating clusters of the α'-martensite phase was examined in a total of 26 samples (13 parallel to the tensile axis and 13 in the transverse direction) of the EN 1.4318-1 steel strained at 3×10^{-4} s^{-1} at room temperature. From each sample five micrographs were taken from arbitrary locations and analysed using the MATLAB routine. Examples of the analysed micrographs with different $f^{\alpha'}$ are shown in Figure 61. Each cluster of α'-martensite was identified and coloured with an arbitrarily selected colour. Corresponding α'-martensite volume fractions determined by the image analysis are indicated in the figures.

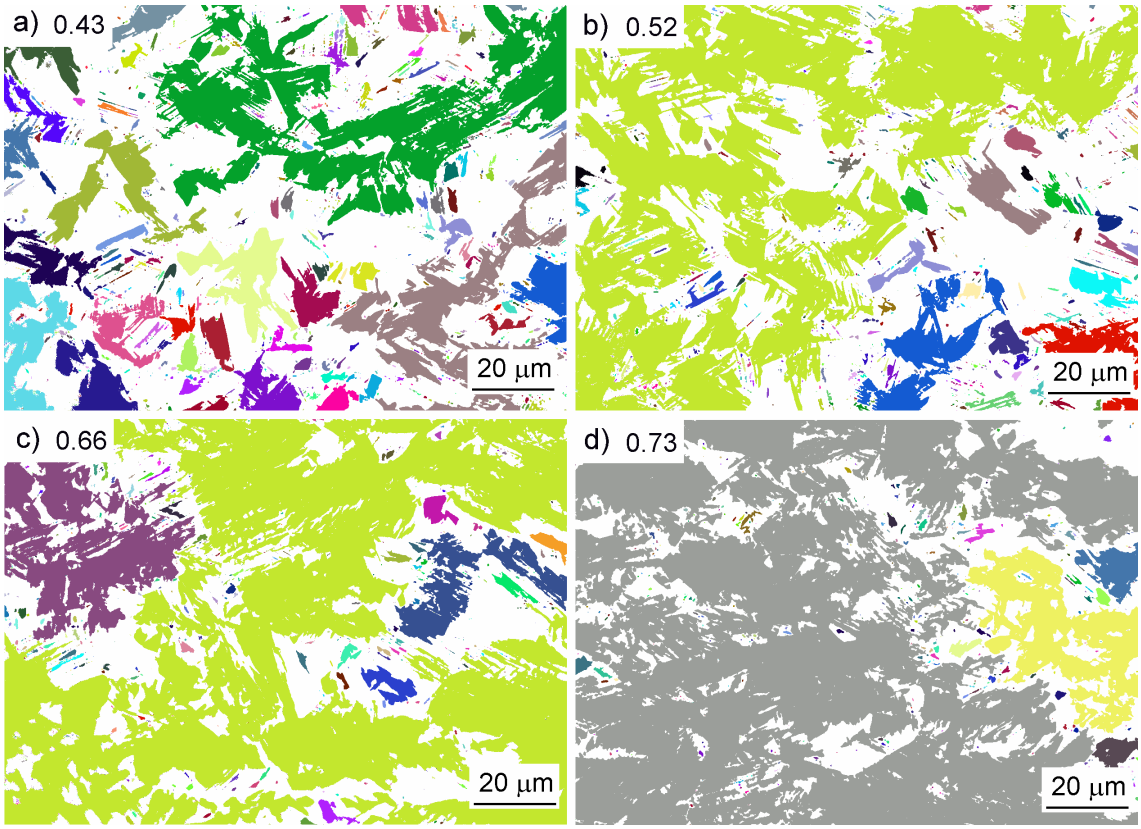

Figure 61 Clustering of α'-martensite phase in EN 1.4318-1 steel strained at strain rate 3×10^{-4} s^{-1} at room temperature with α'-martensite volume fractions of a) 0.43, b) 0.52, c) 0.66 and d) 0.73

The micrographs shown in Figure 61 illustrate how the percolating clusters of α'-martensite were formed with increasing $f^{\alpha'}$. Figure 62 summarises the presence of percolating α'-martensite clusters in all analysed micrographs as a function of α'-martensite volume fraction. According to the results, the α'-martensite formed a percolating cluster in the tensile direction first when $f^{\alpha'}$=0.5. The highest volume fraction where the percolation did not occur was about 0.6. In the vertical direction, a percolating cluster existed first time at $f^{\alpha'}$=0.44 and the highest $f^{\alpha'}$ where the percolation did not occur was 0.65. A similar behaviour was found in the micrographs taken

transverse to the tensile axis, but the percolation occurred at slightly lower α'-martensite volume fractions. However, taking into account the rather small number and the limited size of the analysed images, the results were rather consistent. The percolation threshold was, therefore, close to $f^{\alpha'}$=0.6, which correlates well with the theoretical percolation threshold of 0.593 for a statistically distributed two-dimensional square lattice (Stauffer and Aharony, 1994). Analogously, in a three-dimensional cubic lattice the theoretical percolation threshold value is 0.312, which was found to be the critical volume fraction, at which the strengthening contribution of the α'-martensite phase was found to become stronger. Unfortunately, it is impossible to carry out 3D percolation analysis on the real samples. However, it is believed that due to the good correlation between the theoretical and experimental results in the 2D case, the correlation exists also in 3D case.

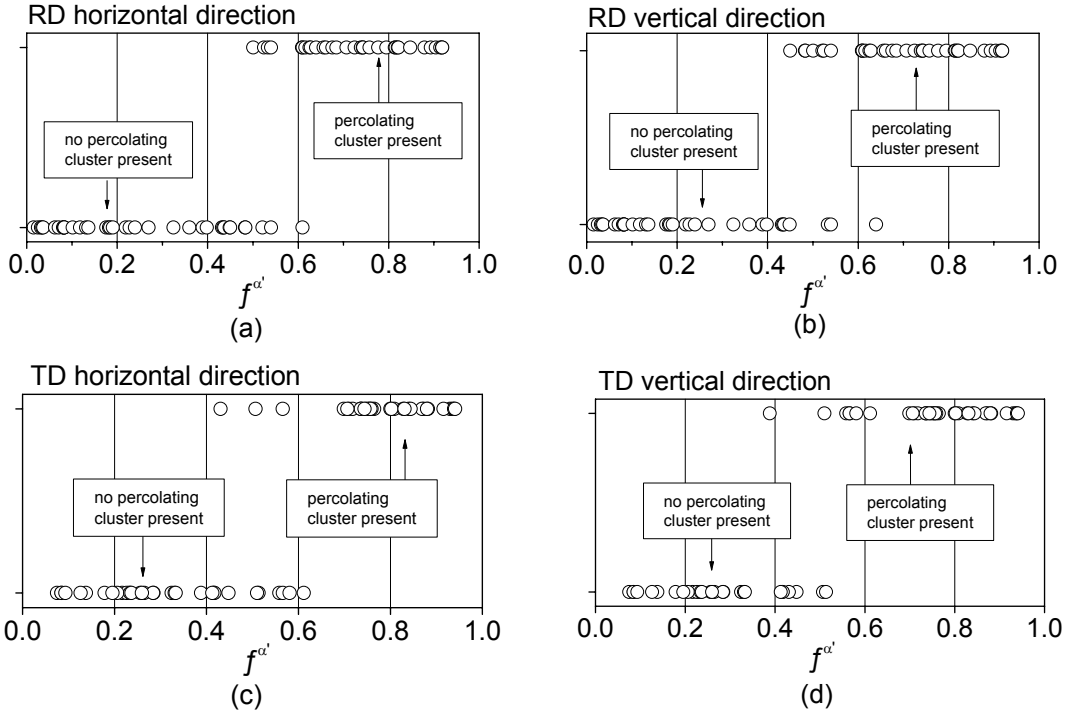

Figure 62 Occurrence of percolating α'-martensite clusters in (a) horizontal and (b) vertical directions in micrographs taken parallel with rolling direction and tensile axis (RD) and in (c) horizontal and (d) vertical directions in micrographs taken transverse to rolling direction and tensile axis (TD) of EN 1.4318-1 steel tensile strained at strain rate 3×10^{-4} s^{-1} at room temperature

The occurrence of the percolating clusters at the α'-martensite volume fractions below the percolation threshold is a consequence of two factors: when the percolating phase is statistically distributed, there obviously exists a probability greater than zero that the phase percolates at a volume fraction below the threshold value. Furthermore, the analysed sampling areas had only a limited size, far from infinite or even from the size of the samples. The width of the micrographs was 143 μm, which is more than three orders of magnitude less than the size of the tensile test samples. Therefore, the percolating clusters occurred at lower $f^{\alpha'}$ than would be the case in a larger volume. However, these features are probably not significant, since the results indicated that the percolation of the α'-martensite did not deviate significantly from the theoretical values.

5 DISCUSSION

5.1 Microstructural evolution

The comparison between the ECC imaging results and the measured α'-martensite volume fractions showed that the appearance of the shear bands always preceded the onset of the α'-martensite transformation. This is in a good agreement with the literature suggesting that the nucleation of the α'-martensite occurs only at the shear band intersections. This view was also supported by the TEM findings. Furthermore, the appearance of the shear bands and the onset of the α'-martensite transformation exhibited similar dependence on the chemical composition, deformation temperature, stress and strain, indicating a close relation between these events.

5.1.1 Formation of shear bands

The ECC imaging results indicated that the extent of shear band formation was essentially dependent on the chemical composition, strain and stress level, temperature and strain rate: in the EN 1.4318-1 steel tested at room temperature and in the EN 1.4318-2 steel tested at low temperatures, numerous shear bands appeared at even the very beginning of the plastic deformation. In contrast, in the EN 1.4301 steel tensile strained at room temperature and in the EN 1.4318-2 steel strained at higher temperatures the shear bands could be observed only after a certain strain and stress level. It is well known that the formation of the shear bands is closely related to the SFE. As the SFE is dependent on chemical composition and temperature, the observed variation in the shear band formation may be attributed to the compositional and temperature dependence of the SFE. Recently, also the influence of the applied stress on the stacking faults has been discussed (Byun, 2003). Here, Byun's model (equation 10) was used in order to explain the shear band formation.

The analysis was based on the hypothesis that the appearance of the shear bands extending through the austenite grains, observed by the ECC imaging, corresponds to the situation where the stacking faults become unstable and diverge due to the applied stress, as predicted by Byun's model. Thus, even a single wide stacking fault was regarded as a shear band, and the overlapping process of the stacking faults was not considered. By using the SFEs determined by the XRD (Table 7) as input values, the curves presented in Figures 63 and 64 showing the stacking fault width as a function of external tensile stress were obtained. Figure 63 shows the calculation results for the EN 1.4318-1 and EN 1.4301 steels at room temperature. Figure 64 illustrates the effect of temperature on the stress-dependence of the stacking fault width in the EN 1.4318-2 steel. The influence of temperature on the SFEs was taken into account by using the temperature coefficient of 0.1 mJ/m^2K, typical of the austenitic stainless steels of low alloy content as shown in Table 1. The curves were calculated by using the highest possible Schmid factor of 0.5. The angles θ_1 and θ_2 were assumed to be -30° and 30°, respectively, corresponding to a perfect screw dislocation possessing the highest possible stress effect. Hence, the results shown in Figures 63 and 64 represent the width of the stacking faults in the most favourably oriented slip systems, and the stresses correspond to the lowest stress level at which the shear bands extending through the austenite grains should appear. The results predicted that the diverging of the stacking faults occurred in all cases at a stress level between 200 and 600 MPa. Following the

hypothesis made above, the shear bands extending through the austenite grains should appear only in the samples that were stressed above the critical stress levels. This may be assessed by examining the ECC images presented in section 4.6.

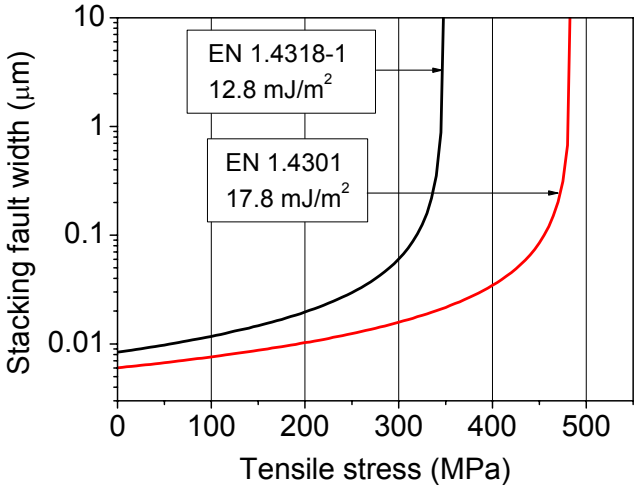

Figure 63 Calculated stacking fault width as a function of applied tensile stress in EN 1.4318-1 and EN 1.4301 steels at room temperature

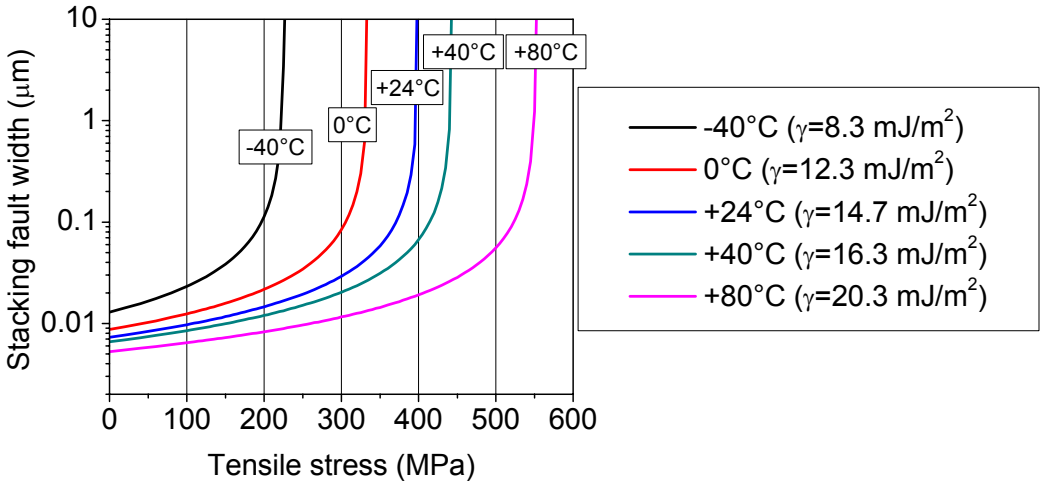

Figure 64 Calculated stacking fault width as a function of applied tensile stress in EN 1.4318-2 steel at various temperatures

Numerous densely spaced intersecting shear bands appeared in all studied tensile strained EN 1.4318-1 steel samples (Figures 45 and 46). Accordingly, the flow stress was in all cases higher than the calculated critical stress of about 350 MPa. With the EN 1.4301 steel, the formation of shear bands was clearly dependent on the plastic strain and flow stress. No shear bands were present after the plastic strain of 0.05 (Figure 47a). At this strain, the corresponding flow stress was 466 MPa, *i.e.*, below the calculated critical stress of 480 MPa. At the plastic strain of 0.09, corresponding to the flow stress of 582 MPa exceeding the critical value, the SEM examination showed that shear bands were present in some grains (Figure 47b). Furthermore, at the higher strains and flow stresses (Figures 47c and d), the number of shear bands increased, and also intersecting shear bands appeared, indicating the activation of the slip systems of lower Schmid factors.

The effect of stress on the shear band formation could be observed also when comparing samples of the EN 1.4301 steel deformed at different strain rates, as the flow stress increased with increasing strain rate. Whereas after 0.05 plastic strain at 3×10^{-4} s^{-1} no shear bands were present, after the same amount of plastic deformation at 200 s^{-1} shear bands appeared in the microstructure (Figure 48a). Since the flow stress corresponding to 0.05 true plastic strain at 3×10^{-4} s^{-1} was 466 MPa and at 200 s^{-1} 600 MPa, it seems that the high strain rate promoted the shear band formation by increasing the flow stress.

An excellent correlation between the calculations and the observed microstructures was found also for the EN 1.4318-2 steel strained at different temperatures. As shown in Figure 49, at the true plastic strain of 0.05 well-defined shear bands appeared only at -40 and 0°C. In these cases the corresponding flow stresses were 498 and 496 MPa, respectively. Comparison with the calculation results presented in Figure 64 reveals that the flow stresses were significantly higher than the calculated critical stresses for stacking fault instability at these temperatures. At +24 and +40°C the calculated stresses and flow stresses were close to each other. Consequently, only weak traces of the shear bands could be seen. At +80°C the calculated stress (550 MPa) was substantially higher than the flow stress (419 MPa). Correspondingly, no shear bands were observed.

The deformation microstructures of the EN 1.4318-2 steel deformed at +80°C to several strain levels were shown in Figure 50. At +80°C the calculated critical stress for the instability of the stacking faults was about 550 MPa, corresponding to the true strain of 0.12. Again, an excellent correlation between the calculation and observed microstructures was found. The shear bands appeared only at strain levels higher than 0.2, whereas at the strains of 0.05 and 0.09 no shear bands could be observed.

The stress acting on the partial dislocations is affected not only by the orientation of the slip system. Also local stress concentrations are present in the microstructure, which may be caused by, for instance, grain boundaries, dislocation pile-ups and annealing twins. The presence of the stress concentrations may cause deviation from the behaviour predicted by the above analysis. Furthermore, the XRD measurements, as well as the estimation of the effect of temperature on the SFE, involve uncertainty. However, as the significant number of the samples studied exhibited consistent behaviour, the results seem to be representative. Furthermore, the ECC imaging technique enabled to study large areas of the samples, which allowed obtaining a representative picture of the deformation microstructures.

5.1.2 Structure of shear bands

The above discussion considered only the behaviour of single extended dislocations and stacking faults. Therefore, it is unable to explain the overlapping process of the stacking faults, which is obviously essential in terms of the generation of the nucleation sites for the α'-martensite. Furthermore, with the ECC imaging it was not possible to distinguish between the stacking fault bundles, ε-martensite and the mechanical twins, which is an important limitation. However, the X-ray diffraction measurements indicated that the ε-martensite formation was favoured by low alloying and low temperature, both decreasing the stacking fault energy of the steel. Therefore, the results demonstrate that the low SFE promotes the overlapping of the stacking faults on every second {111} plane, resulting in the formation of more perfect ε-martensite phase. The role of the SFE can be rationalised by equation 6, which divides the SFE in surface and volume energy

components. The surface energy term has been estimated as about 20 mJ/m^2 (Olson and Cohen, 1976b; Miodownik, 1978), which is more than the measured SFEs of the studied steels. Therefore, if the strain energy contribution is neglected, the chemical free-energy difference between the FCC and HCP phases $\Delta G^{\gamma\rightarrow\varepsilon}$ was negative for all the studied steels, the EN 1.4318-2 steel at +80°C being an exception with SFE=20.3 mJ/m^2. As the HCP phase is thermodynamically more stable than the austenite, the stacking faults tend to overlap on every second {111} plane in order to form perfect ε-martensite and minimise the surface energy of the faults. Therefore, the higher chemical driving force was available (*i.e.*, the lower was the SFE), the more perfect ε-martensite was formed. It is, however, noteworthy that the ε-martensite reflections were in all cases very broad, even much broader than the 110 reflections of the α'-martensite located at almost equal 2θ angles (Figure 26). This indicates that the ε-martensite was very highly faulted and finely dispersed.

The TEM investigation limited only to the EN 1.4318-1 steel did not reveal the presence of mechanical twins, and the other experimental techniques used were unable to distinguish the twinning. However, twinning probably did not occur in the present experiments. The tendency to the mechanical twinning may be assessed by equation 12. If we assume that (see explanations for the input data in section 1.2.5) $\gamma_0=2\sigma(n)=20$ mJ/m^2, x=0.5 (Lecroisey and Pineau, 1972), G=77.4 GPa, b=1.47 Å and ξ=0.01 (Olson and Cohen, 1976b), the twinning should occur only when the SFE is higher than about 30 mJ/m^2 within the stress range relevant to the studied steels. As the measured SFEs of the test materials were significantly lower than 30 mJ/m^2, it is reasonable to conclude that the twins were not observed, and the shear bands found by ECC imaging consist mainly of bundles of overlapping stacking faults and ε-martensite.

5.1.3 Formation of strain-induced α'-martensite

It is well established that in austenitic stainless steels the shear band intersections act as the nucleation sites of the α'-martensite phase. The results of the present study supported the view that the formation of the shear bands and α'-martensite are directly interlinked, since the presence of the shear bands always preceded the formation of the α'-martensite. Also the optical and electron microscopy studies demonstrated that the α'-martensite nucleated at the shear band intersections. Therefore, it is reasonable to compare the stress-dependence of the stacking fault width (Figures 63 and 64) and the stress-dependence of the α'-martensite transformation, presented in Figures 22 and 23. For all steels and deformation temperatures, there was a certain stress level above which the strain-induced α'-martensite transformation occurred. Obviously, the stress level corresponding to the onset of the α'-martensite transformation was higher than the stress level at which the shear bands appeared in the most favourably oriented slip system. However, qualitatively the dependencies were equivalent.

According to the α'-martensite nucleation mechanisms suggested by Olson and Cohen (1972; 1976b), Lecroisey and Pineau (1972), Suzuki *et al.* (1977) and Brooks *et al.* (1979a; 1979b), the necessary condition for the α'-martensite nucleation is the formation of a shear band on one austenite {111} plane, and the activation of the other intersecting austenite {111}<110> slip system. Furthermore, dissociation of the perfect dislocations and significant piling-up of the Shockley partial dislocations is necessary before the partial dislocations can penetrate through the shear band. Consequently, it is

evident that a higher stress is needed for the nucleation of the α'-martensite compared to the formation of the shear bands. However, quantitative estimation of the stress level is difficult.

In the tests carried out at the lowest strain rate, the maximum transformation rate occurred consistently at $f^{\alpha'}$=0.3. Apparently, this feature is related to the decreasing volume fraction of the austenite phase, which leads to the reduction in the volume fraction of the nucleation sites against the volume of the aggregate. Unfortunately, accurate and representative quantification of the shear bands is impossible. However, the dislocation density measurement results of the austenite phase should at least qualitatively reflect the number of shear bands and shear band intersections, as the presence of the stacking faults and dislocations is directly interlinked (the stacking faults are a result from the dissociation of the perfect dislocations). Figure 65 shows the dislocation density of the austenite per unit volume of the aggregate ρ_{AGG}, defined as:

$$\rho_{AGG} = \rho(1 - f^{\alpha'}), \tag{63}$$

determined by the IBM as a function of α'-martensite volume fraction in the EN 1.4318-1 and EN 1.4318-2 steels tensile strained at 3×10^{-4} s^{-1}. Although the dislocation density per unit volume of the austenite kept increasing with increasing plastic strain and $f^{\alpha'}$ (Figure 30), the plots shown in Figure 65 clearly demonstrate that ρ_{AGG} decreased at higher α'-martensite volume fractions. Due to the limited number of data points the exact locations of the maxima in the ρ_{AGG}-$f^{\alpha'}$ plots were difficult to define. However, the maxima seemed to be located at about $f^{\alpha'}$=0.3-0.4, thus, corresponding well with the location of the transformation rate maxima.

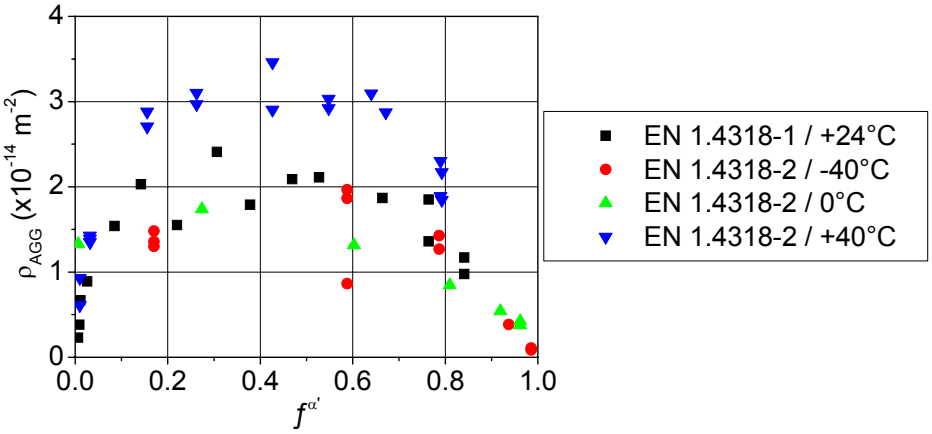

Figure 65 Dislocation density of the austenite per unit volume of the aggregate in EN 1.4318-1 and EN 1.4318-2 steels tensile strained at 3×10^{-4} s^{-1} as a function of α'-martensite volume fraction

Furthermore, the percolation of the α'-martensite phase and the associated increasing contribution of the α'-martensite to the flow stress may affect the plasticity of the austenite and the generation of the shear bands in such a manner that the α'-martensite transformation rate is reduced. The flow stress of the austenite measured by XRD showed a decreasing slope with increasing ε and $f^{\alpha'}$ (Figure 42). This may also affect the nucleation of the α'-martensite, as the nucleation mechanism is essentially stress-dependent.

5.1.4 Effect of temperature on strain-induced α'-martensite transformation

The effect of temperature on the strain-induced α'-martensite transformation was studied on the EN 1.4318-2 steel within the temperature range of -40…+80°C. The transformation was found to be suppressed with increasing temperature. The present results indicate that the temperature dependence (as well as the compositional dependence) of the austenite stability is mainly accounted by the compositional and temperature dependence of the stacking fault energy. The results discussed above demonstrated that the tendency to the shear band formation and the generation of the energetically favourable nucleation sites for the α'-martensite was determined by the SFE. Furthermore, the extensive shear band formation always preceded the onset of α'-martensite formation, and the onset of both shear band and α'-martensite formation showed a similar dependence on the temperature and composition. Although the shear band formation was greatly affected by the temperature, the α'-martensite volume fractions always reached high values, reaching almost 1 at the temperatures up to +40°C. Therefore, once the generation of the nucleation sites started, this was followed by the nucleation of the α'-martensite. This indicates that a significant chemical driving force $\Delta G^{\gamma\rightarrow\alpha'}$ was available also at the higher temperatures and that $\Delta G^{\gamma\rightarrow\alpha'}$ was not significantly affected by the temperature. Therefore, the temperature dependence of $\Delta G^{\gamma\rightarrow\alpha'}$ probably has only a minor role in determining the austenite stability with the chemical compositions and temperatures studied.

The role of the shear bands in the formation of α'-martensite can be assessed by utilising the Olson-Cohen model. Figure 66 shows the parameters of the Olson-Cohen model (equation 18) presented in Table 6 as a function of temperature.

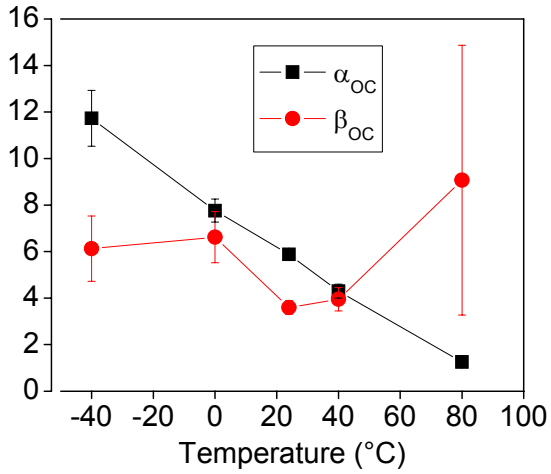

Figure 66 Parameters α_{OC} and β_{OC} of the Olson-Cohen kinetic model determined by least squares fitting from the α'-martensite volume fraction data of EN 1.4318-2 steel

Parameter α_{OC}, corresponding to the rate of the shear band formation, decreased with increasing temperature. By a linear extrapolation it would have reached zero at about +95°C. Recalling equation 10, and by assuming the SFE at +95°C as 22 mJ/m^2, the critical stress for the onset of shear band formation would be 600 MPa, if the Schmid factor of 0.5 was used. However, since the nucleation of α'-martensite requires the presence of intersecting shear bands, a lower Schmid factor must be used. If the

reciprocal of the Taylor factor (0.326) is used, the calculation results in the critical stress of 900 MPa. By taking into account the decreasing flow stress with increasing temperature (Figure 16), the flow stress corresponding to the uniform elongation at +95°C would be about 900 MPa. Therefore, +95°C seems to be the temperature at which the combination of the SFE and applied stress can no longer lead to the generation of energetically favourable nucleation sites for the α'-martensite, and the α'-martensite transformation is entirely prevented. This occurs although the behaviour of the parameter β_{OC}, proportional to the probability of the α'-martensite nucleation, does not predict a significant decrease in the nucleation probability. In fact, the parameter β_{OC}, although exhibiting a high error, had the highest value at +80°C, which is contrary to the previous findings (Olson and Cohen, 1975; Hecker *et al.*, 1982) indicating that β_{OC} goes to zero with increasing temperature.

The rate of the strain-induced α'-martensite transformation was greatly affected by the deformation temperature, as shown in Figure 21. With the increasing temperature the maximum of the transformation rate was delayed to a higher strain level and the maximum value decreased. This feature cannot be explained by Byun's model, or by the above discussion. The rate of the α'-martensite transformation is probably governed by the combination of the SFE and chemical driving force $\Delta G^{\gamma\rightarrow\alpha'}$. As suggested by equation 15 and by Staudhammer *et al.* (1983), an α'-martensite embryo has the critical size of about 57 Å, corresponding to a layer of 27 austenite {111} planes. Therefore, significant overlapping of the stacking faults must occur before the nucleation of the α'-martensite. As the SFE increases with the increasing temperature, the probability of the formation of the shear bands of appropriate thickness and structure decreases (Olson and Cohen, 1972). Consequently, the rate of generation of the nucleation sites for the α'-martensite decreases. Both the XRD results indicating the decreasing formation of ε-martensite with increasing temperature and the Olson-Cohen results presented above support this view.

On the other hand, the chemical driving force affects the critical embryo size through equation 15. The variation of the critical embryo size with temperature was assessed by calculating the $\Delta G^{\gamma\rightarrow\alpha'}$ as a function of temperature. This was done according to Breedis and Kaufman (1971) for two ternary Fe-Cr-Ni alloys. The compositions 17.5%Cr/6.6%Ni and 18.2%Cr/8.1%Ni were used, corresponding to the alloys used in this study. The input data was taken from Breedis and Kaufman (1971) and Kaufman (1966). The calculation results are shown in Figure 67. The results (Figure 67a) predicted higher negative values of $\Delta G^{\gamma\rightarrow\alpha'}$ compared to -1260 J/mole used by Olson and Cohen (1976b) and Staudhammer *et al.* (1983). Consequently, the calculated critical embryo sizes at room temperature were 12 and 14 atom planes for the analysed compositions, respectively, and smaller than the 27 planes estimated by Staudhammer *et al.* (1983). Both $\Delta G^{\gamma\rightarrow\alpha'}$ and the critical embryo size exhibited a linear temperature dependence. For instance, for the 17.5%Cr/6.6%Ni alloy (corresponding to the EN 1.4318 steel) the calculation predicted that the critical embryo size increases from 12 to 16 overlapping {111} planes, when the temperature increases from -40°C to 80°C. Based on the analysis, it is difficult to assess whether it is the SFE or $\Delta G^{\gamma\rightarrow\alpha'}$ that has the most significant effect on the α'-martensite transformation rate. However, an important result is that although $\Delta G^{\gamma\rightarrow\alpha'}$ decreases with increasing temperature, it still has a significant magnitude at the higher temperatures. Therefore, although the temperature affects the nucleation of the α'-martensite through the chemical driving force by

affecting the critical embryo size, the effect of temperature on the SFE seems to be more critical, since it defines the rate of the generation of the nucleation sites. If the generation of the nucleation sites is prevented by the increasing SFE, no transformation will take place in spite of the existence of a significant chemical driving force $\Delta G^{\gamma\rightarrow\alpha'}$.

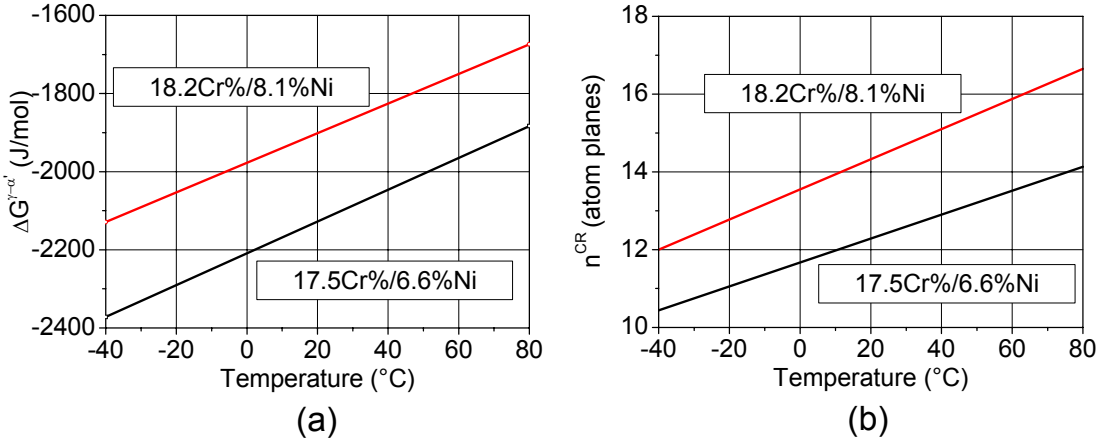

Figure 67 Effect of temperature on (a) chemical driving force $\Delta G^{\gamma\rightarrow\alpha'}$ and (b) critical embryo size n^{CR} of α'-martensite phase in two Fe-Cr-Ni alloys

5.1.5 Effect of strain rate on strain-induced α'-martensite transformation

The tensile test results of the EN 1.4318-1 steel showed that the α'-martensite transformation was suppressed by the increasing strain rate. This was manifested by the decreasing transformation rate and by the shift of the transformation rate maximum to a higher strain level. An opposite effect was observed with the EN 1.4301 steel, in which the transformation was promoted at low strains at 200 s^{-1}. However, the effect was weak and at the high strains the transformation was clearly suppressed at the high strain rates. According to the temperature measurements carried out during the tensile tests at the strain rate of 10^{-1} s^{-1}, the maximum temperature increases due to the adiabatic heating were 80 and 40 K for the EN 1.4318-1 and EN 1.4301 steels, respectively.

There are three ways by which the increased strain rate may affect the strain-induced α'-martensite transformation: 1) by decreasing the chemical driving force $\Delta G^{\gamma\rightarrow\alpha'}$ of the transformation due to the adiabatic heating, 2) by increasing the SFE due to the adiabatic heating, or 3) by enhancing the shear band formation and α'-martensite nucleation due to the increased flow stress. In literature, the first explanation seems to be the most widely accepted (Powell *et al.*, 1958; Bressanelli and Moskowitz, 1966; Neff *et al.*, 1969; Livitsanos and Thomson, 1977; Hecker *et al.*, 1982; Ferreira *et al.*, 2004).

The data shown in Figure 67 can be used to assess the effect of the adiabatic heating on the chemical driving force $\Delta G^{\gamma\rightarrow\alpha'}$. It appears that although according to the calculations $\Delta G^{\gamma\rightarrow\alpha'}$ exhibited clear temperature dependence, overall the change was not large. The change in $\Delta G^{\gamma\rightarrow\alpha'}$ of the EN 1.4318-1 steel caused by the adiabatic heating would be about 300 J/mol, corresponding only a 15% decrease in the chemical driving force. This is not believed to account for the significant reduction of the α'-martensite transformation at the high strain rates. Instead, the effect of the adiabatic heating on the SFE seems to be far more important. Figure 68 illustrates the effect of the adiabatic heating on the SFEs of the EN 1.4318-1 and EN 1.4301 steels tensile strained at 10^{-1} s^{-1}.

The curves were obtained by using the temperature measurement results presented in Figure 15 and the temperature coefficient of 0.1 mJ/m^{2}K. Evidently, the SFE increased rapidly with increasing plastic strain and temperature. Especially significant was the increase of the SFE in the metastable steel showing higher adiabatic heating and lower SFE at room temperature.

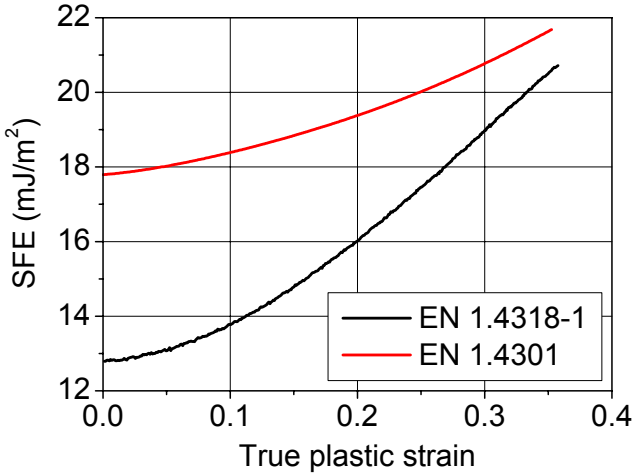

Figure 68 Effect of adiabatic heating on the stacking fault energies of EN 1.4318-1 and EN 1.4301 steels at the strain rate of 10^{-1} s^{-1} as a function of true plastic strain

Recalling the discussion in the previous section, the increasing SFE due to the adiabatic heating decelerates the overlapping process of the stacking faults and, thus, hinders the formation of the nucleation sites for the α'-martensite. As the critical embryo size at the same time increases due to the decreasing chemical driving force, the transformation rate is reduced. However, when considering the high speed deformation the situation is rather different compared to the deformation occurring at constant temperature. For instance, in the unstable EN 1.4318-1 steel large number of shear bands formed in the beginning of the deformation, since the SFE remained relatively constant at the low strains. When the strain and heating increased, the SFE increased significantly and the overlapping process was impeded. However, due to the high number of shear bands formed in the beginning of the deformation, the α'-martensite transformation was still able to proceed, but the transformation rate was reduced. With the EN 1.4301 steel the strain-induced α'-martensite transformation was almost entirely prevented at the high strain rates. This was probably related to the fact that even at the lowest strain rate, representing the isothermal condition, significant shear band formation and α'-martensite transformation occurred only at strains above 0.2. At the high strain rates the adiabatic heating at this strain level was already so significant that the increase in the SFE and the decrease in the chemical driving force were enough to prevent the transformation entirely.

So far, only the adiabatic heating of bulk material has been considered. However, locally higher temperatures may occur if the strain rate is high. For instance, for the EN 1.4318-1 steel $\Delta G^{\gamma\rightarrow\alpha'}$ was about -2100 J/mol. By taking into account the strain energy component of 500 J/mol (Olson and Cohen, 1976b), the transformation from the austenite to the α'-martensite involves a free-energy release of -1600 J/mol. This energy is converted to heat, which leads to an abrupt local heating of 57 K, if the density is estimated as 7900 kg/m^3 and the specific heat as 500 J/kgK. Therefore, if numerous α'-martensite embryos are repeatedly nucleated in the vicinity of each other, this may lead

to locally higher temperature increases than measured macroscopically. This probably efficiently restricts further growth of the α'-martensite. Another feature not taken into account so far is related to the non-homogeneous nature of the plastic deformation of the metastable steel grades. At the low α'-martensite volume fractions the plastic deformation is believed to take place mainly in the austenite phase. Therefore, the local heating of the austenite phase differs from the macroscopic behaviour shown in Figure 15. Furthermore, in the austenite phase the slip activity is concentrated to the shear bands, which may exhibit locally higher heating than the bulk austenite. Therefore, the local effects of the adiabatic heating may be more pronounced than the bulk heating discussed above.

Beyond the adiabatic heating, also the direct effects of the high strain rate and the associated higher flow stress on the microstructural evolution have been discussed in literature. Staudhammer *et al.* (1980), Hecker *et al.* (1982) and Murr *et al.* (1982) found the high strain rate to promote the shear band formation and the strain-induced α'-martensite transformation in AISI 304 steel, but did not explain the mechanism. In the present work the EN 1.4301 steel was found to exhibit similar characteristics at low strains at the strain rate of 200 s^{-1}. However, the effect was negligibly small and had no observable influence on the mechanical behaviour. Furthermore, in the EN 1.4318-1 steel no distinguishable effect of the strain rate on the shear band formation was found. It seems that the higher tendency to the shear band and α'-martensite formation at the high strain rate is explained in terms of higher the flow stress promoting the instability of the stacking faults, which promotes the formation of the nucleation sites. The strain rate has the most pronounced effect on the shear band formation when the value of SFE is such that the shear bands are not formed at the early stages of the deformation at a low strain rate. Increasing the strain rate in this condition rises the flow stress above the critical level, which enhances the formation of shear bands and the α'-martensite phase. This effect is probably present only at the early stages of deformation, when the adiabatic heating remains low.

Ferreira *et al.* (2004) found high strain rate (order of 10^3 s^{-1}) to promote the formation of the ε-martensite and stacking faults (*i.e.*, shear bands). This was explained in terms of the lower energy barrier to nucleate the partial dislocation loops and the higher mobility of the partial dislocations at the high strain rate compared to perfect dislocations. However, the analysis ignored the formation of the partial dislocations even spontaneously according to Frank's rule in low SFE austenitic stainless steels. This is observed from the TEM micrographs presented in section 4.7, as well as from numerous TEM investigations published in literature. Therefore, most probably the behaviour of the partial dislocations under applied stress and the SFE itself control the formation of wide stacking faults and ε-martensite, and not the nucleation of the partial dislocations.

5.2 Effect of microstructural evolution on mechanical properties

The results of the tensile tests and the phase identification indicated that the strain-induced α'-martensite transformation and the mechanical response of the studied steels were closely interlinked. The work-hardening rate deviated from the regular continuously decreasing trend, typical of single phase metals and alloys, due to the strain-induced α'-martensite transformation. Furthermore, a correspondence between the rate of the α'-martensite transformation and the work-hardening rate was found, and

it was found to be independent on the chemical composition and experimental conditions. Therefore, the present discussion concentrates mainly to the role of the α'-martensite phase in the mechanical response.

5.2.1 Effect of α'-martensite transformation on work-hardening rate

The unstable EN 1.4318-1 steel showed a similar work-hardening abnormality (Figure 13) as previously reported in literature (Huang *et al.*, 1989; Fang and Dahl, 1991; De *et al.*, 2006). The EN 1.4318-2 steel tested at different temperatures showed that the work-hardening behaviour was strongly dependent on the temperature, and that the abnormality disappeared as the temperature increased (Figure 17). According to the results, this correlated closely with the observed changes in the austenite stability, emphasising the close relation between the work hardening and the strain-induced α'-martensite transformation.

Based on the results, the work-hardening sequence of an unstable austenitic stainless steel grade may be divided in four stages. The work-hardening stages are illustrated in Figure 69, which presents the work-hardening rate of the EN 1.4318-2 steel strained at +24°C at the strain rate 3×10^{-4} s^{-1} as a function of true strain. The corresponding α'-martensite volume fractions are shown with red circles and dashed line. In the following, each work-hardening stage will be discussed in detail.

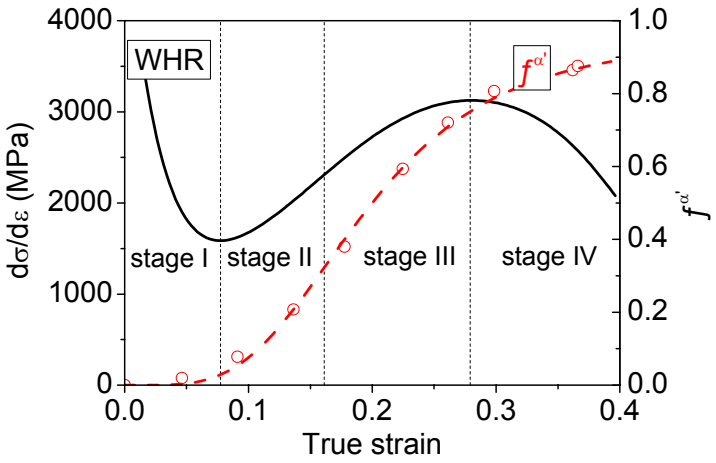

Figure 69 Work-hardening rate of EN 1.4318-2 steel strained at strain rate 3×10^{-4} s^{-1} at +24°C divided in four stages and corresponding volume fraction of α'-martensite as a function of true strain

Stage I

During the stage I the work-hardening rate decreased rapidly. In fact, the WHR of the unstable EN 1.4318-1 steel reached considerably lower values than that of the stable EN 1.4301 steel after equivalent plastic strain. In the EN 1.4318-2 steel the minimum WHR was essentially dependent on the temperature and the extent of the α'-martensite transformation: the lowest work-hardening rates were found at the lowest temperatures, where the α'-martensite transformation rate was the highest.

The rapidly decreasing WHR during the stage I has been related to the rapid formation of ε-martensite by Reed and Guntner (1964) and recently by De *et al.* (2006). The softening effect was explained by the appearance of the highest amount of ε-martensite in conjunction with the WHR minimum. A similar conclusion could be drawn from the present results. However, this explanation seems to conflict with the elementary dislocation theory. The formation of ε-martensite is directly related to the formation of stacking faults and Shockley partial dislocations, which are unable to cross-slip. Furthermore, the stacking faults and ε-martensite should rather act as obstacles for the slip than to provide an easy mode of deformation. Therefore, the formation of the stacking faults and ε-martensite should rather increase than decrease the work-hardening rate. Suzuki *et al.* (1976; 1977) also questioned the explanations related to the ε-martensite formation, and suggested that the low WHR is related to the nucleation of the α'-martensite at the shear band intersections. Thus, the nucleation provides a mechanism, referred to as the window effect, by which two shear bands, which otherwise would be barriers to each others, can intersect easily. This was proven by *in-situ* TEM experiments on AISI 304 steel. In more general terms, the α'-martensite nucleation has been suggested to cause a dynamic softening effect due to the α'-martensite transformation strain, *i.e.*, by the operation of the phase transformation as a competing deformation mechanism (Narutani *et al.*, 1982; Olson and Cohen, 1986; Huang *et al.*, 1989). In terms of thermodynamics, the dynamic softening effect may be understood as the external load needed to deform the material was facilitated by the chemical driving force of the α'-martensite transformation. The present results indeed indicate that the stage I is related to the onset of the α'-martensite formation, as shown in Figures 13 and 18 (EN 1.4318-1 steel) and Figures 17 and 19 (EN 1.4318-2 steel). The minimum WHR was always reached, when $f^{\alpha'}$ was about 0.05.

Based on the experimental evidence, Narutani *et al.* (1982) suggested that the dynamic softening contribution σ_S due to the α'-martensite transformation is proportional to rate of the α'-martensite transformation $df^{\alpha'}/d\varepsilon$. Accordingly, the softening rate $d\sigma_S/d\varepsilon$ due to the transformation is proportional to $d^2f^{\alpha'}/d\varepsilon^2$. This can be proven by a simple consideration as follows. If the plastic deformation is aided by the chemical driving force $\Delta G^{\gamma\rightarrow\alpha'}$, the external work needed to induce the deformation is decreased by $\sigma_S d\varepsilon$. Therefore, provided that the softening contribution due to $\Delta G^{\gamma\rightarrow\alpha'}$ is assumed to be constant, the relation between the reduction in the mechanical work and the transformed volume fraction is:

$$-\sigma_S d\varepsilon \propto \Delta G^{\gamma\rightarrow\alpha'} df^{\alpha'}. \tag{64}$$

By rearrangement and differentiating the following relation is obtained:

$$-\frac{d\sigma_S}{d\varepsilon} \propto \Delta G^{\gamma\rightarrow\alpha'} \frac{d^2 f^{\alpha'}}{d\varepsilon^2}, \tag{65}$$

which verifies the experimental findings of Narutani *et al.* (1982). Figure 70 shows the comparison between the WHR and the second derivatives of the $f^{\alpha'}$-ε curves of the EN 1.4318-2 steel presented in Figure 19. An excellent correlation between both the location and magnitude of the maximum $d^2f^{\alpha'}/d\varepsilon^2$ and minimum WHR was found. The minimum WHR was in all cases reached slightly before the maximum $d^2f^{\alpha'}/d\varepsilon^2$. This is probably because the increasing α'-martensite volume fraction causes an increasing

dispersion hardening effect, which is not taken into account in the above treatment. Therefore, the minimum WHR, *i.e.*, the shift from stage I to II occurs when the combination of the dynamic softening and hardening effects of α'-martensite reaches the lowest value.

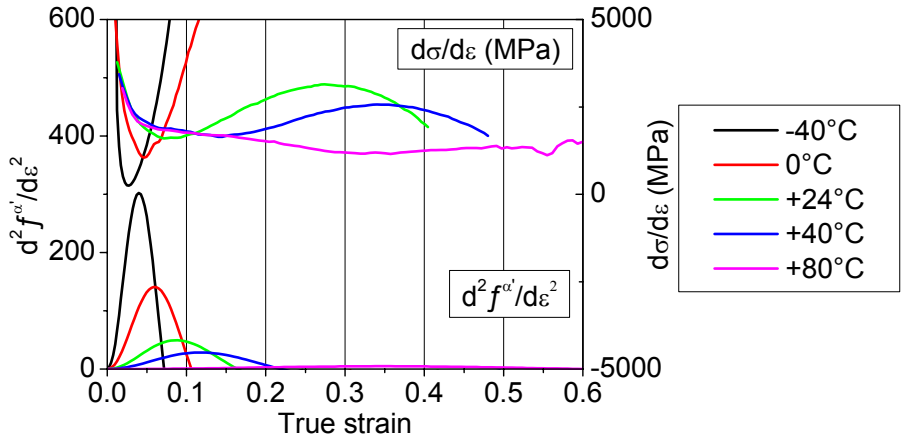

Figure 70 Comparison of work-hardening rates and second derivatives of the $f^{\alpha'}$-ε curves of EN 1.4318-2 steel tensile strained at strain rate 3×10^{-4} s^{-1}

Evidence of the softening effect was obtained also from the σ vs. $\rho^{1/2}$ plots presented in Figures 38 and 39. The unstable EN 1.4318-1 steel showed lower slope than that of the stable EN 1.4301 steel when $f^{\alpha'}<0.3$, *i.e.*, at a given dislocation density the unstable steel showed lower flow stress.

Stage II

The shift from the stage I to the stage II, corresponding to the minimum work-hardening rate, occurred always slightly after the onset of the α'-martensite transformation, at about $f^{\alpha'}=0.05$. This feature could be observed even with the stable EN 1.4301 steel at the lowest strain rate, where the WHR minimum occurred at the true strain of 0.42 (Figure 14). As discussed above, the stage I is characterised by the dynamic softening effect due to the α'-martensite transformation. The stage II involving the increasing WHR, therefore, begins when the strengthening effect of the α'-martensite phase starts to dominate the work hardening. The results of the present investigation indicate that the α'-martensite increases the flow stress and the work-hardening rate of an austenite-α'-martensite aggregate by two mechanisms:

1. When the α'-martensite volume fraction remains below the percolation threshold ($f^{\alpha'}=0.3$), the microstructure consists of hard α'-martensite dispersions or clusters mounted in a softer austenite matrix. Due to the non-homogeneous plastic deformation, the dislocation generation in the austenite is enhanced, which was well evidenced by the XRD dislocation density measurements. The enhanced dislocation generation gives a rise in the flow stress and work-hardening rate. This mechanism is believed to be operative during the stage II.

2. When the α'-martensite volume fraction exceeds the percolation threshold, the α'-martensite forms a percolating cluster extending through the whole aggregate, which

further increases the work hardening. This mechanism is believed to be operative during the stage III.

The calculated density of the geometrically necessary dislocations in the austenite phase of the EN 1.4318-1 steel correlated well with the measured dislocation density (section 4.8.3). The contribution of the dislocation generation in the austenite to the flow stress may be assessed by remembering that the flow stress is related to the square root of the dislocation density (equation 50). Thus, the work-hardening rate contribution due to the generation of the geometrically necessary dislocations may be assessed based on ρ_G with equation 50. The slope $\alpha_0 Gb=1.937\times10^{-5}$ obtained from XRD broadening analysis (Figure 38) was used in the calculation. The work-hardening rate, plotted with red dots in Figure 71, was then obtained by numerical differentiation of the calculated stress against the true plastic strain. The calculated WHR showed similar behaviour as the transformation rate (Figure 20), and therefore, its maximum was located at about $f^{\alpha'}=0.3$, corresponding to the percolation threshold of the α'-martensite. Furthermore, a rather good correlation between the measured and calculated work-hardening rates was observed during the stage II. The work-hardening rate of the two-phase aggregate, however, continued to increase further when the percolation threshold of $f^{\alpha'}$ was exceeded. Therefore, the results indicate that the work-hardening rate is dominated by the generation of the geometrically necessary dislocations only up to the percolation threshold of the α'-martensite, after which another mechanism must account for the increasing WHR.

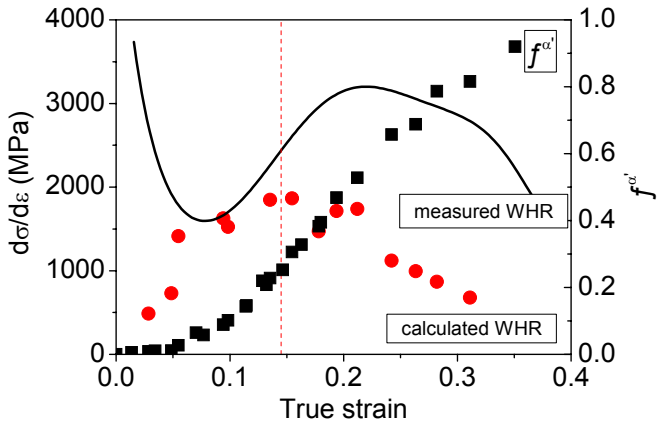

Figure 71 Work-hardening rate of EN 1.4318-1 steel tensile strained at strain rate 3×10^{-4} s^{-1} at room temperature calculated from the density of geometrically necessary dislocations and compared to the actual work-hardening rate and α'-martensite volume fraction

Stage III

The onset of the stage III is related to the formation of a percolating cluster of the α'-martensite. This occurs when the α'-martensite volume fraction exceeds the percolation threshold of 0.3. The percolation of the α'-martensite phase was well illustrated by the image analysis carried out on the optical micrographs. The formation of the percolating cluster became evident also in the σ-$(f^{\alpha'})^{1/2}$ and σ-$\rho^{1/2}$ plots (Figures 24 and 38, respectively), which exhibited an abrupt change in the slope at the stress level corresponding to the percolation threshold. After exceeding the percolation threshold

also the stress level in the austenite phase deviated significantly from the macroscopic stress (Figure 42). These features indicate that above the percolation threshold the flow stress is no longer determined by the dislocation density of the austenite phase alone.

The strengthening effect of the α'-martensite phase above the percolation threshold may be understood as follows. Once a percolating cluster is formed, it extends through the whole body. Thus, the plastic deformation of the aggregate can no longer be fully accommodated by the plasticity of the austenite, but also the α'-martensite must deform. As the α'-martensite phase possesses higher dislocation density and yield strength compared to those of the austenite, it is reasonable that the external load needed to deform the aggregate increases rapidly after the formation of the percolating cluster. Furthermore, as the α'-martensite volume fraction further increases, the strength of the α'-martensite cluster increases. Correspondingly, the work-hardening rate keeps on increasing with the increasing $f^{\alpha'}$.

Although the contribution of the α'-martensite on the flow stress becomes more and more dominant as its volume fraction increases, the austenite phase undergoes significant plastic deformation even at high α'-martensite volume fractions. This is supported by two observations: 1) the austenite showed markedly larger change in the dislocation density with increasing plastic strain, indicating the occurrence of the plastic deformation, and 2) the generation of the geometrically necessary dislocations in the austenite phase correlated well with the measured dislocation densities. The behaviour of the austenite before and after the percolation threshold of the α'-martensite is well illustrated in Figure 72, which shows the comparison of the applied macroscopic stress and the stress in the austenite phase measured with XRD as a function of $\rho^{1/2}$ of the austenite. The stress level in the austenite was lower due to the stress relaxation that occurred during the *in-situ* stress measurements. However, an excellent linear fit between the dislocation density and the stress level in the austenite phase was found, and the plot representing the macroscopic stress deviated from the linear trend at the point at which $f^{\alpha'}$ exceeded 0.3.

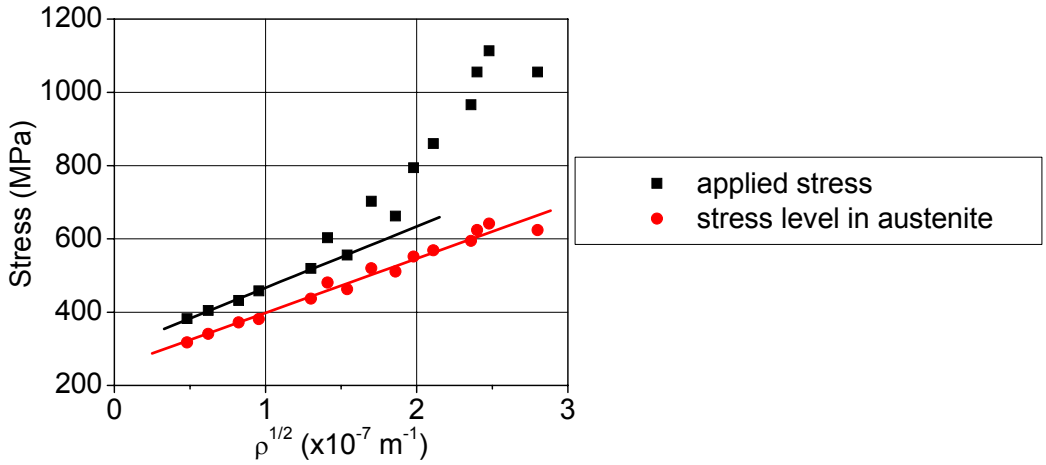

Figure 72 Applied macroscopic stress and stress level in austenite phase measured by XRD as a function of square root of dislocation density of austenite determined by IBM

Stage IV

The onset of the work-hardening stage IV was associated to the maximum work-hardening rate, and during the stage IV WHR decreased. At the strain rate 3×10^{-4} s^{-1} the shift from the stage III to IV occurred when the α'-martensite volume fraction reached 0.6-0.7. This was valid for both the EN 1.4318-1 and EN 1.4318-2 steels at all deformation temperatures. One might attribute this to the 2D percolation threshold of the α'-martensite ($f^{\alpha'}$=0.593), or to the 3D percolation threshold of the austenite ($f^{\alpha'}$=1-0.312=0.688). In any case, at high volume fractions the role of the deformation of the α'-martensite phase in accommodating the shape change of the aggregate becomes more and more important. This was also indicated by the XRD stress analysis, which showed that the stress level in the α'-martensite and the macroscopic stress coincided at about $f^{\alpha'}$=0.7, corresponding to the 3D percolation threshold of the austenite phase. Latest at this point the plastic deformation of the aggregate becomes dominated by the plasticity and dynamic recovery of the α'-martensite phase, and the material behaviour starts to resemble the behaviour of a single phase material again. Accordingly, the work-hardening rate starts to decrease.

However, the above discussion applies only to the isothermal conditions. At the high strain rates the stage IV started in the EN 1.4318-1 steel prematurely, *i.e.* at the α'-martensite volume fractions much less than 0.7. The behaviour is probably related to the adiabatic heating that decreased the rate of the α'-martensite transformation. As according to the results the transformation rate affected directly the WHR, the decreasing transformation rate caused the WHR to decrease. When only little α'-martensite was formed, as in the EN 1.4301 steel at room temperature and in the EN 1.4318-2 steel at +80°C, the stage IV did not exist at all, because the plastic instability occurred before the WHR exhibited any decrease.

5.2.2 Effect of shear bands on work-hardening rate

The strain-induced α'-martensite transformation in austenitic stainless steels is interlinked to the formation of shear bands (*i.e.*, stacking faults, ε-martensite, twins). Therefore, when assessing the effect of the α'-martensite phase on the mechanical response, one must be aware of taking into account the influence of the shear bands. It has been suggested that the formation of the stacking faults, ε-martensite and twins alone enhance the work hardening of austenitic Co-Ni-Cr-Mo (Rémy and Pineau, 1976) and Fe-Mn-Cr-C alloys (Rémy and Pineau, 1977), as well as the work hardening of austenitic stainless steels (Müllner *et al.*, 1993; 1994; Byun *et al.*, 2004). The strengthening mechanism was explained in terms of the ε-martensite platelets and twins acting as strong glide obstacles, thus, increasing the work-hardening rate. However, this mechanism is believed not to be operative in the case of metastable austenitic Cr-Ni stainless steels. As suggested by several authors (Lecroisey and Pineau, 1972; Suzuki *et al.*, 1976; 1977; Brooks *et al.*, 1979a; 1979b), the nucleation of the α'-martensite is the mechanism, which allows the slip to propagate through the intersecting shear bands. As the process is aided by the chemical free-energy difference $\Delta G^{\gamma\rightarrow\alpha'}$, the combined formation of the shear bands and α'-martensite initially rather eases the evolution of the plastic deformation, as discussed in section 5.2.1. Therefore, the formation of the shear bands is not believed to enhance the work hardening of the studied steels directly, but through the generation of the nucleation sites for the hard α'-martensite phase. Indeed,

in the investigations in which the shear band formation has been reported to enhance the work hardening, the presence of the α'-martensite has not been reported. In such a case, the ε-martensite and twins may dominate the work-hardening behaviour, since the nucleation of the α'-martensite phase does not provide the easy mechanism for the slip systems to intersect.

5.2.3 Effect of α'-martensite transformation on ductility

The experimental results showed that the uniform elongation of the studied steels was strongly dependent on the work-hardening rate. The uniform elongation, *i.e.*, the onset of the plastic instability, is defined according to Considére's criterion by the balance between the decrease in the load bearing capacity due to the decreasing cross-sectional area and the increased strength due to the work hardening. In the derivation of Considére's criterion the plastic deformation is assumed to be a constant volume process. In the present case this was, however, not exactly true, since the α'-martensite transformation is accompanied by a volume increase of about 2%. However, this effect was considered to be negligible.

According to the present results, the work-hardening rate was closely related to the α'-martensite transformation rate. Thus, it is evident that the high uniform elongation of metastable austenitic stainless steels is related to the enhanced work hardening due to the transformation, and not directly to the transformation strain or to the volume change related to the transformation. In fact, the experimental results showed that the highest uniform elongations were obtained when relatively low amount of α'-martensite was formed (*e.g.*, the EN 1.4301 steel strained at room temperature and the EN 1.4318-2 steel at +80°C). The EN 1.4301 steel showed a drastic decrease of the uniform elongation when the steel was deformed at higher strain rates (Figure 14). This was clearly related to the suppression of the α'-martensite transformation, which reduced the work-hardening rate, and made the stress-strain and WHR curves to intersect at a lower strain. On the other hand, the EN 1.4318-2 steel demonstrated that if the α'-martensite transformation occurs rapidly in the beginning of the deformation, the work-hardening rate drops rapidly after reaching the maximum, resulting in a low uniform elongation (Figure 17). In such a case, the high strain rate increases the uniform elongation, since it decreases the transformation rate and WHR, and shifts the intersection of the WHR and stress-strain curves to higher strains. Such a behaviour was exhibited by the EN 1.4318-1 steel (Figure 13), although the effect was weak.

To summarise, the behaviours of the EN 1.4301 steel at room temperature and the EN 1.4318-2 steel at +80°C seem to correspond to the situation, where the highest uniform elongation is reached in isothermal conditions. However, increase in the strain rate may in these cases cause a significant decrease in the elongation. This feature is of a significant importance, since the strain rates used in any sheet metal forming operations are much higher than the lowest strain rate used in this study. Therefore, in practice the deformation is seldom isothermal. According to the results, the metastable steel grades exhibiting significant strain-induced α'-martensite transformation show lower strain-rate dependence of the uniform elongation. However, as illustrated by the isothermal test results of the EN 1.4318-2 steel, the deformation temperature strongly affects the uniform elongation of the unstable steels.

5.3 Subjects of further studies

A variety of experimental techniques utilised in the present study enabled the obtaining of a representative picture of the tensile deformation behaviour of the metastable austenitic stainless steels. However, there are several areas where further studies are desirable.

The temperature dependence of the SFE was in the key role in the analysis of the strain rate and temperature dependence of the austenite stability. The analysis relied on the temperature coefficients of the SFE taken from literature. The plausibility of the present conclusions could be improved by determining the temperature dependence of the SFE for the studied steel grades.

During the recent years the electron backscatter diffraction (EBSD) has been increasingly used in the field of materials science. Furthermore, it has been successfully exploited to study deformation microstructures of metastable austenitic stainless steels (Gey *et al.*, 2005). The EBSD technique would be a unique tool in examining the crystallographic features of the shear bands and the α'-martensite phase, as well as the evolution of the deformation textures, which was omitted in the present study. In particular, *in-situ* ECCI and EBSD examination during the plastic deformation would give an excellent insight into the evolution of the deformation microstructures and textures.

The transmission electron microscopy study included in this thesis was limited. A more extensive TEM examination would be useful in order to confirm the findings made with the other experimental techniques, including the ECCI examination of the microstructures and the dislocation density and stacking fault energy measurements carried out with the XRD. It must, however, be noticed that the TEM technique involves severe limitations. The sample preparation for the TEM is laborious and involves the risk of affecting or losing microstructural features. Furthermore, the TEM examination of highly deformed microstructures is difficult or even impossible.

The present thesis concentrated only to the experimental research. However, recently the plasticity of austenitic stainless steels has been investigated also from the mechanics point of view. The continuum mechanics modelling would be an alternative approach to study the mechanisms behind the abnormal work-hardening behaviour, and especially the role of the dispersion hardening effect and the percolation of the α'-martensite phase.

The use of the metastable austenitic stainless steels in the sheet metal forming has been hindered by the lack of reliable constitutive models taking into account the TRIP effect, which has limited the accuracy of the FEM analysis of the forming process. The knowledge obtained in the present work is believed to serve as a useful basis for the further development of the constitutive material models.

6 CONCLUSIONS

In this thesis the mechanical properties and microstructural evolution during the plastic deformation of metastable austenitic stainless steels were studied. The austenitic stainless steel grades EN 1.4318 and EN 1.4301 were tensile tested at different strain rates and temperatures. The mechanical response was interlinked with the observed deformation microstructures. Based on the results, the following conclusions can be drawn:

1. The onset of the formation of the shear bands in the austenite phase is determined by the balance between the intrinsic stacking fault energy (SFE) and the resolved shear stress caused by the applied load.

2. The temperature and chemical composition seem to affect the austenite stability mainly through their influence on the SFE. Although the chemical driving force of the transformation is also affected, it seems to have only a minor role in determining the austenite stability.

3. Increasing strain rate decreases the rate of the strain-induced α'-martensite transformation. This is attributed to the adiabatic heating that increases the SFE and decreases the chemical driving force of the α'-martensite transformation.

4. XRD line broadening analysis showed that the dislocation density of the austenite phase increases with increasing plastic strain and α'-martensite volume fraction. Instead, the dislocation density of the α'-martensite phase remains relatively constant, and is significantly higher than the dislocation density of the austenite phase.

5. The deviation of the work-hardening rate of a metastable austenitic stainless steel from the continuously decreasing trend, referred to as the work-hardening abnormality, is attributed to the strain-induced α'-martensite transformation. Based on the observed behaviour, the work-hardening sequence was divided in four stages.

6. During the stage I the work-hardening rate decreases rapidly, and reaches lower level than in stable steel at the same plastic strain. This is caused by the onset of the α'-martensite transformation, which by operating as an alternative mechanism of plastic deformation, aided by the chemical driving force, eases the deformation and causes the effect referred to as dynamic softening.

7. During the stage II the α'-martensite volume fraction increases so that its strengthening effect masks the dynamic softening effect. Consequently, the work-hardening rate starts to increase with increasing plastic strain. During the stage II the α'-martensite particles act as hard undeformable dispersions embedded in the softer austenite matrix, and enhance the dislocation generation in the austenite phase due to the non-homogeneous plastic deformation.

8. During the stage III the hard α'-martensite phase forms a percolating cluster. Thereafter, also the α'-martensite phase must deform in order to accommodate the shape change of the aggregate. Consequently, the work-hardening rate continues to increase with increasing plastic strain and α'-martensite volume fraction.

9. During the stage IV the work-hardening rate decreases. In the most cases the stage IV began when the α'-martensite volume fraction reached about 0.7. Therefore, during the stage IV the aggregate consists mainly of the α'-martensite phase, and the material behaviour starts to resemble the behaviour of a single phase material. At the high strain rates the suppression of the α'-martensite transformation made the stage IV to begin at lower α'-martensite volume fractions.

10. The strain-induced α'-martensite transformation affects the uniform elongation through its influence on the work-hardening rate. The highest uniform elongation is reached when the transformation effectively shifts the intersection of the WHR and stress-strain curves to high strains.

11. Extensive EBSD and TEM examinations, continuum mechanics modelling and the development of the constitutive material models are proposed as the subjects of further studies.

REFERENCES

Abrassart, F. 1973. Stress-Induced γ→α' Martensitic Transformation in Two Carbon Stainless Steels, Application to Trip Steels. Metallurgical Transactions, 4 (9), pp. 2205-2216.

Angel, T. 1954. Formation of Martensite in Austenitic Stainless Steels. Journal of the Iron and Steel Institute, 177 (5), pp. 165-174.

Ashby, M.F. 1971. The Deformation of Plastically Non-Homogeneous Alloys. In: Kelly, A. and Nicholson, R.B. (Eds.). Strengthening Methods in Crystals. Elsevier Publishing Company Ltd, Barking, UK, pp. 137-192.

ASTM E 112-96. 1997. Standard Test Methods for Determining Average Grain Size. In: Annual Book of ASTM Standards, Volume 03.01, Metals – Mechanical Testing; Elevated and Low-Temperature Tests; Metallography. American Society for Testing and Materials, West Conshohocken, USA, pp. 227-249.

Balzar, D. 1992. Profile Fitting of X-ray Diffraction Lines and Fourier Analysis of Broadening. Journal of Applied Crystallography, 25 (5), pp. 559-570.

Balzar, D. and Ledbetter, H. 1993. Voigt-Function Modeling in Fourier Analysis of Size- and Strain-Broadened X-ray Diffraction Peaks. Journal of Applied Crystallography, 26 (1), pp. 97-103.

Balzar, D. and Popović, S. 1996. Reliability of the Simplified Integral-Breadth Methods in Diffraction Line-Broadening Analysis. Journal of Applied Crystallography, 29 (1), pp. 16-23.

Balzar, D. 1999. Voigt Function Model in Diffraction-Line Broadening Analysis. In: Snyder, R.L., Fiala, J. and Bunge, H.-J. (Eds.). Defect and Microstructure Analysis by Diffraction. Oxford University Press, Oxford, UK, pp. 94-126.

Balzar, D., Audebrand, N., Daymond, M.R., Fitch, A., Hewat, A., Langford, J.I., Le Bail, A., Louër, D., Masson, O., McCowan, C.N., Popa, N.C., Stephens, P.W. and Toby, B.H. 2004. Size-Strain Line-Broadening Analysis of the Ceria Round-Robin Sample. Journal of Applied Crystallography, 37 (6), pp. 911-924.

Balzar, D. 2006. BREADTH - A PC Program for Analyzing Diffraction-Line Broadening. http://www.du.edu/%7ebalzar/breadth.htm. Updated 6th December 2005.

Bever, M.B. 1973. Stored Energy of Cold Work. Progress in Materials Science, 17, 190 p.

Bhadeshia, H.K.D.H. 2002. TRIP-Assisted Steels? ISIJ International, 42 (9), pp. 1059-1060.

Bogers, A.J. and Burgers, W.G. 1964. Partial Dislocations on the {110} Planes in the B.C.C. Lattice and the Transition of the F.C.C. into the B.C.C. Lattice. Acta Metallurgica, 12 (2), pp. 255-261.

Bolling, G.F. and Richman, R.H. 1970. The Plastic Deformation-Transformation of Paramagnetic F.C.C. Fe-Ni-C Alloys. Acta Metallurgica, 18 (6), pp. 673-681.

Bowkett, M.W., Keown, S.R. and Harries, D.R. 1982. Quench- and Deformation-Induced Structures in Two Austenitic Stainless Steels. Metal Science, 16 (11), pp. 499-517.

Breedis, J.F. and Kaufman, L. 1971. Formation of Hcp and Bcc Phases in Austenitic Iron Alloys. Metallurgical Transactions, 2 (9), pp. 2359-2371.

Bressanelli, J.P. and Moskowitz, A. 1966. Effects of Strain Rate, Temperature, and Composition on Tensile Properties of Metastable Austenitic Stainless Steels. Transactions of the ASM, 59 (2), pp. 223-239.

Brofman, P.J. and Ansell, G.S. 1978. On the Effect of Carbon on the Stacking Fault Energy of Austenitic Stainless Steels. Metallurgical Transactions A, 9 (6), pp. 879-880.

Brooks, J.W., Loretto, M.H. and Smallman, R.E. 1979a. *In Situ* Observations of the Formation of Martensite in Stainless Steel. Acta Metallurgica, 27 (12), pp. 1829-1838.

Brooks, J.W., Loretto, M.H. and Smallman, R.E. 1979b. Direct Observations of Martensite Nuclei in Stainless Steel. Acta Metallurgica, 27 (12), pp. 1839-1847.

Byun, T.S. 2003. On the Stress Dependence of Partial Dislocation Separation and Deformation Microstructure in Austenitic Stainless Steels. Acta Materialia, 51 (11), pp. 3063-3071.

Byun, T.S., Lee, E.H. and Hunn, J.D. 2003. Plastic Deformation in 316LN Stainless Steel – Characterization of Deformation Microstructures. Journal of Nuclear Materials, 321 (1), pp. 29-39.

Byun, T.S., Hashimoto, N. and Farrell, K. 2004. Temperature Dependence of Strain Hardening and Plastic Instability Behaviours in Austenitic Stainless Steels. Acta Materialia, 52 (13), pp. 3889-3899.

Cherkaoui, M., Berveiller, M. and Sabar, H. 1998. Micromechanical Modeling of Martensitic Transformation Induced Plasticity (TRIP) in Austenitic Single Crystals. International Journal of Plasticity, 14 (7), pp. 597-626.

Cherkaoui, M., Berveiller, M. and Lemoine, X. 2000. Couplings between Plasticity and Martensitic Phase Transformation: Overall Behavior of Polycrystalline TRIP Steels. International Journal of Plasticity, 16 (10-11), pp. 1215-1241.

Copley, S.M. and Kear, B.H. 1968. The Dependence of the Width of a Dissociated Dislocation on Dislocation Velocity. Acta Metallurgica, 16 (2), pp. 227-231.

Cortés, J.A., Tsuta, T., Mitani, Y. and Osakada, K. 1992. Flow Stress and Phase Transformation Analyses in the Austenitic Stainless Steel under Cold Working. Part 1, Phase Transformation Characteristics and Constitutive Formulation by Energetic Criterion. JSME International Journal, 35 (1), pp. 201-209.

Cottrell, A.H. 1953. Dislocations and Plastic Flow in Crystals. Oxford University Press, London, UK, 223 p.

De, A.K., Murdock, D.C., Mataya, M.C., Speer, J.G. and Matlock, D.K. 2004. Quantitative Measurement of Deformation-Induced Martensite in 304 Stainless Steel by X-Ray Diffraction. Scripta Materialia, 50 (12), pp. 1445-1449.

De, A.K., Speer, J.G., Matlock, D.K., Murdock, D.C., Mataya, M.C. and Comstock, Jr., R.J. 2006. Deformation-Induced Phase Transformation and Strain Hardening in Type 304 Austenitic Stainless Steel. Metallurgical and Materials Transactions A, 37 (6), pp. 1875-1885.

Diani, J.M., Sabar, H. and Berveiller, M. 1995. Micromechanical Modelling of the Transformation Induced Plasticity (TRIP) Phenomenon in Steels. International Journal of Engineering Sciences, 33 (13), pp. 1921-1934.

Eckstein, C.B. and Guimarães, J.R.C. 1984. Microstructure-Property Correlation in Martensite-Austenite Mixtures. Journal of Materials Science, 19 (9), pp. 3043-3048.

El-Magd, E., Scholles, H. and Weisshaupt, H. 1997. Dynamic Ductility of Metals. Journal de Physique IV, 7 (C3), pp. 349-354.

Fang, X.F. and Dahl, W. 1991. Strain Hardening and Transformation Mechanism of Deformation-Induced Martensite Transformation in Metastable Austenitic Stainless Steels. Materials Science and Engineering A, 141 (2), pp. 189-198.

Ferreira, P.J and Müllner, P. 1998. A Thermodynamical Model for the Stacking-Fault Energy. Acta Materialia, 46 (13), pp. 4479-4484.

Ferreira, P.J., Vander Sande, J.B., Amaral Fortes, M. and Kyröläinen, A. 2004. Microstructure Development during High-Velocity Deformation. Metallurgical and Materials Transactions A, 35 (10), pp. 3091-3101.

Fischer, F.D., Reisner, G., Werner, E., Tanaka, K., Cailletaud, G. and Antretter, T. 2000. A New View on Transformation Induced Plasticity. International Journal of Plasticity, 16 (7-8), pp. 723-748.

Fujita H. and Ueda, S. 1972. Stacking Faults and F.C.C. (γ) $\rightarrow$ H.C.P. (ε) Transformation in 18/8-Type Stainless Steel. Acta Metallurgica, 20 (5), pp. 759-767.

Garion, C. and Skoczen, B. 2002. Modeling of Plastic Strain-Induced Martensitic Transformation for Cryogenic Applications. Journal of Applied Mechanics, 69 (6), pp. 755-762.

Garion, C., Skoczen, M. and Sgobba, S. 2006. Constitutive Modelling and Identification of Parameters of the Plastic Strain-Induced Martensitic Transformation in 316L Stainless Steel at Cryogenic Temperatures. International Journal of Plasticity, 22 (7), pp. 1234-1264.

Gavriljuk, V.G., Sozinov, A.L., Foct, J., Petrov, J.N., Polushkin, J.A. 1998. Effect of Nitrogen on the Temperature Dependence of the Yield Strength of Austenitic Steels. Acta Materialia, 46 (4), pp. 1157-1163.

Gavriljuk, V.G. and Berns, H. 1999. High Nitrogen Steels: Structure, Properties, Manufacture, Applications. Springer Verlag, Berlin, Germany, 378 p.

Gay, P., Hirsch, P.B. and Kelly, A. 1953. The Estimation of Dislocation Densities in Metals from X-Ray Data. Acta Metallurgica, 1 (1), pp. 315-319.

Gey, N., Petit, B. and Humbert, M. 2005. Electron Backscatter Diffraction Study of ε/α' Martensitic Variants Induced by Plastic Deformation in 304 Stainless Steel. Metallurgical and Materials Transactions A, 36 (12), pp. 3291-3299.

Goodchild, D., Roberts, W.T. and Wilson, D.V. 1970. Plastic Deformation and Phase Transformation in Textured Austenitic Stainless Steel. Acta Metallurgica, 18 (11), pp. 1137-1145.

Gonzáles, J.L., Aranda, R and Jonapá, M. 1992. The Influence of Grain Size on the Kinetics of Strain Induced Martensite in Type 304 Stainless Steel. In: Nordberg, H. and Björklund, J. (Eds.). Applications of Stainless Steel '92, Stockholm, Sweden, 9-11 June 1992, pp. 1009-1016.

Guimarães, J.R.C. and De Angelis, R.J. 1974. Hardening by a Deformation Induced Phase Transformation. Materials Science and Engineering, 15 (2-3), pp. 291-294.

Guntner, C.J. and Reed, R.P. 1962. The Effect of Experimental Variables Including the Martensitic Transformation on the Low-Temperature Mechanical Properties of Austenitic Stainless Steels. Transactions of the ASM, 55 (3), pp. 399-419.

Halder, N.C and Wagner, C.N.J. 1966. Separation of Particle Size and Lattice Strain in Integral Breadth Measurements, Acta Crystallographica, 20 (2), pp. 312-313.

Han, H.N., Lee, C.G., Oh, C.-S., Lee, T.-H. and Kim, S.-J. 2004. A Model for Deformation Behavior and Mechanically Induced Martensitic Transformation of Metastable Austenitic Steel. Acta Materialia, 52 (17), pp. 5203-5214.

Hecker, S.S., Stout, M.G., Staudhammer, K.P. and Smith, J.L. 1982. Effects of Strain State and Strain Rate on Deformation-Induced Transformation in 304 Stainless Steel: Part I. Magnetic Measurements and Mechanical Behavior. Metallurgical Transactions A, 13 (4), pp. 619-626.

Hoffmann, B., Vöhringer, O. and Macherauch, E. 1997. Effect of Tempering on the Microstructure and Strength of Martensitically Hardened Plain Carbon Steels. Materials Science and Engineering A, 234-236, pp. 707-710.

Hoffmann, B., Vöhringer, O. and Macherauch, E. 2001. Effect of Compressive Plastic Deformation on Mean Lattice Strains, Dislocation Densities and Flow Stresses of Martensitically Hardened Steels. Materials Science and Engineering A, 319-321, pp. 299-303.

Hoshen, J. and Kopelman, R. 1976. Percolation and Cluster Distribution. I. Cluster Multiple Labeling Technique and Critical Concentration Algorithm. Physical Review B, 14 (8), pp. 3438-3445.

Hoshino, K. 1983. The Flow Stress of Unstable Austenitic Stainless Steel Accompanied by Deformation-Induced Martensite. Tetsu-to-Hagane, 69 (8), pp. 998-1005.

Hu, X., Wagoner, R.H., Daehn, G.S. and Ghosh S. 1994. The Effect of Inertia on Tensile Ductility. Metallurgical and Materials Transactions A, 25 (12), pp. 2723-2735.

Huang, G.D., Matlock, D.K. and Krauss, G. 1989. Martensite Formation, Strain Rate Sensitivity, and Deformation Behavior of Type 304 Stainless Steel Sheet. Metallurgical Transactions A, 20 (7), pp. 1239-1246.

Hänsel, A.H.C, Hora, P. and Reissner, J. 1998. Model for the Kinetics of Strain-Induced Martensitic Phase Transformation at Non Isothermal Conditions for the Simulation of Sheet Metal Forming Processes with Metastable Austenitic Stainless Steels. In: Huetink, J. and Baaijens, F.P. (Eds.). Simulation of Materials Processing - Theory, Methods & Applications: Proceedings of the 6th International Conference, Enschede, The Netherlands, 22-25 June 1998, pp. 373-378.

Ilola, R. 1999. Effects of Temperature on Mechanical Properties of Austenitic High Nitrogen Steels. Doctoral Thesis. Helsinki University of Technology, Laboratory of Engineering Materials, Espoo, Finland, 100 p.

Iwamoto, T., Tsuta, T. and Tomita, Y. 1998. Investigation on Deformation Mode Dependence of Strain-Induced Martensitic Transformation in TRIP Steels and Modelling of Transformation Kinetics. International Journal of Mechanical Sciences, 40 (2-3), pp. 173-182.

Iwamoto, T. and Tsuta, T. 2000. Computational Simulation of the Dependence of the Austenitic Grain Size on the Deformation Behavior of TRIP Steels. International Journal of Plasticity, 16 (7-8), pp. 791-804.

Joy, D.C., Newbury, D.E. and Davidson, D.L. 1982. Electron Channeling Patterns in the Scanning Electron Microscope. Journal of Applied Physics, 53 (8), pp. 81-121.

Kaufman, L. 1966. The Lattice Stability of the Transition Metals. In: Rudman, P.S., Stringer, J. and Jaffee, R.I. (Eds.). Phase Stability in Metals and Alloys, New York, USA, pp. 125-148.

de Keijser, H., Langford, J.I., Mittemeijer, E.J. and Vogels, A.B.P. 1982. Use of the Voigt Function in a Single-Line Method for the Analysis of X-Ray Diffraction Line Broadening. Journal of Applied Crystallography, 15 (3), pp. 308-314.

Kelly, P.M. 1965. The Martensite Transformation in Steels with Low Stacking Fault Energy. Acta Metallurgica, 13 (6), pp. 635-646.

Kelly, A., Groves, G.W. and Kidd, P. 2000. Crystallography and Crystal Defects. 2nd edition. John Wiley & Sons Ltd, Chichter, UK, 470 p.

Kestenbach, H.-J. 1977. The Effect of Applied Stress on Partial Dislocation Separation and Dislocation Substructure in Austenitic Stainless Steel. Philosophical Magazine, 36 (6), pp. 1509-1515.

Kim, Y.H., Kim, K.Y. and Lee, Y.D. 2003. Nitrogen-Alloyed Metastable Austenitic Stainless Steel for Automotive Structural Applications. In: Speidel, M.O., Kowanda, C. and Diener, M. (Eds.). HNS 2003 High Nitrogen Steels, Schaffhausen, Switzerland, 26-28 March 2003, pp. 149-158.

Klug, H.P. and Alexander, L.E. 1974. X-Ray Diffraction Procedures for Polycrystalline and Amorphous Materials. 2nd edition. John Wiley & Sons Inc., New York, USA, 966 p.

Kubler, R., Berveiller, M., Cherkaoui, M. and Inal, K. 2003. Transformation Textures in Unstable Austenitic Steel. Transactions of the ASME, 125 (1), pp. 12-17.

Lagneborg, R. 1964. The Martensite Transformation in 18% Cr-8% Ni Steels. Acta Metallurgica, 12 (7), pp. 823-843.

Langford, J.I. 1978. A Rapid Method for Analysing the Breadths of Diffraction and Spectral Lines using the Voigt Function. Journal of Applied Crystallography, 11 (1), pp. 10-14.

Langford, J.I. 1980. Accuracy of Crystallite Size and Strain Determined from the Integral Breadth of Powder Diffraction Lines. National Bureau of Standards Special Publication, 567, pp. 255-268.

Latanision, R.M. and Ruff, J.R., A.W. 1971. The Temperature Dependence of Stacking Fault Energy in Fe-Cr-Ni Alloy. Metallurgical Transactions, 2 (2), pp. 505-509.

Lecroisey, F. and Pineau, A. 1972. Martensitic Transformations Induced by Plastic Deformation in the Fe-Ni-Cr-C System. Metallurgical Transactions, 3 (2), pp. 387-396.

Ledbetter, H.M. 1984. Monocrystal-Polycrystal Elastic Constants of a Stainless Steel. Physica Status Solidi, 85 (1), pp. 89-96.

Lee, E.H., Yoo, M.H., Byun, T.S., Hunn, J.D., Farrell K. and Mansur L.K. 2001. On the Origin of Deformation Microstructures in Austenitic Stainless Steel: Part II-Mechanisms. Acta Materialia, 49 (16), pp. 3277-3287.

Lee, W.-S. and Lin, C.-F. 2000. The Morphologies and Characteristics of Impact-Induced Martensite in 304L Stainless Steel. Scripta Materialia, 43 (8), pp. 777-782.

Lee, W.-S. and Lin, C.-F. 2001. Impact Properties and Microstructure Evolution of 304L Stainless Steel. Materials Science and Engineering A, 308 (1-2), pp. 124-135.

Lee, W.-S. and Lin, C.-F. 2002. Comparative Study of the Impact Response and Microstructure of 304L Stainless Steel with and without Prestrain. Metallurgical and Materials Transactions A, 33 (9), pp. 2801-2810.

Levitas, V. 1998. Thermomechanical Theory of Martensitic Phase Transformations in Inelastic Materials. International Journal of Solids and Structures, 35 (9-10), pp. 889-940.

Levitas, V., Idesman, A.V. and Olson, G.B. 1999. Continuum Modeling of Strain-Induced Martensitic Transformations at Shear-Band Intersections. Acta Materialia, 47 (1), pp. 219-233.

Lichtenfeld, J.A., Mataya, M.C. and van Tyne, C.J. 2006. Effect of Strain Rate on Stress-Strain Behavior of Alloy 309 and 304L Austenitic Stainless Steel. Metallurgical and Materials Transactions A, 37 (1), pp. 147-161.

Livitsanos, C.P. and Thomson, P.F. 1977. The Effect of Temperature and Deformation Rate on Transformation-Dependent Ductility of a Metastable Austenitic Stainless Steel. Materials Science and Engineering, 30 (2), pp. 93-98.

Ludwigson, D.C. and Berger, J.A. 1969. Plastic Behaviour of Metastable Austenitic Stainless Steels. Journal of the Iron and Steel Institute, 207 (1), pp. 63-69.

Mangonon, P.L. and Thomas, G. 1970a. The Martensite Phases in 304 Stainless Steel. Metallurgical Transactions, 1 (6), pp. 1577-1586.

Mangonon, P.L. and Thomas, G. 1970b. Structure and Properties of Thermal-Mechanically Treated 304 Stainless Steel. Metallurgical Transactions, 1 (6), pp. 1587-1594.

Mikkola, D.E. and Cohen, J.B. 1965. Examples of Applications of Line Broadening. In: Cohen, J.B. and Hilliard, J.E. (Eds.). Local Atomic Arrangements Studied by X-Ray Diffraction. Proceedings of a Symposium Held in Chicago, USA, 15th February 1965, pp. 289-333.

Miodownik, A.P. 1978. The Calculation of Stacking Fault Energies in Fe-Ni-Cr Alloys. CALPHAD, 2 (3), pp. 207-226.

Murr, L.E., Wong, G.I. and Horylev, R.J. 1973. Measurement of Interfacial Free Energies and Associated Temperature Coefficients in 304 Stainless Steel. Acta Metallurgica, 21 (5), pp. 595-604.

Murr, L.E., Staudhammer, K.P. and Hecker, S.S. 1982. Effects of Strain State and Strain Rate on Deformation-Induced Transformation in 304 Stainless Steel: Part II. Microstructural Study. Metallurgical Transactions A, 13 (4), pp. 627-635.

Müllner, P., Solenthaler, C., Uggowitzer, P. and Speidel, M.O. 1993. On the Effect of Nitrogen on the Dislocation Structure of Austenitic Stainless Steel. Materials Science and Engineering A, 164 (1-2), pp. 164-169.

Müllner, P., Solenthaler, C. and Speidel, M.O. 1994. Second Order Twinning in Austentic Steel. Acta Metallurgica et Materialia, 42 (5), pp. 1727-1732.

Narutani, T., Olson, G.B. and Cohen, M. 1982. Constitutive Flow Relations for Austenitic Steels during Strain-Induced Martensitic Transformation. Journal de Physique, 43 (C4), pp. 429-434.

Narutani, T. 1989. Effect of Deformation-Induced Martensitic Transformation on the Plastic Behavior of Metastable Austenitic Stainless Steel. Materials Transactions, JIM, 30 (1), pp. 33-45.

Neff, D.V., Mitchell, T.E. and Troiano, A.R. 1969. The Influence of Temperature, Transformation, and Strain Rate on the Ductility Properties of Austenitic Stainless Steels. Transactions of the ASM, 62 (4), pp. 858-868.

Nohara, K., Ono, Y. and Ohashi, N. 1977. Composition and Grain-Size Dependencies of Strain-Induced Martensitic Transformation in Metastable Austenitic Stainless Steels. Journal of Iron and Steel Institute of Japan, 63 (5), pp. 212-222.

Noyan, I.C. and Cohen, J.B. 1987. Residual Stress, Measurement by Diffraction and Interpretation. Springer-Verlag, New York, USA, 276 p.

Olson, G.B. and Cohen, M. 1972. A Mechanism for the Strain-Induced Nucleation of Martensitic Transformations. Journal of Less-Common Metals, 28 (1), pp. 107-118.

Olson, G.B. and Cohen, M. 1975. Kinetics of Strain-Induced Martensitic Nucleation. Metallurgical Transactions A, 6 (4), pp. 791-795.

Olson, G.B. and Cohen, M. 1976a. A General Mechanism of Martensitic Nucleation: Part I. General Concepts and the FCC $\rightarrow$ HCP Transformation. Metallurgical Transactions A, 7 (12), pp. 1897-1904.

Olson, G.B. and Cohen, M. 1976b. A General Mechanism of Martensitic Nucleation: Part II. FCC $\rightarrow$ BCC and Other Martensitic Transformations. Metallurgical Transactions A, 7 (12), pp. 1905-1914.

Olson, G.B. and Cohen, M. 1986. Martensitic Transformation as a Deformation Process. In: Antalovich, S.D., Gerberich, W.W. and Ritchie, R.O. (Eds.). Proceedings of Earl R. Parker Symposium on Structure/Property Relationships, TMS-AIME, Warrendale, USA, pp. 367-390.

Patel, J.R. and Cohen, M. 1953. Criterion for the Action of Applied Stress in the Martensitic Transformation. Acta Metallurgica, 1 (5), pp. 531-538.

Paterson, M.S. 1952. X-Ray Diffraction by Face-Centered Cubic Crystals with Deformation Faults. Journal of Applied Physics, 23 (8), pp. 805-811.

Pešička, J., Kužel, R., Dronhofer, A. and Eggeler, G. 2003. The Evolution of Dislocation Density During Heat Treatment and Creep of Tempered Martensite Ferritic Steels. Acta Materialia, 51 (16), pp. 4847-4862.

Petit, B., Gey, N., Humbert, M., Bolle, B. and Cherkaoui, M. 2005. Microstructure and Texture Evolution of Cold Worked 304 Stainless Steel, Experimental and Modelling. In: v. Haute, P. and Kestens, L. (Eds.). Textures of Material, ICOTOM 14, Proceedings of the 14th International Conference on Textures of Materials, Leuven, Belgium, 11-15 July 2005, pp. 405-410.

Powell, G.W., Marshall, E.R. and Backofen, W.A. 1958. Strain Hardening of Austenitic Stainless Steel. Transactions of the ASM, 50 (1), pp. 478-497.

Reed, R.P. and Guntner, C.J. 1964. Stress-Induced Martensitic Transformations in 18Cr-8Ni Steel. Transactions of the Metallurgical Society of AIME, 230 (7), pp. 1713-1720.

Reed, R.P. and Schramm, R.E. 1974. Relationship between Stacking-Fault Energy and X-Ray Measurements of Stacking-Fault Probability and Microstrain. Journal of Applied Physics, 45 (11), pp. 4705-4711.

Reed-Hill, R.E and Abbaschian, R. 1992. Physical Metallurgy Principles. 3rd edition. PWS-Kent Publishing Company, Boston, USA, 926 p.

Rémy, L. and Pineau, A. 1976. Twinning and Strain-Induced F.C.C.→H.C.P. Transformation on the Mechanical Properties of Co-Ni-Cr-Mo Alloys. Materials Science and Engineering, 26 (1), pp. 123-132.

Rémy, L. and Pineau, A. 1977. Twinning and Strain-Induced F.C.C.→H.C.P. Transformation in the Fe-Mn-Cr-C System. Materials Science and Engineering, 28 (1), pp. 99-107.

Rémy, L. and Pineau, A. 1978. Temperature Dependence of Stacking Fault Energy in Close-Packed Metals and Alloys. Materials Science and Engineering, 36 (1), pp. 47-63.

Rhodes, C.G. and Thompson, A.W. 1977. The Composition Dependence of Stacking Fault Energy in Austenitic Stainless Steels. Metallurgical Transactions A, 8 (12), pp. 1901-1906.

Rosen, A., Jago, R. and Kjer, T. 1972. Tensile Properties of Metastable Stainless Steels. Journal of Materials Science, 7 (8), pp. 870-876.

Ruland, W. 1965. The Integral Width of the Convolution of a Gaussian and a Cauchy Distribution, Acta Crystallographica, 18 (3), p. 581.

Sanderson, G.P. and Llewellyn, D.T. 1969. Mechanical Properties of Standard Austenitic Stainless Steels in the Temperature Range -196 to +800°C. Journal of the Iron and Steel Institute, 207 (8), pp. 1129-1140.

Schedin, E., Prentzas, L. and Hilding, D. 2004. Finite Element Simulation of the TRIP-effect in Austenitic Stainless Steel. SAE Transactions: Journal of Materials & Manufacturing, 113 (5), pp. 438-445.

Schoening, F.R.L. 1965. Strain and Particle Size Values from X-Ray Line Breadths. Acta Crystallographica, 18 (5), pp. 975-976.

Schramm, R.E. and Reed R.P. 1975. Stacking Fault Energies of Seven Commercial Austenitic Stainless Steels. Metallurgical Transactions A, 6 (7), pp. 1345-1351.

Serri, J., Martiny, M. and Ferron, G. 2005a. Finite Element Analysis of the Effects of Martensitic Phase Transformation in TRIP Steel Sheet Forming. International Journal of Mechanical Sciences, 47 (6), pp. 884-901.

Serri, J., Martiny, M. and Ferron, G. 2005b. A Numerical Analysis of the Formability of Unstable Austenitic Steels. Journal of Materials Processing Technology, 164-165, pp. 1241-1247.

SFS-EN 10088-2. 1995. Stainless Steels. Part 2. Technical Delivery Conditions for Sheet/Plate and Strip for General Purposes. Suomen Standardisoimisliitto SFS, Helsinki, Finland, 85 p.

Shin, H.C., Ha, T.K. and Chang, Y.W. 2001. Kinetics of Deformation Induced Martensitic Transformation in a 304 Stainless Steel. Scripta Materialia, 45 (7), pp. 823-829.

Shrinivas, V., Varma, S.K. and Murr, L. 1995. Deformation-Induced Martensitic Characteristics in 304 and 316 Stainless Steels during Room-Temperature Rolling. Metallurgical and Materials Transactions A, 26 (3), pp. 661-671.

Simkin, B.A. and Crimp, M.A. 1999. An Experimentally Convenient Configuration for Electron Channeling Contrast Imaging. Ultramicroscopy, 77 (1-2), pp. 65-75.

Smallman, R.E. and Westmacott, K.H. 1957. Stacking Faults in Face-Centered Cubic Metals and Alloys. Philosophical Magazine, 2 (17), pp. 669-683.

Spencer, K., Embury, J.D., Conlon, K.T., Véron, M. and Bréchet, Y. 2004. Strengthening via the Formation of Strain-Induced Martensite in Stainless Steels. Materials Science and Engineering A, 387-389, pp. 873-881.

Stauffer, D. and Aharony, A. 1994. Introduction to Percolation Theory. 2nd edition. Taylor & Francis Ltd, London, UK, 181 p.

Staudhammer, K.P. and Murr, L.E. 1980. The Effect of Prior Deformation on the Residual Microstructure of Explosively Deformed Stainless Steels. Materials Science and Engineering, 44 (1), pp. 97-113.

Staudhammer, K.P., Frantz, C.E., Hecker S.S. and Murr, L.E. 1980. Effects of Strain Rate on Deformation-Induced Martensite in 304 Stainless Steel. In: Meyers, M.A. and Murr, L.E. (Eds.). Proceedings of an International Conference on Metallurgical Effects of High-Strain-Rate Deformation and Fabrication, Albuquerque, USA, 22-26 June 1980, pp. 91-112.

Staudhammer, K.P., Murr, L.E. and Hecker, S.S. 1983. Nucleation and Evolution of Strain-Induced Martensitic (B.C.C.) Embryos and Substructure in Stainless Steel: A Transmission Electron Microscopy Study. Acta Metallurgica, 31 (2), pp. 267-274.

Stokes, A.R. 1948. A Numerical Fourier-Analysis Method for the Correction of Widths and Shapes of Lines on X-Ray Powder Photographs. Proceedings of the Physical Society of London, 61, pp. 382-391.

Stringfellow, R.G., Parks, D.M. and Olson, G.B. 1992. A Constitutive Model for Transformation Plasticity Accompanying Strain-Induced Martensitic Transformations in Metastable Austenitic Stainless Steels. Acta Metallurgica et Materialia, 40 (7), pp. 1703-1716.

Suzuki, T., Kojima, H., Suzuki, K., Hashimoto, T., Koike, S. and Ichihara, M. 1976. Plastic Deformation and Martensitic Transformation in an Iron-Base Alloy. Scripta Metallurgica, 10 (4), pp. 353-358.

Suzuki, T., Kojima, H., Suzuki, K., Hashimoto, T. and Ichihara, M. 1977. An Experimental Study of the Martensite Nucleation and Growth in 18/8 Stainless Steel. Acta Metallurgica, 25 (10), pp. 1151-1162.

Säynevirta, J. 2005. Life Cycle Environmental Evaluation and Cost Analysis of Structural Automotive Materials. Master's Thesis. Helsinki University of Technology, Laboratory of Engineering Materials, Espoo, Finland, 156 p.

Talonen, J., Aspegren, P. and Hänninen, H. 2004. Comparison of Different Methods for Measuring Strain Induced α'-martensite Content in Austenitic Steels. Materials Science and Technology, 20 (12), pp. 1506-1512.

Talonen, J., Nenonen, P., Pape, G. and Hänninen, H. 2005. Effect of Strain Rate on the Strain-Induced γ→α'-Martensite Transformation and Mechanical Properties of Austenitic Stainless Steels. Metallurgical and Materials Transactions A, 36 (2), pp. 421-431.

Talonen J. and Hänninen, H. 2006. Effect of Tensile Properties on the Energy-Absorbing Capacity of Weld-Bonded Austenitic Stainless Steel Profiles. International Journal of Crashworthiness, 11 (4), pp. 371-378.

Talonen, J., Taulavuori, T. and Hänninen, H. 2006. Effect of Temperature on Tensile Behaviour and Microstructural Evolution of Nitrogen Alloyed Austenitic Stainless Steel. In: Dong, H., Su, J. and Speidel, M. (Eds.). Proceedings of International Conference on High Nitrogen Steels HNS2006, Jiuzhaigou, China, 29-31 August 2006, pp. 52-58.

Tamura, I. 1982. Deformation-Induced Martensitic Transformation and Transformation-Induced Plasticity in Steels. Metal Science, 16 (5), pp. 245-253.

Teng, F.-E., Yang, B. and Wang, Y. 1992. A Study of Stacking Faults in Deformed Austenitic Stainless Steel by X-Ray Diffraction. Metallurgical Transactions A, 23 (10), pp. 2859-2861.

Tomita, Y. and Iwamoto, T. 1995. Constitutive Modeling of TRIP Steel and Its Application to the Improvement of Mechanical Properties. International Journal of Mechanical Sciences, 37 (12), pp. 1295-1305.

Tomota, Y., Tokuda, H., Adachi, Y., Wakita, M., Minakawa, N., Moriai, A. and Morii, Y. 2004. Tensile Behavior of TRIP-Aided Multi-Phase Steels Studied by *In Situ* Neutron Diffraction. Acta Materialia, 52 (20), pp. 5737-5745.

Tsuchida, N. and Tomota, Y. 2000. A Micromechanic Modeling for Transformation Induced Plasticity in Steels. Materials Science and Engineering A, 285 (1-2), pp. 345-352.

Tsuta, T. and Cortés, J.A. 1993. Flow Stress and Phase Transformation Analyses in Austenitic Stainless Steel under Cold Working (Part 2, Incremental Theory under Multiaxial Stress State by the Finite-Element Method). JSME International Journal, 36 (1), pp. 63-72.

Underwood, E.E. 1985. Quantitative Metallography. In: Metals Handbook. Ninth edition. American Society for Metals, Metals Park, USA, pp. 123-134.

Ungár, T., Gubicza, J., Ribárik, G., and Borbély, A. 2001. Crystallite Size Distribution and Dislocation Structure Determined by Diffraction Profile Analysis: Principles and Practical Application to Cubic and Hexagonal Crystals. Journal of Applied Crystallography, 34 (3), pp. 298-310.

Vander Voort, G.F. 1999. Metallography, Principles and Practice. ASM International, Materials Park, USA, 752 p.

Varma, S.K., Kalyanam, J., Murr, L. and Srinivas, V. 1994. Effect of Grain Size on Deformation-Induced Martensite Formation in 304 and 316 Stainless Steels during Room Temperature Tensile Testing. Journal of Materials Science Letters, 13 (2), pp. 107-111.

Velterop, L., Delhez, R., de Keijser, Th.H., Mittemeijer, E.J. and Reefman, D. 2000. X-Ray Diffraction Analysis of Stacking and Twin Faults in F.C.C. Metals: a Revision and Allowance for Texture and Non-Uniform Fault Probabilities. Journal of Applied Crystallography 33 (2), pp. 296-306.

Venables, J.A. 1962. The Martensite Transformation in Stainless Steel. Philosophical Magazine, 7 (73), pp. 35-44.

Wang, Y., Lee, S. and Lee, Y. 1982. X-ray Line Profile Analysis of Deformed Al. Journal of Applied Crystallography, 15 (1), pp. 35-38.

Warren, B.E. and Averbach, B.L. 1950. The Effect of Cold-Work Distortion on X-Ray Patterns. Journal of Applied Physics, 21 (6), pp. 595-599.

Warren, B.E. and Averbach, B.L. 1952. The Separation of Cold-Work Distortion and Particle Size Broadening in X-Ray Patterns. Journal of Applied Physics, 23 (4), p. 497.

Warren, B.E. 1990. X-Ray Diffraction. Dover Publications Inc., New York, USA, 381 p.

Wayman, C.M. and Bhadeshia, H.K.D.H. 1996. Phase Transformations, Nondiffusive. In: Cahn, R.W. and Haasen, P. (Eds.). Physical Metallurgy. Fourth edition. Elsevier Science Publishers, Amsterdam, The Netherlands, pp. 1507-1554.

Wilkens, M. 1970. The Determination of Density and Distribution of Dislocations in Deformed Single Crystals from Broadened X-Ray Diffraction Profiles. Physica Status Solidi A, 2 (2), pp. 359-370.

Wilkens, M. 1979. X-ray Diffraction Line Broadening of Crystals Containing Small-Angle Boundaries. Journal of Applied Crystallography, 12 (1), pp. 119-125.

Wilkinson, A.J. and Hirsch, P.B. 1997. Electron Diffraction Based Techniques in Scanning Electron Microscopy of Bulk Materials. Micron, 28 (4), pp. 279-308.

Williamson G.K. and Smallman, R.E. 1956. Dislocation Densities in Some Annealed and Cold-Worked Metals from Measurements on the X-Ray Debye-Scherrer Spectrum. Philosophical Magazine, 1 (1), pp. 34-46.

Zackay, V.F., Parker, E.R., Fahr, D. and Busch, R. 1967. The Enhancement of Ductility in High-Strength Steels. Transactions of the ASM, 60 (2), pp. 252-259.

ISBN 978-951-22-8779-6
ISBN 978-951-22-8780-2 (PDF)
ISSN 1795-2239
ISSN 1795-4584 (PDF)